THÈSE DE DOCTORAT
DE L'UNIVERSITÉ DE LILLE

LABORATOIRE DE GÉNIE CIVIL ET GÉO-ENVIRONNEMEN

Présentée par

Shanshan HE

pour obtenir le grade de

DOCTEUR DE L'UNIVERSITÉ DE LILLE

Domaine

GÉNIE CIVIL

Sujet de la thèse

Étude numérique de la migration des fines particules dans les sols granulaires sous des processus de couplage hydromécanique

Soutenue le 3 Octobre 2025 devant le jury composé de:

Ali ZAOUI, Professeur	Université de Lille	*Président du jury*
Richard GIOT, Professeur	Université Poitiers	*Rapporteur*
Ali DAOUADJI, Professeur	INSA de Lyon	*Rapporteur*
Hui DONG, Professeur	Université de Xiangtan	*Examinateur*
Yun JIA, MCF-HDR	Université de Lille	*Examinatrice*
Hanbing BIAN, MCF-HDR	Université de Lille	*Directeur de thèse*

LGCgE - UNIVERSITÉ DE LILLE

DOCTORAL THESIS
OF THE UNIVERSITY OF LILLE

CIVIL AND GEO-ENVIRONMENTAL ENGINEERING LABORATORY

Presented by

Shanshan HE

to obtain the degree of

DOCTOR OF THE UNIVERSITY OF LILLE

Field

CIVIL ENGINEERING

Provisional version for the jury

Numerical investigation of fine particle migration in granular soils under hydro-mechanical coupling processes

Defended on 3 October 2025 before the jury composed of:

Ali ZAOUI, Professeur	University of Lille	*President of the jury*
Richard GIOT, Professor	Poitiers University	*Reviewer*
Ali DAOUADJI, Professeur	INSA of Lyon	*Reviewer*
Hui DONG, Professeur	University of Xiangtan	*Member*
Yun JIA, MCF-HDR	University of Lille	*Member*
Hanbin BIAN, MCF-HDR	University of Lille	*Thesis Supervisor*

LGCgE - UNIVERSITY OF LILLE

Résumé

L'érosion interne constitue l'une des principales causes de défaillance des digues et des barrages en terre, compromettant la sécurité des infrastructures et représentant un risque pour les vies humaines et les biens. Cette thèse analyse les mécanismes micromécaniques de l'érosion interne dans les sols granulaires en combinant des expérimentations en laboratoire et des modélisations numériques. L'accent est mis sur l'influence des conditions de charge hydraulique, de la teneur de particules fines, de la porosité, de la pression de confinement et de la texture du sol sur la migration des particules fines et l'évolution de la structure granulaire.

Une série d'essais ont été menés afin d'étudier les effets du gradient hydraulique et de la distribution granulométrique sur la migration des particules fines dans les sols granulaires. Des techniques d'imagerie à haute résolution ont permis de caractériser les motifs d'érosion à l'échelle des pores. Un critère de stabilité interne modifié, intégrant la porosité et la gradation, est proposé pour mieux décrire les conditions de déclenchement de la migration.

Afin d'approfondir la compréhension des mécanismes d'érosion interne, et plus particulièrement des migrations des particules fines dans les sols granulaires, un modèle couplé Méthode des Éléments Discrets et Maillage Fluide Dynamique (DEM & DFM) a été développé et calibré sur la base des observations expérimentales. Ce modèle reproduit les interactions dynamiques entre les particules fines, les particules granulaires et le fluide au cours du processus d'érosion interne, et permet d'analyser l'influence de paramètres hydrauliques et de microstructuraux tels que la porosité, le gradient hydraulique et le mouvement des particules sur la teneur en fines et la réorganisation de la structure granulaire. Le modèle est ensuite étendu pour considérer l'influence de la pression de confinement et les différentes textures de sol.

Les résultats de cette recherche apportent une meilleure compréhension du mouvement des particules fines dans les sols granulaires, et soutiennent le développement d'outils numériques sous divers scénarios hydro-mécaniques pour l'évaluation et la prévision de la stabilité interne des structures géotechniques.

Mots-clés : Érosion interne, Remblais, Couplage DEM-DFM, Migration des particules fines, Gradient hydraulique, Pression de confinement

Abstract

Internal erosion is one of the main causes of failure in earth dikes and embankment dams, threatening the safety of infrastructures and posing risks to human lives and property. This thesis investigates the micromechanical mechanisms of internal erosion in granular soils through a combined approach of laboratory experiments and numerical modeling. The focus is placed on the influence of hydraulic loading conditions, fine particle content, porosity, confining pressure, and soil texture on the migration of fine particles and the evolution of the granular structure.

A series of laboratory tests were conducted to examine the effects of hydraulic gradient and particle size distribution on the migration of fine particles within granular soils. High-resolution imaging techniques were employed to characterize erosion patterns at the pore scale. A modified internal stability criterion, incorporating porosity and gradation, is proposed to better describe the onset conditions of particle migration.

To deepen the understanding of internal erosion mechanisms, particularly the migration of fine particles in granular soils, a coupled Discrete Element Method and Dynamic Fluid Mesh (DEM & DFM) model was developed and calibrated based on experimental observations. This model reproduces the dynamic interactions between fine particles, granular particles, and the fluid during internal erosion, allowing the analysis of the influence of hydraulic and microstructural parameters such as porosity, hydraulic gradient, and particle motion on the fine content and the reorganization of the granular structure. The model is further extended to consider the influence of confining pressure and various soil textures.

The results of this research provide an improved understanding of fine particle migration in granular soils, and support the development of numerical tools under various hydro-mechanical scenarios for assessing and predicting the internal stability of geotechnical structures.

Keywords: Internal erosion, Embankments, DEM-DFM coupling, Fine particle migration, Hydraulic gradient, Confining pressure

Acknowledgement

As I come to the end of this journey, I am filled with deep gratitude and reflection.

First and foremost, I would like to express my heartfelt thanks to my parents. It is my family who has shaped my resilience and confidence, enabling me to one day travel from a small village in Zhejiang, China, to Europe, creating countless precious memories along the way.

I am deeply indebted to my supervisor, Professor Hanbing Bian, for his rigorous academic guidance, patience, and unwavering support throughout my doctoral studies. His dedication to research and his exemplary character have profoundly influenced my academic growth and personal development. I am also sincerely grateful to Professor Jia Yun, whose kindness and care made me feel at home even when I was far away. Their encouragement and help sustained me through moments of difficulty and doubt.

I would like to express my deepest gratitude to the members of my defense committee. I am sincerely thankful to Professor Ali Zaoui from the University of Lille, who served as President of the jury; to Professor Richard Giot from the University of Poitiers and Professor Ali Daouadji from INSA Lyon, who served as rapporteurs; to Professor Hui Dong from Xiangtan University and Professor Jia Yun from the University of Lille, who served as examiners; and to my thesis supervisor, Professor Hanbing Bian from the University of Lille, for his continuous guidance and support. Their insightful comments and valuable feedback greatly improved the quality of this thesis.

My sincere appreciation also goes to my professors at the University of Lille, including Isam Shahrou, Ammar Aljer, and Fahmi Zairi, for their invaluable instruction and guidance.

I am thankful to my fellow lab members, Zhouwantian, Zhang Hualin, Xiao Junyi, Tang Jie, Yan Xianhang, Cheng Zihua, Yu Huicong, and Guo Yang, for their companionship and collaboration. I would also like to thank my dear friends I met in France, including Hou Nan, Cai Runcheng, Liu Shuilian, Hadia Zaiter, M'hammed Taghlaoui, Lionel Ogouari, Jiwei Jia, Ugo Cachot, Majd Al Jurdi, Hanan Jafar, and Mohammed Itair, for bringing joy, warmth, and friendship into my life abroad.

I extend my heartfelt gratitude to Ms. Radia Sedaoui, my mentor at the United Nations Economic and Social Commission for Western Asia (UNESCWA). During my internship

there, I learned a great deal from her professionalism, leadership, and vision, which have deeply inspired me.

Last but not the least, I would like to express my sincere appreciation to the China Scholarship Council (CSC) for financially supporting my doctoral studies in France. My homeland has always been my strongest foundation. Experiencing different cultures and systems in Europe has only deepened my love for my country and strengthened my resolve to contribute to its future.

Shanshan HE

Contents

List of Figures

List of Tables

Chapter I

The migration of fine particles in granular soils: State of the Art

1 Introduction

As extreme climate events become more frequent and intense, the risks of flooding are increasing worldwide. Rising temperatures, changing rainfall patterns, and sea level rise contribute to more severe and unpredictable flood scenarios. In this context, flood protection infrastructures such as embankments face growing challenges, particularly in low-lying and riverine regions. Meanwhile, the global shift toward renewable energy and the expansion of related projects near rivers and coasts further heighten the need for resilient and adaptable flood defenses.

Embankments, often built with natural soils for economic and practical reasons, are vulnerable to gradual degradation over time (Figure I .1). Among the various degradation processes, the migration of fine particles within granular soils plays a critical role in altering the internal structure of these materials, which in turn affects their permeability and mechanical stability. This process is governed by the interaction between hydraulic flow and soil skeleton deformation, involving complex hydro-mechanical coupling mechanisms. Despite extensive research, the fundamental understanding of these coupled processes and their implications for soil behavior remains limited.

This chapter provides an overview of the motivation and context for studying the migration of fine particles in granular soils under hydro-mechanical coupling. It begins by describing the microstructural characteristics of embankment fill materials and their relevance to particle migration. Next, key experimental studies that investigate the initiation and evolution of fine particle movement are reviewed. The chapter then introduces nu-

merical modeling approaches that capture the coupled fluid–solid interactions governing these processes. Finally, the influence of factors such as soil gradation, porosity, and loading conditions is discussed, establishing the foundation for the numerical investigations presented in the following chapters.

Figure I .1: Embankment degradation caused by fine particle migration (Irons et al., 2014)

2 Characteristics of embankment fill materials

2.1 Microstructure of embankment fill materials

The microstructure of embankment fill materials plays a crucial role in determining their macroscopic properties, such as shear strength, permeability, compressibility, and overall service life. In embankment construction, the fill materials are typically composed of natural resources, such as soil, gravel, and crushed stone, though industrial by-products like fly ash and slag may also be used (Figure I .2(a)) (Divya Jyothi and Ramya Krishna, 2021; El Mountassir et al., 2014). Upon scanning, these materials can be categorized as a binary mixture of coarse and fine particles (Figure I .2(b)). Coarse and fine particles possess distinct engineering properties that influence the overall performance of the fill material. Embankments constructed using well-graded soil, for instance, exhibit enhanced seismic resistance (Jiang et al., 2015). By optimizing the proportion and combination of materials, the performance of the embankment, such as its stability and durability, can be significantly improved.

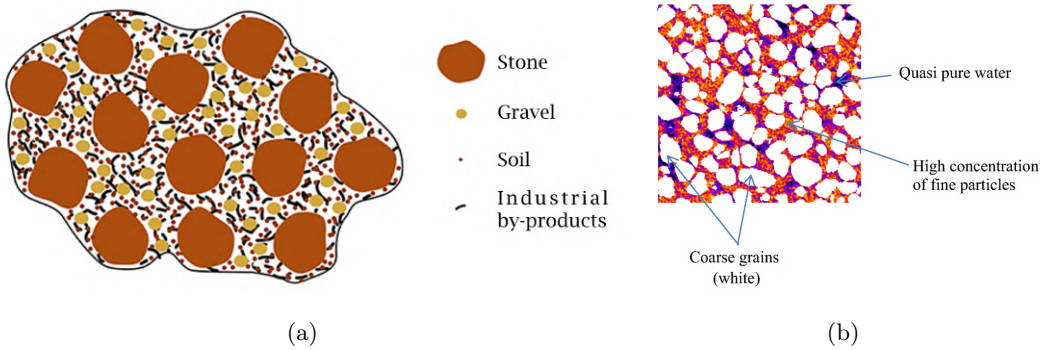

Figure I .2: Composition of embankment fill material: (a) Composition of substances that may be contained in the embankment fill material (Department of Jobs, 2024); (b) Coarse and fine particles in the embankment fill material (Nguyen et al., 2019)

2.1.1 Particle morphology and distribution

The morphology of particles in embankment fill materials is a fundamental aspect of their microstructure. The size, shape, and distribution of these particles directly influence the packing arrangement of the material, which in turn affects its porosity and density (Xing et al., 2021). For example, particles in gravel and crushed stone typically exhibit irregular shapes, leading to fewer contact points between particles and the formation of larger voids (Figure I .3). In contrast, finer particles such as clay and silt possess higher specific surface areas and greater adhesive properties, enabling them to fill the gaps between larger particles, which reduces the overall porosity of the material.

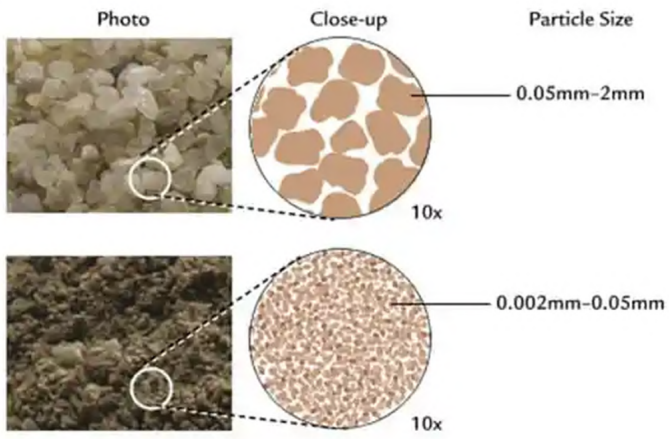

Figure I .3: Comparison of porosity of soils composed of coarser particles and finer particles, respectively (Rahman, 2018)

Moreover, the heterogeneity in particle shapes significantly influences the material's strength (Yang and Luo, 2015; Zou et al., 2023). Angular particles generally exhibit higher frictional resistance, which enables them to better withstand shear failure under applied forces (Gong et al., 2024). In contrast, although rounded particles can pack more densely (Figure I .4), the lower sliding friction between them increases their susceptibility to displacement and failure during shear stress.

(a) (b)

Figure I .4: Angular particles and rounded particles: (a) Angular particles; (b) Rounded particles (Panchuk, 2019)

2.1.2 Interactions between particles

In the microstructure of fill materials, particle interactions are governed by mechanical contact forces, adhesion forces, and electrostatic forces (Figure I .5). The mechanical contact between coarse particles mainly determines the skeleton structure of the material, while fine particles contribute to the material's overall stability through adhesion and filling effects (Taha et al., 2019). These various interactions between particles enable the fill material to effectively disperse external stresses, preventing localized stress concentrations and thereby enhancing the embankment's bearing capacity.

2.1.3 Microstructural changes during the infiltration process

Water infiltration has a profound impact on the microstructure of embankment fill materials. As water permeates the material, fine particles may migrate with the flow, altering the internal distribution of particles (Figure I .6). The loss of these fine particles increases the porosity of the material, which in turn raises its permeability. This increased permeability may lead to local instabilities or even collapse of the embankment.

Moreover, water infiltration can trigger chemical reactions or cause particle surface expansion, further influencing the mechanical properties of the fill material (Chang et al., 2022). For instance, in clay-based fill materials, water infiltration can lead to the formation

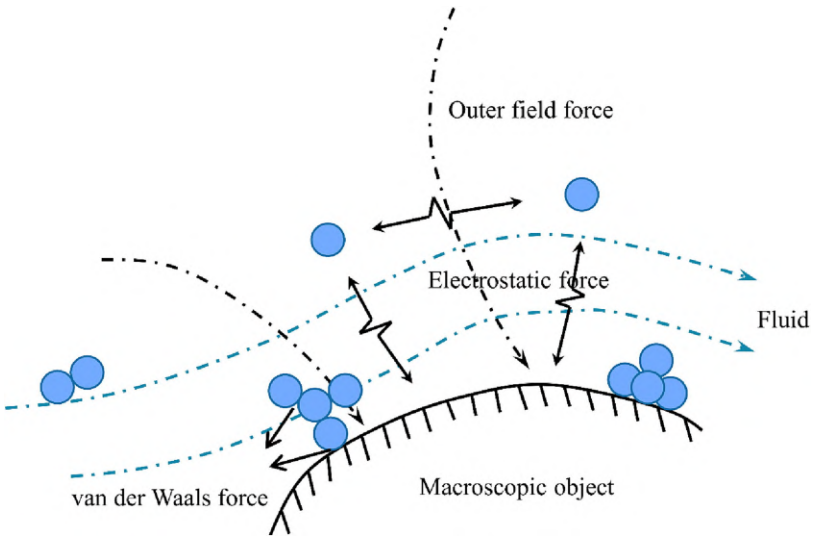

Figure I .5: Schematic of particle interaction mechanisms in granular fill materials (Fang et al., 2024)

of water films on particle surfaces, reducing friction between particles and making the material more susceptible to shear failure under applied stress.

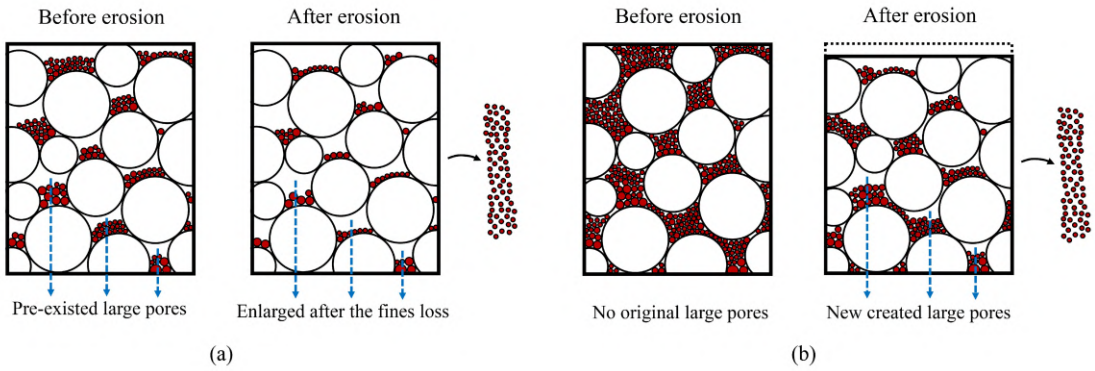

Figure I .6: Mesoscopic fabric illustration to compare the change in pore channels induced by fine particle loss in: (a) Soil in which fine particles under-fill the inter-granular pores; (b) Soil in which fine particles precisely-fill the inter-granular pores (Deng et al., 2023c)

2.2 Overview of fine particle migration mechanisms and development processes

Fine particle migration in granular soils is a key process governing seepage-induced instability. Depending on hydraulic and structural conditions, several migration patterns

can be identified, including backward erosion, concentrated leak erosion, contact erosion, and suffusion (Figure I .7) (Bonelli et al., 2013).

Backward erosion (Zheng et al., 2022) occurs when seepage flow initiates from the downstream side and progresses upstream, removing fine particles and forming retrogressive channels, commonly observed at the base of embankments. Concentrated leak erosion (Chen et al., 2021b) develops in localized weak zones where hydraulic gradients intensify, leading to focused fine particle removal. Contact erosion (Guo et al., 2023) takes place at the interface between materials of contrasting grain sizes, where fine particles are detached and transported through coarser frameworks, causing progressive interface degradation. Suffusion (Nguyen et al., 2019) involves the selective migration of fine particles through the pore network formed by the coarse skeleton, modifying the pore structure and weakening the soil's mechanical integrity. These migration modes may coexist and interact, contributing collectively to the onset and progression of hydro-mechanical instability in granular soils.

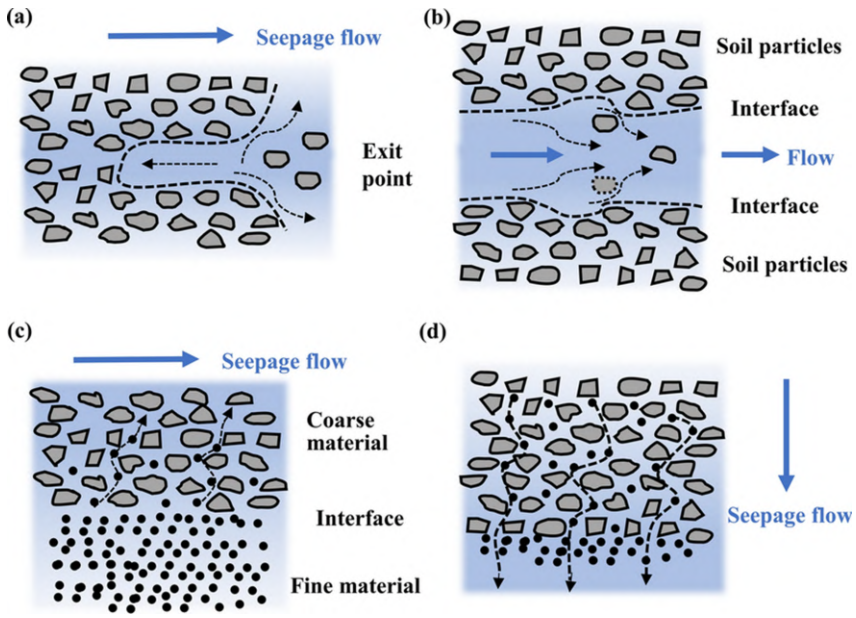

Figure I .7: Micro-view of internal erosion development process: (a) Backward erosion; (b) Concentrated leakage erosion; (c) Contact erosion; (d) Suffusion (Sharp et al., 2013)

The migration of fine particles typically evolves progressively. As seepage intensifies, hydraulic forces mobilize fines within the soil matrix, forming local voids and disrupting the granular skeleton (Figure I .8). With continued particle loss, preferential flow paths develop and expand, enhancing permeability and accelerating local instability. Eventually, these flow channels may connect to form continuous conduits, increasing seepage veloc-

ity and triggering large-scale deformation or failure. This sequence represents a gradual transition from localized particle detachment to macroscopic structural instability under coupled hydro-mechanical effects.

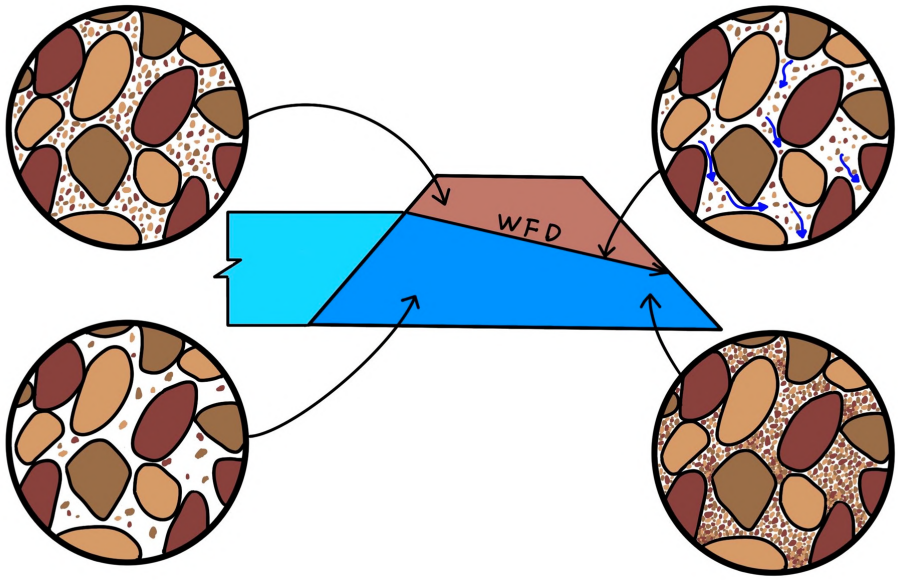

Figure I .8: Particle movement processes where internal erosion occurs

3 Experimental observations of fine particle migration

Experimental studies are fundamental to understanding fine particle migration and its coupling with hydraulic and mechanical responses. Laboratory investigations enable direct observation of particle detachment, transport, and deposition processes, as well as associated changes in porosity, permeability, and strength. These findings provide critical insights into the mechanisms governing soil stability, support the validation of numerical models, and guide the design of erosion-resistant materials and structures. Therefore, experimental research remains indispensable for characterizing fine particle migration and assessing its implications for geotechnical safety and performance.

3.1 Permeability and piping tests

As early as the 19th century, the design and construction of embankments were already well established; however, the underlying causes of many failures remained poorly understood. It was not until the catastrophic failure of the South Fork Dam in Pennsylvania,

USA, in 1889 (Figure I .9) that engineers and researchers began to recognize the significance of seepage-induced fine particle migration and its potential role in the progressive deterioration of earth structures. Early investigations focused mainly on permeability and piping tests (Richards and Reddy, 2007), aiming to explore how water flow through soil could initiate the movement of fines and lead to internal instability.

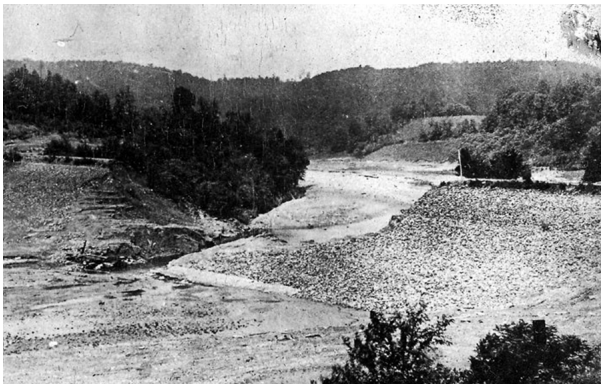

Figure I .9: South Fork Dam Failure in Wisconsin, USA (American Society of Civil Engineers, 1891)

The earliest permeability experiments directed flowing water through soil specimens under controlled hydraulic gradients to examine variations in permeability, deformation, and the soil's capacity to transmit fine particles (Fraser, 1935; Hendrickson, 1934). These studies provided the first insights into how hydraulic flow interacts with the soil's internal structure. Subsequent piping tests were developed to observe how continuous fine particle migration could gradually form preferential flow channels—often referred to as "pipes"—that compromise the mechanical integrity of the soil mass (Gilboy, 1933; Knappen and Philippe, 1936; Stearns et al., 1902). Together, these pioneering experiments laid the foundation for understanding seepage-driven particle transport and its crucial role in the long-term stability of embankments and other earth structures.

Despite limitations in early testing equipment, these studies made significant contributions to the development of soil mechanics and seepage theory. Over time, researchers recognized that water flowing through soil (seepage) can mobilize fine particles, gradually weakening the soil structure and causing hidden internal damage in embankments and dams (Beggs et al., 1938; Buchanan, 1938; Chowdhury, 1948; Terzaghi, 1939). This phenomenon of fine particle migration often remains undetected until structural deterioration or failure has already begun.

3.2 Refined testing

As the theory of soil mechanics advanced, experimental methods became increasingly precise, giving rise to more controlled geotechnical investigations. Standardized permeability tests were developed, with rigorous controls over sample preparation and hydraulic conditions. Researchers began to examine the role of soil microstructure and particle composition in fine particle migration, integrating these observations into mechanical models for analysis (Bendahmane et al., 2008; Fell et al., 2003).

Subsequent experiments carefully controlled parameters such as sample density, particle gradation, water pressure, and hydraulic gradient to investigate fine particle migration under diverse soil conditions. During this period, testing methods became more refined, allowing researchers to differentiate between various modes of particle transport. The incorporation of pore water pressure sensors enabled real-time monitoring of internal pressures, providing insight into the coupled interactions between seepage flow and particle detachment (Zhang et al., 2019).

Geotechnical centrifuge testing was increasingly applied to study fine particle migration in soils (Figure I .10). By using centrifugal forces to replicate gravitational stresses in large-scale systems, researchers could investigate particle movement mechanisms under conditions closer to real-world engineering scenarios. Centrifuge experiments generated data that more accurately reflected field-scale behavior, supporting a deeper understanding of how seepage-induced particle migration affects soil stability.

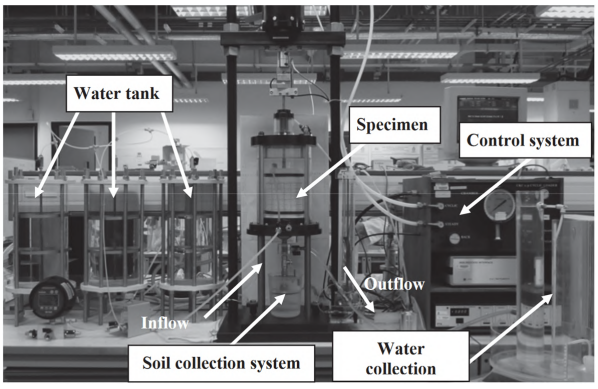

Figure I .10: Centrifuge test setup for studying fine particle migration in granular soils (Chang et al., 2012)

3.3 High-precision monitoring techniques and multiscale research

Contemporary research on fine particle migration in granular soils is increasingly moving toward high-precision, multidimensional investigations. Advances in laboratory equipment and monitoring technologies now allow researchers to characterize particle migration processes across multiple scales with unprecedented accuracy.

A key development is the application of X-ray computed tomography (CT) scanning (Figure I .11), which enables real-time visualization of microstructural changes during particle migration. CT scans allow detailed observation of fine particle detachment, pore network evolution, and localized structural weakening within the soil matrix. This non-destructive technique provides critical insights into the internal mechanisms driving particle transport and structural degradation (Nguyen et al., 2019).

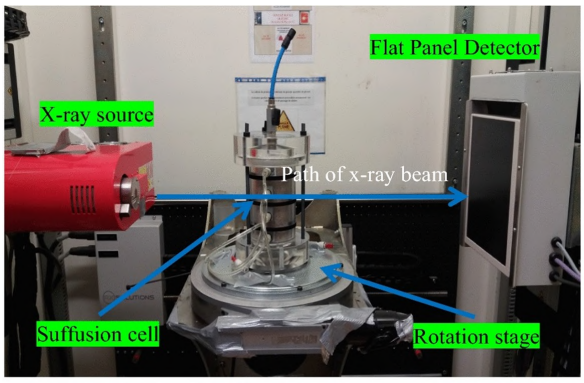

Figure I .11: Set-up of the suffusion cell inside the X-ray chamber (Nguyen et al., 2019)

In addition, microscopes and high-resolution cameras are employed to track particle interactions and fine particle loss in detail (Figure I .12). By integrating these tools with digital image analysis techniques, particle migration trajectories and local erosion rates can be quantified with high precision.

The miniaturization and enhanced accuracy of sensors now enable real-time monitoring of multiple parameters, including temperature, humidity, pressure, and displacement. Such continuous measurements provide valuable insight into the dynamic characteristics of particle migration under coupled hydro-mechanical conditions.

Modern experimental research thus integrates multiscale approaches, spanning from the particle scale to the macroscopic soil structure. Through combined experimental and numerical investigations, researchers can comprehensively study particle interactions, pore structure evolution, and localized stress redistribution during seepage-driven migration.

Although the critical influence of hydraulic gradient on fine particle migration is well

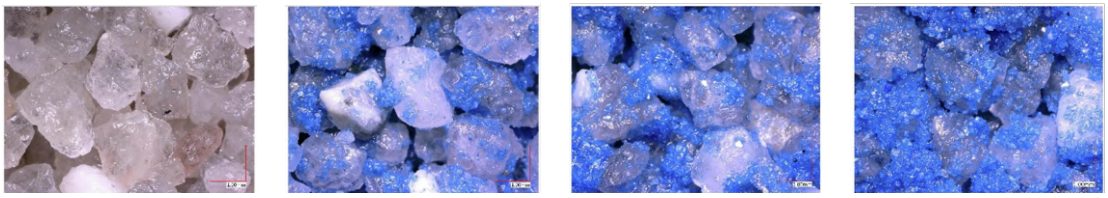

(a) (b) (c) (d)

Figure I .12: Microscopic observation of particle migration for granular soils with varying fine particle contents: (a) No filling; (b) 15% filling; (c) 20% filling; (d) 25% filling (Prasomsri et al., 2021)

established, systematic studies quantifying the effects of other physical parameters—such as soil uniformity, porosity, and particle size distribution—remain limited. In particular, controlled experiments assessing the combined impact of these factors are scarce, restricting a thorough understanding of particle migration processes under coupled fluid-particle interactions.

4 Numerical simulation methods for fine particle migration

The study of fine particle migration in granular soils involves complex hydro-mechanical processes. While experimental investigations are essential for understanding these mechanisms, they face limitations, particularly at the microscale. Consequently, numerical simulations have become a valuable complementary tool, enabling dynamic visualization of particle transport and reducing the time and cost associated with parametric studies. However, simple fluid models alone cannot fully capture the coupled interactions between soil particles and fluids. To address this, fluid-solid coupling methods have been developed (Figure I .13), which simultaneously simulate fluid seepage and the stress, deformation, and migration of soil particles, revealing the bidirectional effects between fluid and solid phases.

Because fine particle migration occurs in granular media, the Discrete Element Method (DEM) offers significant advantages for simulating such processes. DEM can accurately model collisions, friction, and interactions between individual particles, providing detailed dynamic depictions of particle movement at the microscale. When integrated with fluid-solid coupling, DEM enables more precise simulations of particle transport under seepage and stress. Based on this approach, several fluid-particle coupling frameworks have been developed, including PNM-DEM, CFD-DEM, LBM-DEM, and SPH-DEM models (Fig-

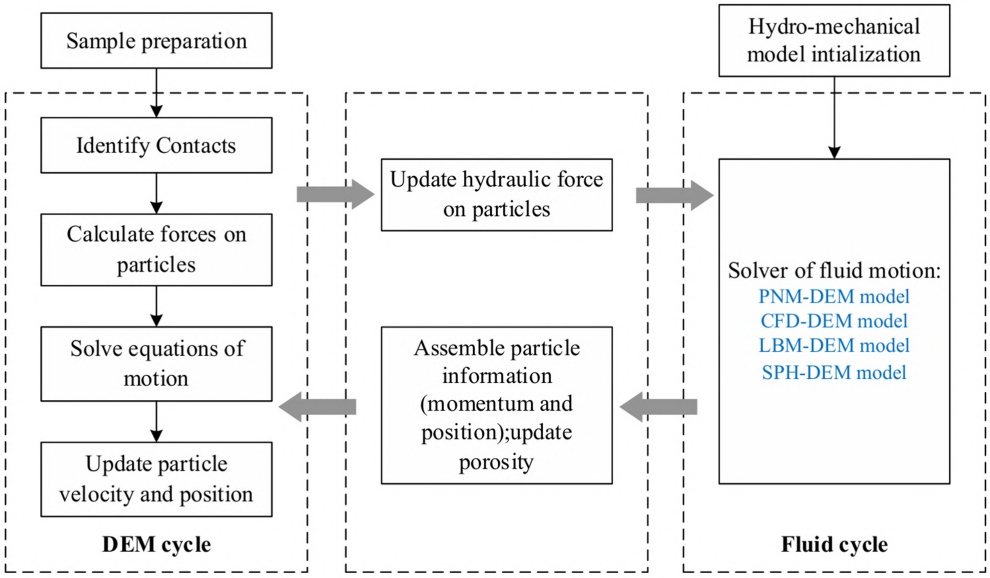

Figure I .13: Schematic of fluid-solid coupling methods for particle-fluid interaction

ure I .14). These models facilitate comprehensive multiscale and multiphysics simulations of fine particle migration in granular soils.

4.1 PNM-DEM model

The PNM-DEM model integrates the Pore Network Model (PNM), which simulates seepage behavior in soil, with the Discrete Element Method (DEM), which captures particle movement and interactions. This coupling provides a powerful tool for detailed simulation of fine particle migration in granular soils (Li et al., 2021; Wu et al., 2021). The model employs triangulation techniques to construct fluid grids, assuming that adjacent grids are connected through pores, enabling fluid exchange between them (Figure I .15).

Existing studies have shown that the PNM-DEM model can accurately simulate particle migration mechanisms across different soil types and pore structures (Sufian et al., 2019a; Zhu et al., 2023). The model is particularly effective for studying the scouring and transport of fine particles by fluid flow. Researchers have used the PNM-DEM framework to systematically investigate the effects of factors such as flow rate, hydraulic gradient, particle size, and particle shape on the initiation and evolution of fine particle migration (Frishfelds et al., 2011; Knight, 2018; Zhang et al., 2020).

These studies demonstrate how the progressive migration of fine particles alters the mechanical properties of the soil, potentially leading to localized structural weakening.

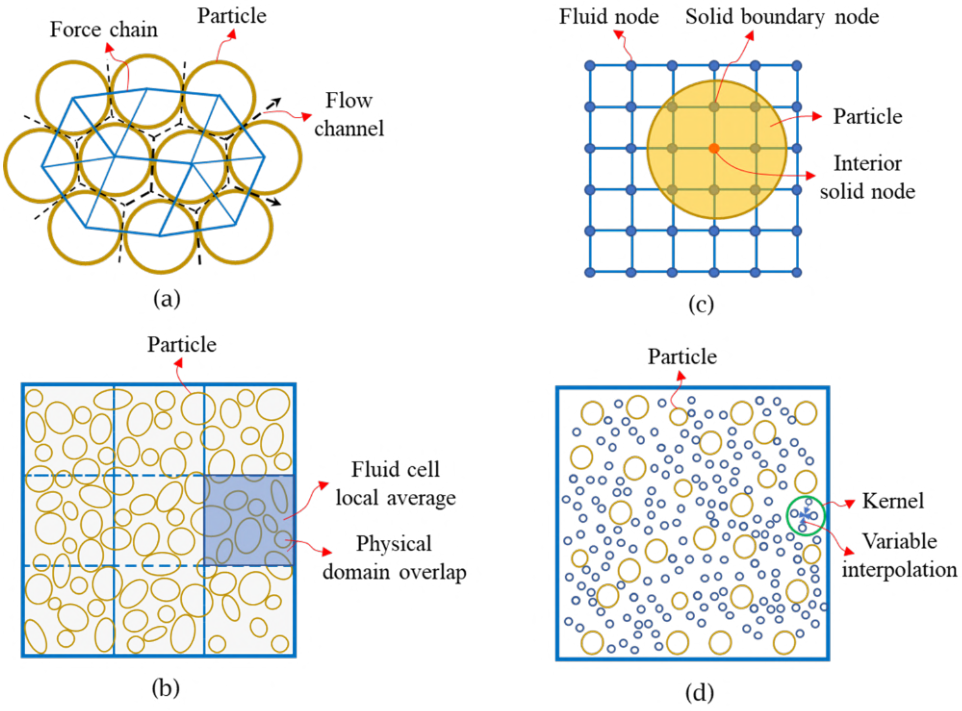

Figure I .14: Numerical methods for internal erosion in embankments: (a) PNM-DEM method; (b) CFD-DEM method; (c) LBM-DEM method; (d) SPH-DEM method (Wang et al., 2021)

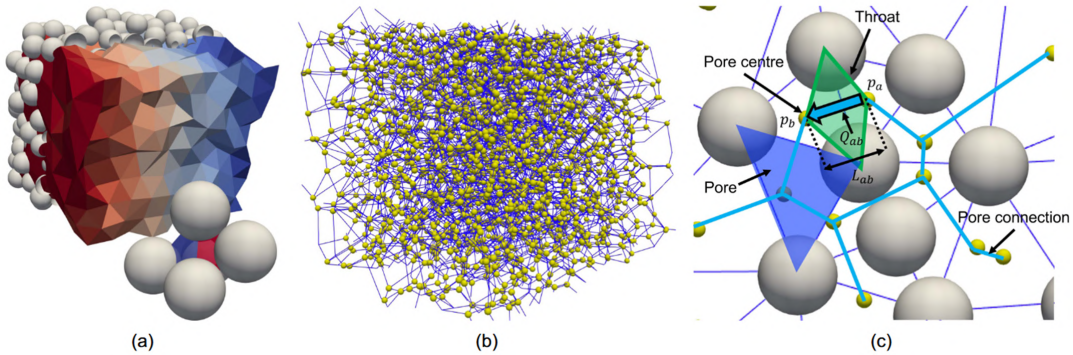

Figure I .15: PNM-DEM method: (a) Schematic illustration of discretization of the pore space using the weighted Delaunay triangulation and an example of two connected pore; (b) schematic illustration of the network with pores and pore connections (throats); (c) 2D schematic illustration of the PNM (Morimoto et al., 2024)

The PNM-DEM model has been partially validated against laboratory experiments, successfully simulating porosity changes and failure modes during localized particle transport

in embankments. The Dynamic Fluid Method (DFM), derived from Wu et al. (2020), further supports these findings.

In multiphase fluid environments, the PNM-DEM model offers a distinct advantage over traditional soil mechanics models, which often cannot simultaneously capture complex water–particle interactions. By incorporating the microscopic structure of porous media, the model represents the full process of particle detachment, migration, and redeposition (Sufian et al., 2019b).

This capability is crucial for understanding how fine particles gradually detach from the soil skeleton, how seepage modifies pore structures, and how localized weakening occurs in embankments under hydraulic loading (Xia et al., 2024). The PNM-DEM model has also been applied to study particle migration in various material combinations and geological conditions, including heterogeneous and fine-grained soils, enabling a more comprehensive analysis of complex soil-fluid interactions.

4.2 CFD-DEM model

The CFD-DEM (Computational Fluid Dynamics–Discrete Element Method) model simultaneously calculates fluid flow characteristics and particle mechanical motion. This approach enables detailed investigation of fine particle migration, the evolution of pore structures, and changes in local stress distribution during seepage-induced soil degradation (Gu et al., 2019; Liu et al., 2024b).

Previous studies have successfully employed the CFD-DEM model to replicate the full process of fine particle transport, the progressive formation of preferential flow paths, and subsequent soil instability (Wang et al., 2020; Yang et al., 2019b; Zhou et al., 2020a). The model can simulate the dynamic interaction of fluid and particles in soils with varying grain sizes, illustrating how particles are detached from pores under hydraulic forces and how migration pathways develop under different hydraulic gradients (Xiong et al., 2023; Yin et al., 2021; Zou et al., 2020).

In recent years, the CFD-DEM model has been widely applied to simulate various migration patterns, including backward erosion, concentrated leakage, and contact-induced particle transport (Cao et al., 2022). By coupling flow velocity fields, pressure distributions, and particle motion (Figure I .16), the model provides a scientific basis for identifying vulnerable zones in embankments and dams and supports the development of predictive models for particle migration-related instability. Furthermore, CFD-DEM has been used to evaluate how variations in particle size distribution, material composition, and hydraulic parameters at the embankment scale influence the rate and extent of particle transport,

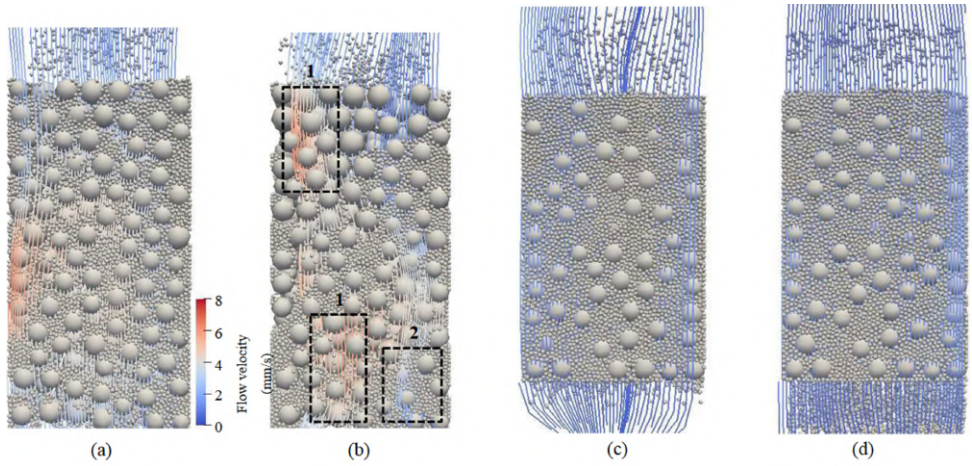

Figure I .16: Interaction between fine particles migration and fluid flow at the (a) initial time and (b) end of the simulation for the sample with $FC = 15\%$ and (c) initial time and (d) end of the simulation for the sample with $FC = 35\%$ under $i = 0.25$ and $C = 30$ g/L (Liu et al., 2021)

offering insights for erosion mitigation and disaster prevention (Figure I .17).

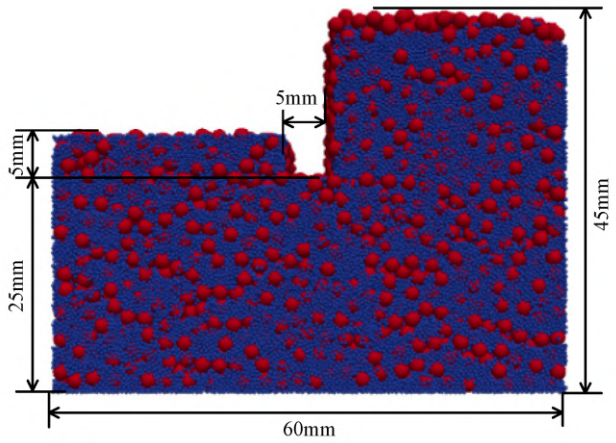

Figure I .17: CFD-DEM simulation of fine particle migration at the embankment scale (Xiao and Wang, 2020)

4.3 LBM-DEM model

The LBM-DEM (Lattice Boltzmann Method–Discrete Element Method) model has demonstrated significant potential for studying fine particle migration, particularly in capturing microscale particle-fluid interactions (Cui et al., 2021; Wang et al., 2016). By

combining the precise simulation of fluid dynamics provided by LBM with the mechanical representation of particle motion in DEM, the model effectively describes the entire process of particle detachment, pore structure evolution, and stress redistribution during seepage-driven particle migration (Figure I .18).

Using LBM, fluid flow in complex porous media can be simulated, while DEM tracks particle trajectories and mechanical responses. This combination provides detailed insights into migration mechanisms under different hydraulic conditions (Wang et al., 2017). For example, the LBM-DEM model can simulate how fluid mobilizes fine particles from pores, illustrating the progressive formation of preferential flow paths and the resulting localized weakening under hydraulic forces (Zhou et al., 2021).

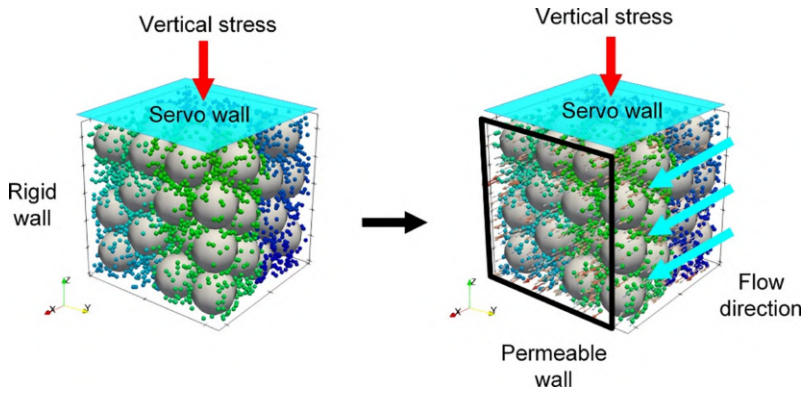

Figure I .18: LBM-DEM model describing fine particle detachment, pore structure evolution, and stress redistribution during particle migration (Zhou et al., 2020a)

In addition, the LBM-DEM model has advanced the study of permeability and porosity evolution (Ibrahim and Meguid, 2023). Researchers can monitor in real time how fine particle detachment alters pore structures and affects soil hydraulic properties (Figure I .19). The model is particularly useful for examining the scouring effects of water on particles of different sizes, revealing the coupled interactions between fluid flow and soil microstructure (Harshani et al., 2015). These studies improve understanding of how fluid-particle interactions influence soil strength and stability, providing numerical tools to evaluate the resistance of various soil types to particle migration.

In recent years, LBM-DEM has also been applied to simulate different particle migration scenarios, such as backward migration and contact-induced particle transport, further broadening its applicability (Scheuermann et al., 2019; Tran et al., 2017). Notably, the model can accurately capture the critical hydraulic gradient that triggers fine particle movement by coupling fluid pressure, velocity fields, and particle dynamics (Abdelhamid and El Shamy, 2016).

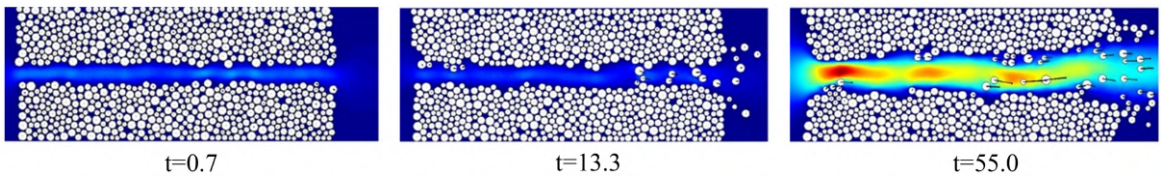

Figure I .19: Snapshots of a simulation of fine particle migration (at t = 0.7, 13.3, and 55.0 s from top to bottom). The colour scale represents the fluid velocity, while the translation velocity of solid particles is indicated by arrows (Sibille et al., 2016)

4.4 SPH-DEM model

The SPH-DEM (Smoothed Particle Hydrodynamics–Discrete Element Method) model has shown promising potential for studying fine particle migration, particularly in capturing complex interactions between fluids and particles (Ma et al., 2022). The model employs SPH to simulate fluid motion, representing the nonlinear behavior of fluids through particle interactions, while DEM describes the mechanical responses of solid particles (Bui and Nguyen, 2017; Mao et al., 2022).

The SPH-DEM framework can effectively simulate fine particle detachment, energy exchange between fluid and particles, and pore structure evolution during seepage-driven particle transport (Figure I .20). For example, Rao and Bai (2020) successfully applied this model to replicate the migration of fine particles under water flow, leading to the formation of localized voids within the soil matrix. These results provide valuable insights into the microscopic mechanisms of particle migration and the development of preferential flow paths under different hydraulic conditions.

The SPH-DEM model has also enabled detailed analysis of seepage behavior under various soil conditions. By accurately simulating fluid flow through granular media, researchers can evaluate how particle composition and hydraulic gradients influence particle migration, revealing pathways of transport and the development of flow channels (Feng et al., 2024). This capability enhances understanding of fluid–particle interactions and provides a valuable tool for assessing the resistance of soil structures to particle loss. In recent years, SPH-DEM has been applied under complex boundary conditions (Su et al., 2024; Zhang et al., 2023b), such as in designing erosion-resistant embankments and reservoirs, supporting the development of protective measures against fine particle migration.

Despite these advances, current numerical approaches for simulating fine particle migration in non-uniform soils still face challenges. Accurately capturing localized fluid-solid coupling, the dynamic transition between clogging and particle detachment, and the

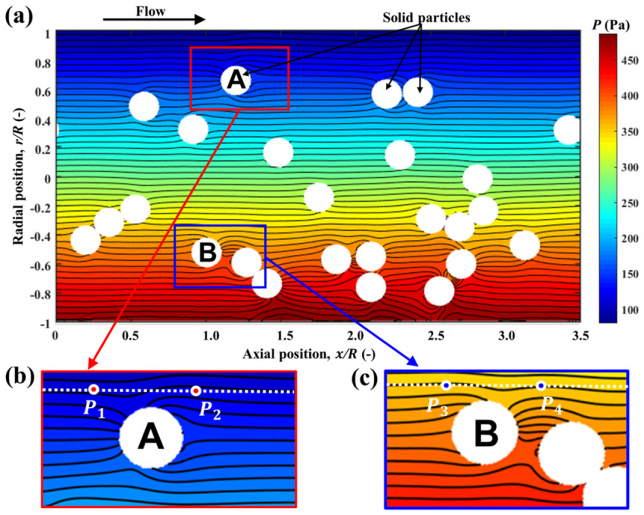

Figure I .20: Typical SPH–DEM predicted pressure field: (a) pipe flow on 1:1 scale; (b) enlarged pressure field around particle A; and (c) enlarged pressure field around particle B; $C_s = 10$ vol. %; P_1, P_2, P_3, and P_4 indicate local fluid pressure (Lian et al., 2023)

real-time evolution of pore structures under unstable seepage conditions remains difficult, highlighting the need for further model refinement.

5 Contributions of various factors to fine particle migration

5.1 The influence of hydraulic gradient

The hydraulic gradient is a critical factor governing fine particle migration, acting as the primary driving force for fluid flow through soil. Variations in the gradient directly affect the flow velocity and the hydrodynamic forces acting on soil particles, thereby controlling particle detachment and transport (Benamar et al., 2019). The magnitude of the hydraulic gradient determines the pressure difference and seepage intensity, which in turn influence the rate and extent of particle movement. Similarly, the direction of the gradient dictates the orientation of the applied forces, affecting where and how particles migrate. Therefore, evaluating both the magnitude and direction of the hydraulic gradient is essential for a comprehensive understanding of how seepage drives fine particle migration in granular soils.

5.1.1 Impact of hydraulic gradient magnitude

The magnitude of the hydraulic gradient directly influences the drag and shear forces exerted by the fluid on soil particles. As the gradient increases, seepage intensifies (Figure I .21), allowing the fluid to apply greater shear and drag forces, which makes particles more likely to be transported or eroded (Luo and Kong, 2016; Nguyen and Indraratna, 2020). In such cases, particle stability within the soil decreases, and the erosion rate increases significantly. In regions with high hydraulic gradients, the speed and volume of particle migration increase, which can even trigger localized instability within the soil structure (Rochim et al., 2017). For example, studies conducted by Chen et al. (2024) showed that under high hydraulic gradient conditions, the loss of soil particles becomes more pronounced, leading to greater erosion-induced structural instability and a significant reduction in overall stability.

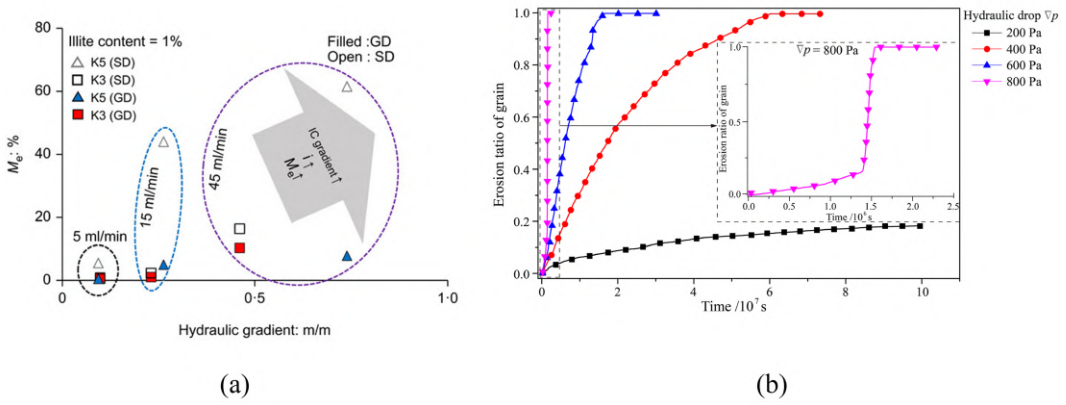

Figure I .21: Erosion mass increases with increasing hydraulic gradient: (a) For a changing (increasing) hydraulic gradient (Choe et al., 2024); (b) For a constant hydraulic gradient (Gu et al., 2019)

Conversely, under low hydraulic gradients, the seepage effect is weak, and particles tend to remain stable, with little observable erosion. Experimental studies have demonstrated that when the hydraulic gradient is low, the shear force generated by the flow is insufficient to transport particles, resulting in minimal erosion. The research by Mu et al. (2023) supports this, showing that when the hydraulic gradient falls below a certain threshold, the water flow's erosive effect on the soil is negligible, and most particles remain in place (Figure I .22).

However, it must be acknowledged that internal erosion varies under cyclic hydraulic gradients. Research has shown that under the same average hydraulic gradient level, the reversal of the hydraulic gradient leads to more severe erosion. also confirmed this in

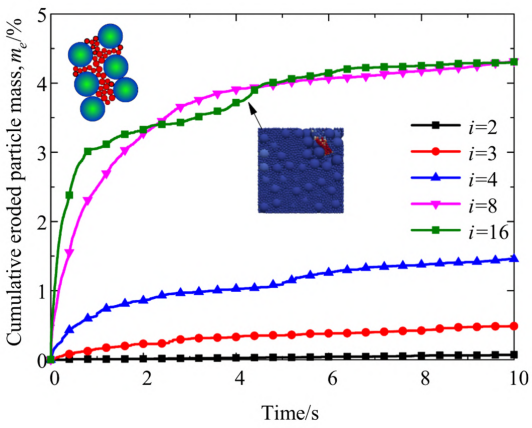

Figure I .22: The mass of cumulative eroded particles changes (30% fines content): The hydraulic gradient is very small ($i = 2$), the erosion rate is very small and almost no erosion occurs (Mu et al., 2023)

follow-up studies. This finding, to some extent, fills a gap in the existing knowledge.

However, it should be noted that internal erosion behaves differently under cyclic hydraulic gradients. Research has shown that even at the same average hydraulic gradient level, reversing the direction of the gradient can lead to more severe erosion (Xu et al., 2022). Chen and Zhang (2023) confirmed this in follow-up studies (Figure I .23). This discovery fills a gap in existing knowledge to some extent.

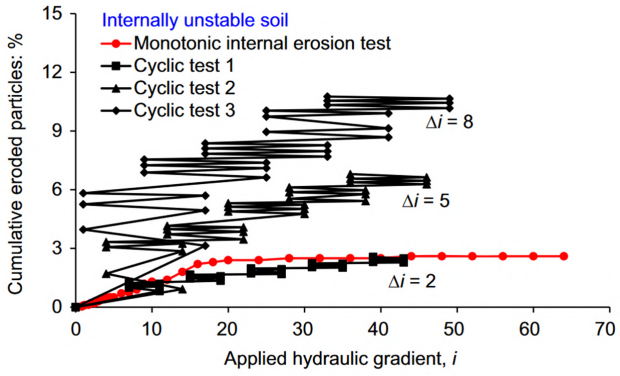

Figure I .23: Cumulative eroded soil mass with changing hydraulic gradient during the cyclic internal erosion test (Chen and Zhang, 2023)

The critical hydraulic gradient refers to the minimum hydraulic gradient at which particle loss begins, and it has garnered significant academic attention. When the hydraulic gradient is below the critical value, the forces generated by the flow are insufficient to

overcome the adhesive, frictional, and gravitational forces between particles, maintaining the stability of the soil structure (Bai et al., 2024; Liang et al., 2017). However, when the hydraulic gradient exceeds this threshold, the shear and buoyant forces exerted by the flow can dislodge fine particles, causing them to migrate downstream and initiate internal erosion (Xie et al., 2018). Research by Cheng et al. (2021) using numerical simulations and experimental tests revealed that the critical hydraulic gradient is closely related to soil properties (Figure I .24). For instance, soils with higher fine particle content tend to have a lower critical hydraulic gradient, making them more susceptible to erosion even under minimal seepage conditions (Liang et al., 2017).

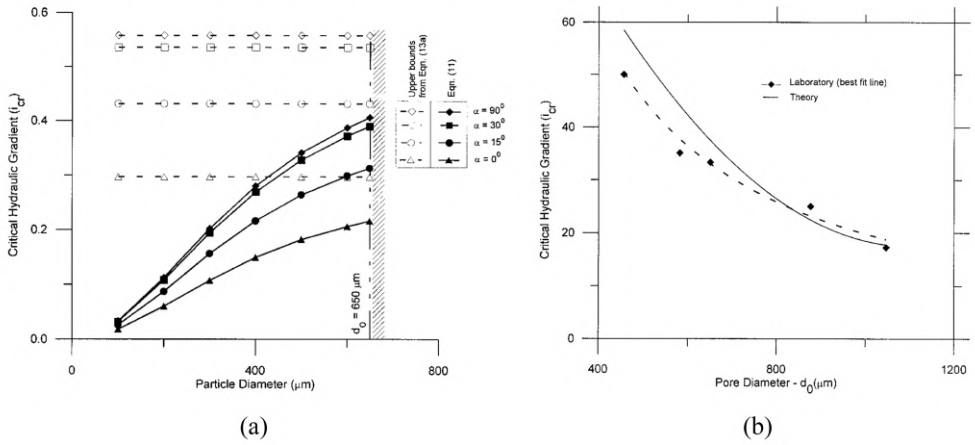

Figure I .24: Correlation between critical hydraulic gradient and soil characteristics: (a) critical hydraulic gradient versus particle diameter, where apha is the angle in the direction of the hydraulic gradient; (b) is the relationship between the hydraulic gradient and pore diameter (Indraratna and Radampola, 2002)

Furthermore, the interaction between confining pressure and hydraulic gradient also plays a crucial role in internal erosion. Studies indicate that while high confining pressure can suppress particle movement, erosion remains inevitable once the hydraulic gradient surpasses a certain level (Chen and Zhang, 2023). Research by Zhou et al. (2022) found that even under significant confining pressure, the energy of water flow at high hydraulic gradients can still cause particle loss within the soil. Therefore, in practical engineering applications, controlling the hydraulic gradient to prevent it from exceeding the critical value is one of the key strategies to mitigate internal erosion.

5.1.2 Influence of hydraulic gradient direction

The direction of the hydraulic gradient is a critical factor controlling fine particle migration. The gradient direction determines the flow paths of water through the soil, directly influencing the trajectories and patterns of particle transport (Marot et al., 2020; Pachideh and Mir Mohammad Hosseini, 2019).

Simulating inclined seepage in laboratory experiments remains challenging. Consequently, most studies focus on vertical seepage, where flow aligns with gravity, such as upward or downward seepage, often neglecting the effects of inclined flow. Migration behavior under inclined seepage may differ from vertical seepage because the resistance forces are no longer aligned with gravity (Ahlinhan and Adjovi, 2019; Li et al., 2023a).

Generally, particle migration rates increase as the seepage direction approaches vertical (Figure I .25). Numerical simulations indicate that when the hydraulic gradient interacts with soil heterogeneity, flow can concentrate along specific weak paths (Xiong et al., 2021b). The resulting localized increase in hydraulic gradient can enhance particle detachment and transport in certain areas, potentially leading to localized weakening or structural instability. Therefore, both the magnitude and direction of the hydraulic gradient not only control the intensity of particle migration but also determine its spatial distribution and development patterns (Zhou et al., 2020b).

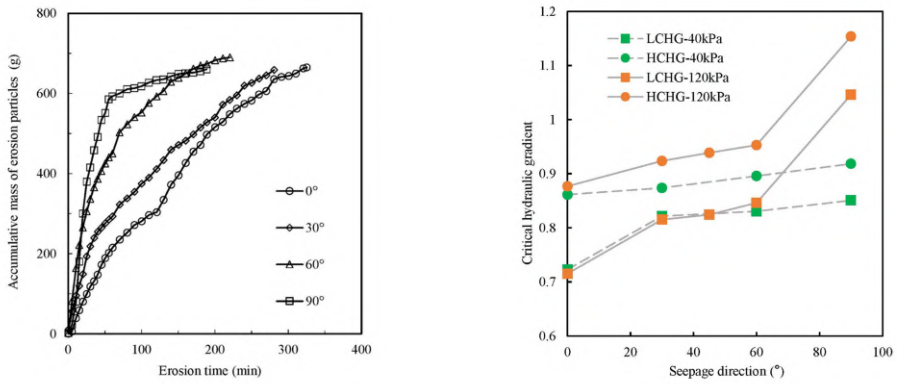

Figure I .25: The influence of seepage direction on cumulative erosion quality and critical hydraulic gradient: (a) The relationship between seepage angle and cumulative erosion quality; (b) The relationship between seepage angle and critical hydraulic gradient (Liang et al., 2020)

5.2 Influence of soil properties

Soil physical properties play a decisive role in fine particle migration, affecting fluid flow paths, particle stability, and the rate and patterns of particle transport. Different soil characteristics—such as initial porosity, particle size distribution, and fine particle content—exhibit varying sensitivities to particle detachment and migration, thereby influencing the evolution of soil structure under seepage.

5.2.1 Impact of initial porosity

Initial porosity quantifies the void space within soil and directly influences the formation of preferential flow paths and fluid velocity, thereby controlling the migration of fine particles. Recent studies have examined how porosity affects particle detachment and transport (Yang et al., 2019a). For example, Liu et al. (2018) found that higher porosity promotes the development of more flow channels, reducing resistance to fluid movement and accelerating fine particle migration (Figure I .26). Similarly, Liang et al. (2024) reported that soils with higher porosity exhibit faster rates of particle transport under seepage conditions.

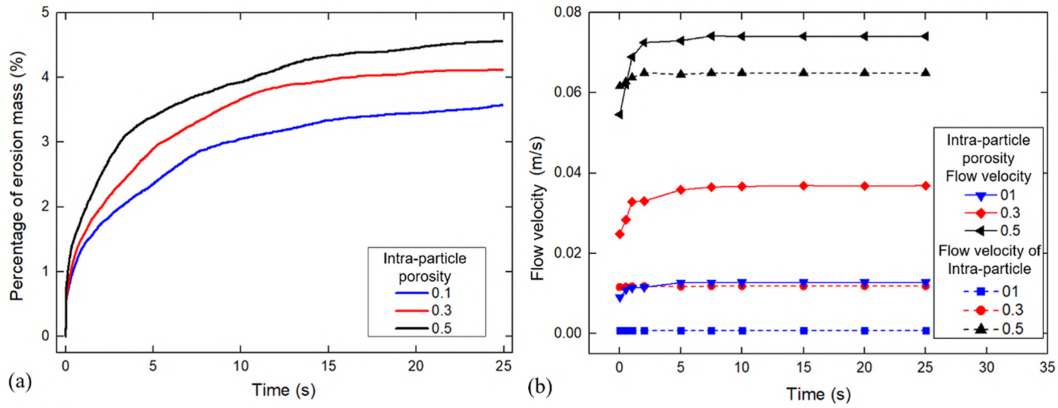

Figure I .26: Influence of initial porosity on fine particle migration: (a) normalized cumulative particle transport in gap-graded soil under different intra-particle porosity; (b) average fluid velocity during simulation (Wang et al., 2022a)

Porosity also affects the post-migration stability of the soil structure. Soils with high porosity that undergo significant particle loss experience a substantial reduction in load-bearing capacity, increasing the risk of local collapse or structural instability (Bedja et al., 2022). Conversely, low-porosity soils feature fewer flow paths, limiting fluid movement and enhancing particle stability, which reduces the extent of particle transport (Mao et al.,

2023). Changes in porosity during particle migration can further influence structural integrity, especially in high-porosity soils experiencing severe particle detachment, potentially leading to localized collapse or broader structural failure.

Overall, initial porosity plays a dual role in controlling fine particle migration and maintaining post-migration soil stability. Studies consistently indicate that lower porosity can mitigate the rate of particle transport and enhance the structural resilience of granular soils under hydraulic loading.

5.2.2 Impact of particle size distribution

Particle size distribution, which describes the range and proportion of particle sizes within soil, strongly influences fluid flow paths, particle stability, and the migration of fine particles (Figure I .27) (Hicher et al., 2018; Liu et al., 2024a). Numerous studies have explored how particle size distribution affects particle transport under seepage conditions (Zhang et al., 2020; Zhao et al., 2024).

Well-graded soils, containing a diverse mix of particle sizes, typically exhibit smaller voids due to interlocking between particles of different sizes. This reduces permeability and limits the migration of fine particles (Marot et al., 2016). The interlocking effect enhances soil stability by hindering particle detachment, thereby slowing particle transport (Yang and Wang, 2017).

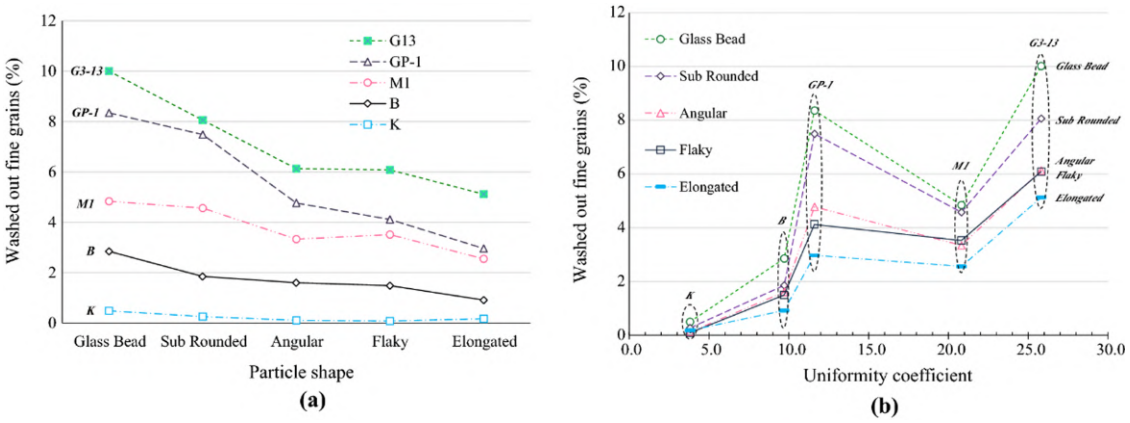

Figure I .27: Influence of particle size distribution on fine particle migration: (a) total particle transport for samples with different particle shapes; (b) total particle transport for samples with varying particle shapes and uniformity coefficients (Maroof et al., 2021)

In contrast, poorly graded soils, composed of uniformly sized particles, generally have larger voids and higher permeability, facilitating the formation of preferential flow paths. This promotes the migration and transport of fine particles (Guo et al., 2023; Oueidat

et al., 2021). Soils with uneven particle size distribution can also exhibit localized migration, as larger particles tend to remain stationary while finer particles are preferentially transported. This selective loss of fine particles can create voids, further enhancing localized fluid flow and accelerating particle migration (Bi et al., 2021; Deng et al., 2023a).

Studies consistently show that soils with a broad particle size range are more resistant to fine particle migration. Fine particles within the mixture can occupy void spaces between coarser grains, reducing the connectivity of flow paths and limiting particle transport (Zhang et al., 2020). Consequently, the overall soil structure remains more stable, and the progression of particle migration is mitigated.

5.2.3 Impact of particle shape

Particle shape is a crucial factor controlling fine particle migration and soil structure stability (Figure I .28). Studies show that irregular, angular particles interlock more effectively than round particles, enhancing friction between grains and stabilizing the soil matrix (Xiong et al., 2021a). The rough surfaces and sharp edges of angular particles reduce particle detachment and migration under fluid flow, thereby limiting the transport of fine particles (Qian et al., 2021). Angular particles are particularly effective in maintaining structural stability under low to moderate seepage rates.

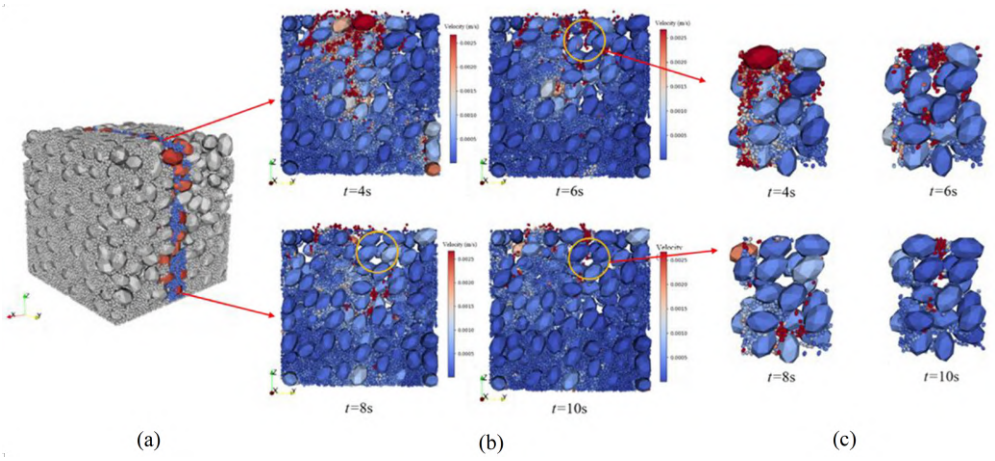

Figure I .28: Distribution of particles at different levels: (a) macroscopic level, (b) mesoscopic level, (c) microscopic level (Zhou et al., 2023a)

In contrast, round particles, which have smooth surfaces and weaker interlocking, are more easily mobilized by seepage flows. Under high-permeability conditions, water can move more freely between spherical particles, accelerating fine particle migration (Figure I .29) (Liu et al., 2024c). The detachment and transport of round particles are particularly

pronounced at higher flow pressures, resulting in more rapid changes to soil microstructure (Xiong et al., 2024). Consequently, the presence of rounded particles can increase the vulnerability of soils to particle migration under strong seepage conditions, potentially reducing overall structural stability.

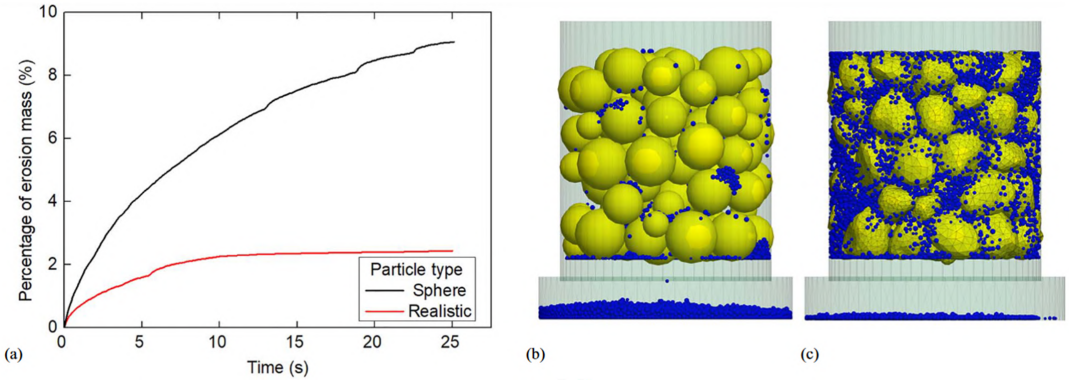

Figure I .29: Migration behavior of round particles under high-permeability conditions: (a) cumulative particle transport for realistic and spherical particle shapes; (b) comparison of fine particle transport for spherical particle model (Wang et al., 2023b)

5.2.4 Impact of fine particle content

The content of fine particles in soil strongly influences fluid flow paths, particle transport, and the overall stability of the soil structure (Figure I .30) (Liu et al., 2020; Yin et al., 2023). When present in moderate amounts, fine particles can fill voids between larger soil grains, reducing permeability and limiting fluid-induced particle migration (Li et al., 2020; Xiong et al., 2022). This filling effect enhances soil resistance to particle detachment and slows down fine particle migration by decreasing the ease of water flow through the pore network.

However, excessive fine particle content can have adverse effects on particle migration behavior. High fine content drastically reduces void space, increasing local flow velocities and pressure gradients within narrow pores (Figure I .31) (Ouyang and Takahashi, 2016; Zhao et al., 2024). Under these conditions, fine particles are more easily mobilized and transported, accelerating their loss from the soil matrix (Prasomsri and Takahashi, 2020).

Furthermore, Ahmadi et al. (2020) investigated the long-term effects of excessive fine particle content on soil stability. Their findings highlighted that the rapid loss of fine particles, especially under intense seepage conditions, can create localized erosion channels. Over time, these channels exhibit increased permeability, allowing more water flow

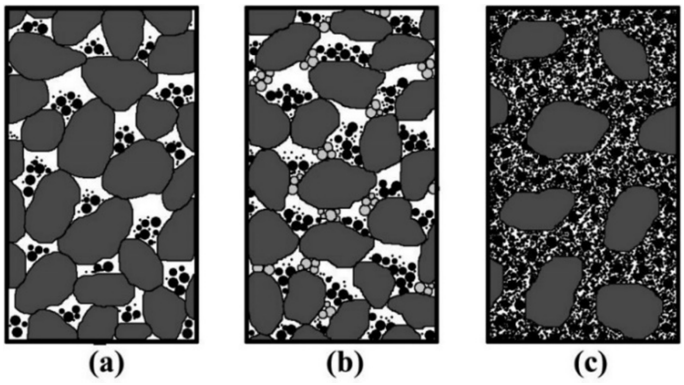

Figure I .30: Effect of fines content on the fines–coarse particles mixtures: (a) main soil skeleton (dark grey) and loosely distributed fine particles (black); (b) some of the fine particles that contribute to the main soil skeleton (light grey); (c) coarse-grained particles that have lost their contact (Dallo, 2021)

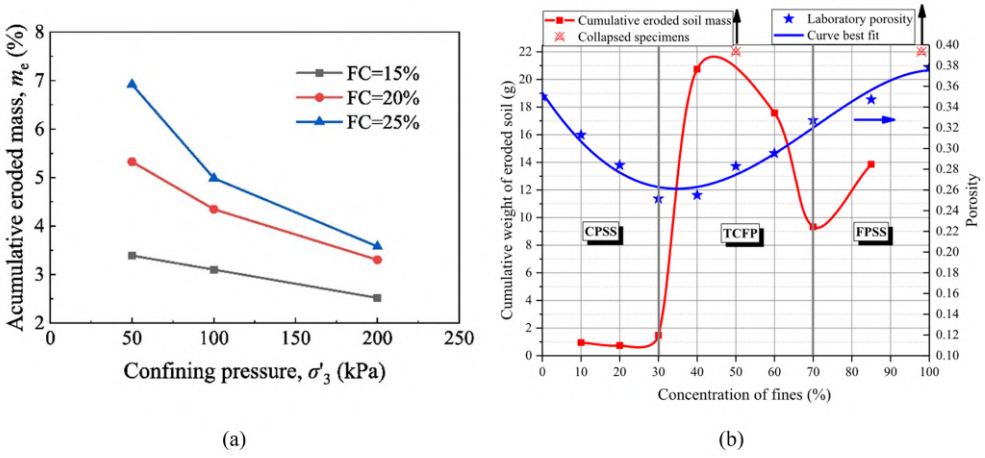

Figure I .31: (a) The cumulative eroded mass m_e after suffusion Liu et al. (2023a); (b) Evolution of cumulative weight of eroded soil with respect to fines content (Tian et al., 2020)

and accelerating internal erosion. Hu et al. (2019) concluded that once localized erosion channels are established, they significantly weaken the soil structure, increasing the risk of large-scale instability or failure.

While previous studies have identified key factors influencing the initiation of fine particle migration, such as fine content, porosity, and hydraulic gradient, the nonlinear and coupled interactions between these factors remain poorly understood. The lack of clarity regarding critical thresholds and their evolution under combined hydro-mechanical influences limits the development of accurate predictive models for particle migration in

granular soils.

6 Mechanisms of fine particle migration: effects of confining pressure and soil texture

6.1 Fine particle migration under confining pressure

Fine particle migration is strongly influenced by external stresses applied to soil structures, such as in dams and embankments. Confining pressure plays a critical role in controlling the movement of fine particles under hydraulic forces (Liang et al., 2019a). Researchers have studied how confining pressure interacts with hydraulic gradients to regulate particle detachment and transport, providing insights essential for mitigating soil instability in engineering applications (Deng et al., 2023b; Zhou et al., 2023b).

Laboratory experiments consistently show that increasing confining pressure reduces soil permeability and slows fluid flow, thereby inhibiting fine particle migration (Figure I .32). For example, Li et al. (2024) found that higher confining pressure compresses the soil matrix, decreases porosity, and narrows flow channels. This compression limits water velocity and reduces the kinetic energy available to mobilize particles (Zhang et al., 2020). These results indicate that confining pressure can effectively suppress particle migration by restricting both fluid flow and particle detachment, a mechanism leveraged in dam foundation projects to enhance soil stability (Kawano et al., 2018).

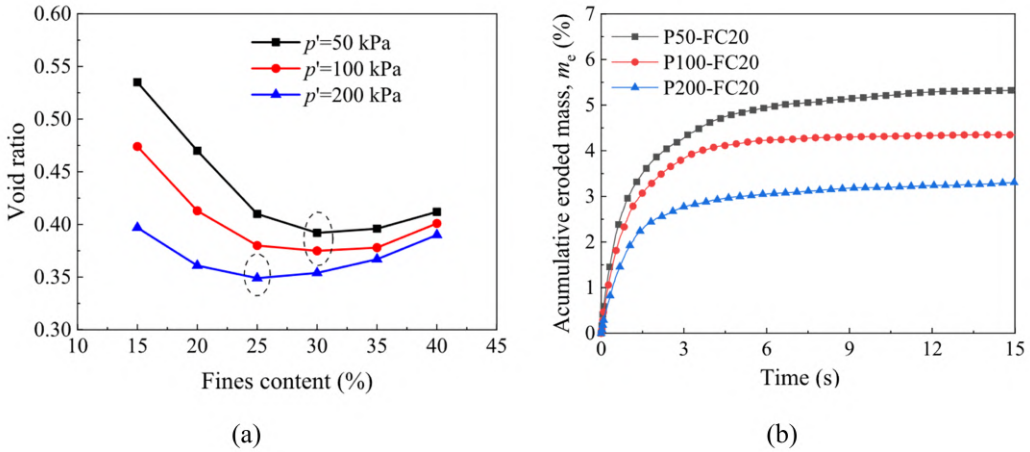

Figure I .32: Changes in porosity and erosion rate due to perimeter pressure: (a) Smaller porosity for specimens with high perimeter pressure; (b) Smaller erosion rate for specimens with high perimeter pressure (Liu et al., 2023a)

Further research on particle mobility has demonstrated that confining pressure enhances interparticle contact forces, reducing the likelihood of particle detachment and migration under water flow (Cao et al., 2024; Liu et al., 2020, 2023b). Chen et al. (2016) highlighted how elevated confining pressures increase friction between particles, making it more difficult for water flow to dislodge them. Numerical simulations have quantified the forces acting on particles, showing that higher confining pressure requires significantly greater water forces to initiate particle movement.

Moreover, the influence of confining pressure on shear strength is a critical factor in studies of fine particle migration and internal erosion (Hu et al., 2020; Liang et al., 2019b). According to the Mohr-Coulomb failure criterion, a soil's shear strength increases with normal stress, a relationship that has been extensively validated in erosion-related research. Experimental and numerical studies (Hu et al., 2023; Luo et al., 2020) have shown that higher confining pressures enhance soil resistance to shear forces, particularly under elevated hydraulic gradients, thereby delaying the initiation of particle migration. Additionally, Li et al. (2023b) demonstrated that soils subjected to higher confining pressures exhibit greater tolerance to shear-induced deformation, reducing the risk of particle migration and structural weakening even under significant water flow conditions.

Recent research on the critical hydraulic gradient has further clarified the role of confining pressure (Chen et al., 2023). Zhang et al. (2023a) conducted combined experimental and numerical studies to assess how confining pressure affects the critical gradient—the threshold at which water forces overcome interparticle resistance. Chang et al. (2020) observed that increasing confining pressure raises the critical hydraulic gradient (Figure I .33), indicating that stronger seepage is required to initiate particle detachment and subsequent soil displacement (Zhou et al., 2022).

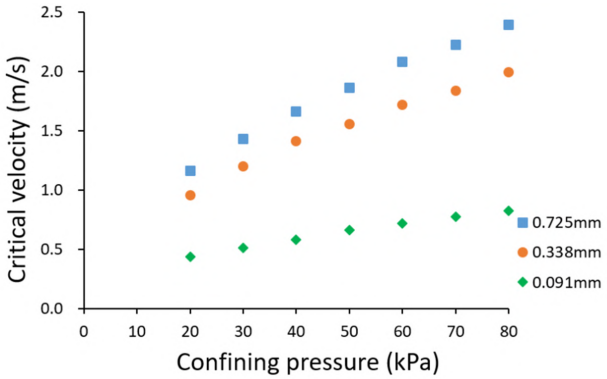

Figure I .33: Critical velocity with various confining pressure with different particle size (Luo et al., 2013)

6.2 Influence of soil texture on soil stability and particle migration

The mechanical texture of soil particles, particularly their hardness and stiffness, plays a critical role in controlling particle stability and migration under seepage conditions. Unlike commonly recognized factors such as gradation or shape, particle hardness governs how grains respond to intergranular stress and fluid-induced forces.

Experimental observations indicate that soils composed of softer particles, such as clay aggregates or weakly cemented silts, are more prone to deformation, abrasion, or fracture under hydraulic gradients. These processes contribute to the generation of fines and modify the pore structure, potentially facilitating preferential flow paths and localized particle movement (Liu et al., 2023a).

In contrast, harder particles, such as quartz-rich sands or crushed angular gravels, retain their integrity under similar seepage conditions. Their higher stiffness enhances the stability of interparticle contacts and reduces the likelihood of particle displacement. Additionally, hard particles are less prone to generate fines under stress, helping maintain a more stable pore network and slower particle migration rates.

Numerical simulations using the Discrete Element Method (DEM) and coupled fluid-particle models, such as DEM-PFV and DEM-DFM, confirm that the threshold force required to mobilize soft particles is significantly lower than that for hard particles. For example, Chen et al. (2025) showed that under identical boundary conditions, soft particles exhibit lower critical hydraulic gradients and higher migration velocities, accelerating structural rearrangement.

Furthermore, particle hardness affects the development of stress chains under confining pressure (Figure I .34). Soft particles are more likely to undergo localized rearrangement and fragmentation, altering porosity and facilitating the formation of preferential migration pathways. In contrast, hard particles preserve the structural skeleton of the soil matrix, enhancing overall stability.

These findings underscore the importance of considering the mechanical properties of soil particles at the micro-scale when evaluating particle mobility and structural stability. In practical applications, selecting harder backfill materials or improving the hardness of weak soils can be an effective strategy to mitigate the risk of particle displacement under seepage.

Most existing studies emphasize particle size and gradation, with limited attention to mechanical texture such as stiffness and hardness. Moreover, the combined influence of material texture and confining pressure on force chain development and failure modes has not been adequately explored at the microscale, leaving a critical gap in understanding

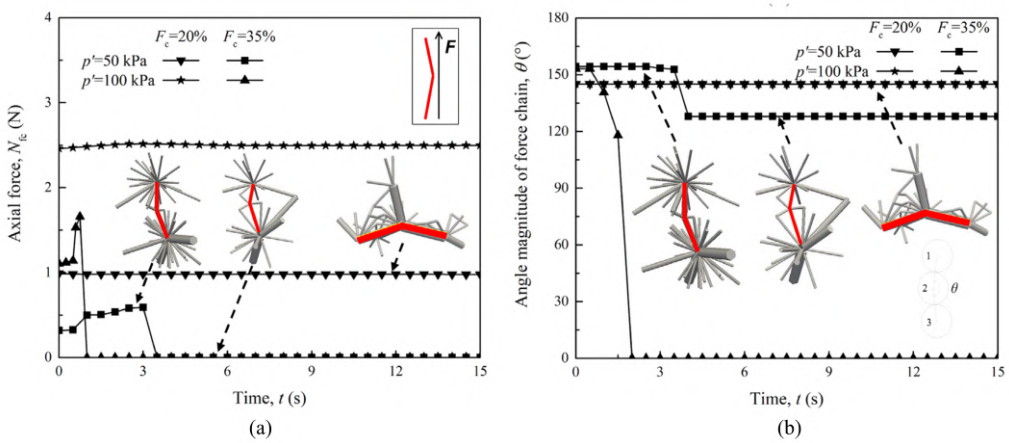

Figure I .34: Evolution of (a) axial force and (b) angle magnitude for a typical force chain in samples with different FC (20% and 35%) and p' (50 and 200 kPa). An angle of 0° means that the contact is separated. (Liu et al., 2020)

the formation of preferential migration pathways and structural stability.

7 Conclusions

This introductory chapter has laid the foundation for understanding particle mobility and soil structural responses under seepage by reviewing microstructural characteristics, particle migration types, experimental observations, and current numerical modeling approaches. The chapter highlights the significance of micro-scale mechanisms in driving instability and identifies critical research gaps in linking soil microstructure, hydraulic conditions, and particle migration. In particular, challenges remain in accurately quantifying thresholds for particle detachment, capturing particle-scale interactions under transient flow, and simulating coupled fluid-solid behavior across diverse soil textures and stress states.

To address these challenges, the following chapters systematically integrate experimental and numerical methods.

- Chapter III develops and validates a hybrid DFM-DEM numerical model that simulates particle migration at the pore scale. The model captures suffusion mechanisms and grid adaptability under varying particle arrangements.

- Chapter IV applies the validated numerical approach to explore the effects of initial porosity, hydraulic loading, and fine particle content on migration patterns. It

also highlights clogging dynamics and permeability evolution, providing quantitative insights into soil structure degradation.

- Chapter V incorporates mechanical confinement and material texture effects into the coupled analysis. The resulting simulations provide a comprehensive understanding of how hydraulic and mechanical factors interact to influence particle mobility and structural stability in gap-graded soils.

- Chapter VI concludes the thesis by summarizing key findings, evaluating limitations, and proposing future research directions to advance the understanding and modeling of particle migration and soil stability under seepage conditions.

These chapters aim to enhance predictive capabilities and contribute to the design of more resilient geotechnical systems.

Chapter II

Experimental Investigation of Internal Erosion

1 Introduction

Particle migration within a soil matrix under hydraulic forces is a critical process in geotechnical engineering, leading to changes in porosity, permeability, and overall soil stability. This mechanism plays a key role in the performance and potential failure of earth structures, such as dams, levees, and slopes, contributing to phenomena like piping and landslides. Despite extensive research, predicting soil instability driven by particle migration remains challenging due to variability in soil structure, including particle size distribution, pore connectivity, and hydraulic conditions. Existing studies have highlighted the influence of soil gradation, hydraulic gradients, and stress conditions on particle mobility, yet inconsistencies in stability criteria and the absence of a unified predictive framework underscore the need for further research through theoretical analysis, numerical modeling, and experimental validation. Moreover, while various numerical models are available, their reliability strongly depends on high-quality experimental data, particularly regarding particle migration mechanisms and pore structure evolution.

This chapter addresses these challenges by conducting cylindrical seepage tests to investigate the effects of hydraulic gradient, particle size distribution non-uniformity, and porosity on seepage velocity and particle transport. Imaging techniques were employed to observe particle migration under transient flow conditions. A modified stability assessment method that integrates porosity and particle size distribution is proposed.

The chapter is structured as follows: First, the experimental setup and procedures are described in detail, including materials, testing protocols, and experimental design.

This is followed by a presentation of results and discussion, providing insights into the evolution of permeability, particle movement, and filtration behavior patterns observed during testing. Finally, a refined stability assessment method is proposed based on the experimental findings, enhancing predictive capabilities by incorporating both porosity and particle size distribution.

2 Experimental setup and procedure

2.1 Experimental apparatus

To investigate the migration behavior of fine particles in granular materials under seepage, a custom-designed visualization apparatus was developed, as illustrated in Figure II .1. The apparatus consists of four main components: a water supply system, a transparent specimen column, an image acquisition system, and a particle collection unit.

The water supply system (6) comprises a constant head tank and an overflow pipe (2), allowing the hydraulic gradient to be adjusted and maintained at stable levels. The transparent specimen experiment chamber colum (8) is made of acrylic, which enables direct observation of particle behavior during seepage. Coarse sand filters (7) and fine mesh screens (1) are installed at both the top and bottom of the column to ensure even water distribution and to prevent particle loss. The image acquisition system (9 and 13) enables real-time and localized visualization during the test process, and the particle collection unit at the base of the column captures and measures the eroded fine particles.

The specimen column has a diameter of 10 cm and a height of approximately 25 cm, providing a sufficient aspect ratio to minimize boundary effects. The column is filled with granular mixtures (4) of varying gradations, and coarse sand layers (2 cm thick, particle size $>$ 2 mm) are placed at both the top and bottom to distribute flow and stabilize the sample. Stainless steel perforated plates with 2 mm-diameter holes, arranged at 3 mm intervals, are placed above and below the specimen to promote uniform flow while preventing clogging. All water channels and connectors used in the system have an inner diameter of 7.5 mm.

To simulate different seepage conditions, the hydraulic gradient was adjusted by varying the overflow pipe height, with target gradients set at 0.2, 1.0, and 1.8. For visual observation, the image acquisition system includes a 5 MP digital CMOS camera with a maximum frame rate of 30 fps, positioned in front of the specimen column to record the entire testing process. In addition, three USB microscopes (9) with up to 500$\times$ magnification and 25 fps recording capability are mounted at fixed positions corresponding to

heights of 4 cm (top), 12.5 cm (middle), and 21 cm (bottom), enabling high-resolution imaging at multiple vertical layers within the specimen.

2.2 Materials and specimens

The granular material used in the tests was fused quartz sand (Figure II .2(a)), chosen for its transparency and strength, which makes it suitable for visual observation and comparable in properties to typical levee fill materials. The quartz sand (Figure II .2(b)), obtained from Xuzhou in Jiangsu Province, is hard, well-rounded, and chemically stable. To track the movement of fine particles during erosion, red-dyed fine sand with a $CaCO_3$ base was used as tracer particles. These tracers have particle diameters smaller than

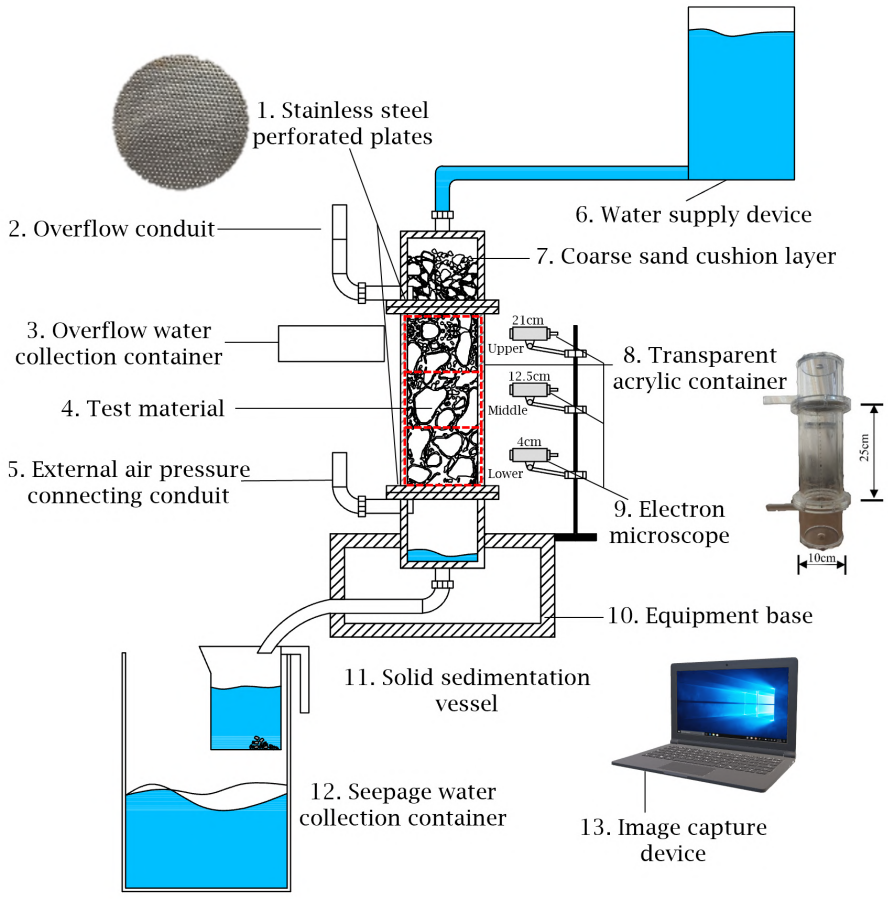

Figure II .1: Schematic presentation of the seepage experimental device

0.25 mm and were added in specific quantities to avoid influencing the hydraulic flow or mechanical response of the bulk material.The properties of the tested materials are summarized in Table II .1.

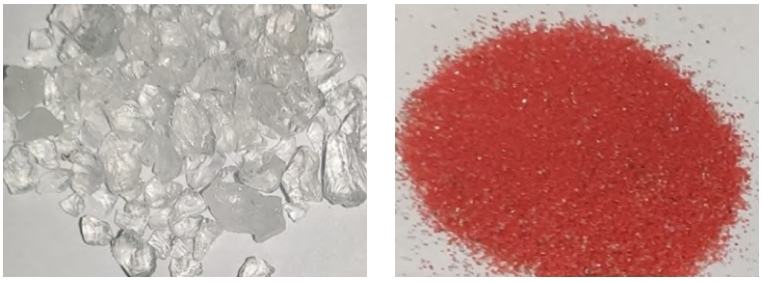

(a) (b)

Figure II .2: Experimental Materials: (a) Transparent fused quartz sand; (b) Red tracer sand

Table II .1: Quartz sand and color sand parameters

Criterion	Quartz sand	Red tracer sand
Main components	SiO_2 (99.9–99.95%), Fe_2O_3, Li_2O, Al_2O_3	$CaCO_3 \geq 98\%$
Density	2.65 g/cm^3	2.71 g/cm^3
Moisture	<0.05%	<0.2%
Mohs hardness	7.0	3.0
pH value	7.0	8.0
Elastic modulus (E)	10.0 GPa	1.0 GPa
Poisson's ratio (ν)	0.25	0.30

All quartz sand used in the tests was oven-dried and sieved into the following particle size fractions: 10–5 mm, 5–2 mm, 2–1 mm, 1–0.5 mm, and 0.5–0.25 mm. To simulate fine particle migration under seepage, additional red-colored tracer sand (composed primarily of $CaCO_3$) was incorporated. The red tracer particles were all smaller than 0.25 mm and were blended into the mixtures in designated proportions. Specifically, red tracer sand was used to represent two distinct size groups: 0.25–0.75 mm and ≤0.25 mm, in order to enhance visual tracking of fine particle movement during seepage-driven migration. Three target porosity levels were considered: 0.30, 0.35, and 0.40, to investigate the effect of initial void ratio on particle migration behavior.

Table II .2: Coefficient of non-uniformity and curvature coefficient for composite materials

Gradation	Coefficient of uniformity (C_u)	Coefficient of curvature (C_c)	d_{10}	d_{20}	d_{30}	d_{60}	d_{70}
B1	2.95	1.07	0.32	0.46	0.57	0.95	1.62
B2	14.78	0.52	0.35	0.53	0.97	5.19	6.12
B3	20.47	9.71	0.36	0.68	5.02	6.74	7.44

The coefficient of uniformity ($C_u = d_{60}/d_{10}$) and the curvature coefficient ($C_c = d_{30}^2/(d_{10}\cdot d_{60})$) serve as key indices for characterizing particle size distributions and evaluating their influence on migration patterns. A gradation is typically considered well-graded and continuous when $C_u \geq 5$ and C_c lies within the range of 1 to 3. According to previous experimental studies, materials with $C_u \leq 5$ tend to exhibit global particle migration, where detachment and transport occur throughout the entire sample. In contrast, when $5 < C_u < 10$, both global migration and localized channel formation may develop, depending on the pore structure and flow conditions. For highly non-uniform mixtures with $C_u > 20$, localized channels and selective transport of fine particles become the dominant modes, owing to the discontinuous packing and high contrast between coarse and fine fractions. These parameters are widely used to predict the susceptibility of granular media to particle migration under seepage.

Based on these considerations, three representative artificial gradations were designed to investigate the role of particle size distribution in controlling migration mechanisms. Gradation B1 was characterized by a relatively narrow size range, with $C_u = 2.95$, representing a uniform structure composed of similarly sized particles. This configuration promotes a stable granular skeleton, reducing the likelihood of particle movement during seepage. Gradation B2 had a broader particle size distribution and a gap-graded structure, with $C_u = 14.78$, where fine particles partially filled the voids between coarser grains, providing an intermediate scenario between uniformity and heterogeneity. Gradation B3, with $C_u = 20.47$, featured the widest size range and a pronounced discontinuity in particle arrangement. The large disparity between coarse and fine fractions in this mixture weakened the contact network and increased the vulnerability to localized channels and selective migration of finer particles under elevated hydraulic gradients.

The grain size characteristics of all tested mixtures, including d_{10}, d_{30}, d_{60}, C_u, and

C_c, are summarized in Table II .2. The corresponding grain size distribution curves are shown in Figure II .3.

2.3 Experimental procedures

To achieve the designated porosity levels, the total dry mass of the mixed sand (M_0) was calculated based on the target dry density (ρ_d) and the fixed specimen volume (V) using the relation $M_0 = \rho_d \cdot V$. For each porosity level, this ensured precise control over the initial packing condition.

The mass of each particle size fraction was then determined according to the prescribed gradation curve (mass percentage), and each fraction was weighed individually using an electronic balance. The weighed components were thoroughly mixed before packing to achieve a uniform distribution.

The mixture was then packed into the specimen column using a layered eposition method with light tapping and slight under-compaction to ensure homogeneity. Each layer (approximately 5 cm thick) was compacted to slightly below the target density. The final porosity was verified by measuring the total mass and dimensions of the specimen. This method has been shown to yield consistent and reproducible porosity distributions in previous studies (Chang and Zhang, 2011).

After specimen preparation, a 2 cm-thick layer of coarse sand was placed on top to help distribute the inflow uniformly and reduce turbulence during saturation. Water was introduced slowly from the top, and the specimen was allowed to saturate naturally under

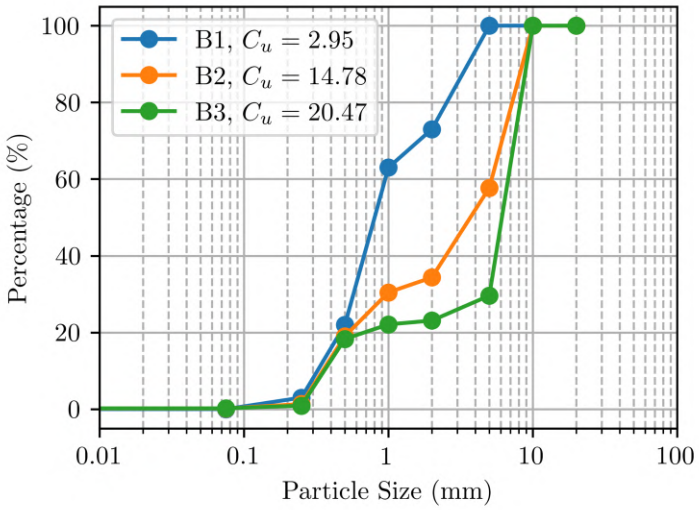

Figure II .3: The particle size distribution curves of the mixed materials in group B

gravity. Saturation was considered complete when a steady water head was observed at the outlet, typically within 30 to 60 minutes depending on gradation and porosity.

The hydraulic gradient was incrementally increased to investigate the evolution of particle migration in granular soils under controlled seepage conditions. The initial gradient was set to 0.2 and incrementally increased by 0.2 up to a maximum value of 2.0. The hydraulic gradient (i) was calculated from the head difference between the inlet and outlet, divided by the specimen height. A gravity-fed setup was employed, wherein the inlet water level was manually adjusted by raising or lowering the water reservoir, and the outlet was fixed at a constant height to maintain a stable outflow condition. Although a Mariotte bottle was not used, the gradual head adjustments and visual monitoring ensured precise control of the seepage process without introducing significant fluctuations.

At each gradient level, the Darcy velocity (v) was used to characterize the seepage behavior and fluid movement through the soil. It was calculated using the equation:

$$v = \frac{Q}{A} \tag{II .1}$$

where Q is the volumetric outflow per unit time (cm^3/s), and A is the cross-sectional area of the sample (cm^2). This flow velocity served as a direct indicator of seepage intensity and potential particle migration development.

Each gradient level was maintained for 20 minutes. During this period, flow rate, effluent turbidity, and internal changes were continuously monitored. The particle migration process at each stage was considered stabilized when both the flow rate and the clarity of outflow water became steady. A sudden increase in turbidity or visible instability in the specimen indicated the onset of particle migration.

The hydraulic gradient was increased in a stepwise manner to assess the progression of fine particle migration under controlled seepage conditions. The initial gradient was set to 0.2 and incrementally increased by 0.2 up to a maximum value of 2.0. The hydraulic gradient (i) was calculated from the head difference between the inlet and outlet, divided by the specimen height. A gravity-fed setup was employed, wherein the inlet water level was manually adjusted by raising or lowering the water reservoir, and the outlet was fixed at a constant height to maintain a stable outflow condition. Although a Mariotte bottle was not used, the gradual head adjustments and visual monitoring ensured precise control of the seepage process without introducing significant fluctuations.

Each gradient level was maintained for 20 minutes. During this period, flow rate, effluent turbidity, and internal changes were continuously monitored. The particle migration process at each stage was considered stabilized when both the flow rate and the clarity of

outflow water became steady. A sudden increase in turbidity or visible instability in the specimen indicated the onset of particle migration.

To capture localized particle migration processes, three USB microscopes with up to 500× magnification and 25fps recording capability were mounted at fixed vertical positions along the column, corresponding to heights of 4cm (bottom), 12.5cm (middle), and 21cm (top). These heights were selected to monitor particle dynamics across the vertical profile of the specimen, with particular attention to fine particle mobilization under upward seepage. Throughout the test, the images and videos from each microscope were reviewed in real time to identify early signs of fine particle migration, such as particle detachment, formation of micro-channels, or color changes induced by tracer particle displacement.

When potential migration activity was observed at any of the monitored levels, the corresponding microscope's focus was manually fine-tuned using an integrated adjustable mount. The field of view was centered on the region of interest to track particle movement trajectories. This allowed the onset, progression, and directionality of fine particle migration to be accurately captured. The fixed positioning also enabled temporal comparison between different test stages.

Due to the cylindrical shape of the column and curvature-induced image distortion, all recorded images were post-processed using MATLAB to apply lens distortion correction and spatial flattening. This ensured that the visual analysis of particle movement was not compromised by geometric artifacts and provided a reliable basis for tracking fine particle migration evolution

The test continued in this stepwise manner until significant particle migration was observed or the upper limit of the hydraulic gradient was reached. After each stage, eroded particles carried out by the seepage flow were collected using a fine mesh at the outlet, oven-dried at 105 °C for 24 hours, and weighed to determine the mass of eroded soil. The cumulative mass migration rate (m_e) was calculated as:

$$m_e = \frac{M_e}{M_0} \times 100\% \tag{II .2}$$

where M_e is the cumulative mass of eroded particles (g), and M_0 is the initial dry mass of the specimen (g).

After the test was completed, the specimen height was measured and evenly divided into three sections, corresponding to the upper, middle, and lower parts defined in Figure II .1. Each section was carefully extracted to minimize disturbance. After drying, the grain size distribution of each part was remeasured.

To systematically analyze the effects of gradation, porosity, and hydraulic gradient

on particle migration, a response surface methodology (RSM) was applied using *Design-Expert* software. The mass migration rate, expressed as mass loss per unit time, was selected as the response variable. A total of 17 tests (labeled T1 through T17) were designed, as shown in Table II .3.

Table II .3: Response surface design of soil particle migration test parameters

Number of tests	Coefficient of nonuniformity (C_u)	Gradation	Porosity (n_0)	Hydraulic gradient (i)
T1	$0-5$	B1	0.30	1.0
T2	$10-15$	B2	0.35	1.0
T3	$0-5$	B1	0.35	1.8
T4	$10-15$	B2	0.35	1.0
T5	$10-15$	B2	0.30	1.8
T6	$10-15$	B2	0.30	0.2
T7	$0-5$	B1	0.40	1.0
T8	$10-15$	B2	0.35	1.0
T9	$10-15$	B2	0.40	0.2
T10	$20-25$	B3	0.40	1.0
T11	$0-5$	B1	0.35	0.2
T12	$20-25$	B3	0.35	0.2
T13	$10-15$	B2	0.40	1.8
T14	$10-15$	B2	0.35	1.0
T15	$20-25$	B3	0.35	1.8
T16	$20-25$	B3	0.30	1.0
T17	$10-15$	B2	0.35	1.0

3 Results and discussions

3.1 Permeation development characteristics

3.1.1 Relationship between incremental hydraulic gradient and permeation development

Based on the results of the cylindrical infiltration tests conducted under varying hydraulic gradients, the relationship between Darcy velocity (v) and hydraulic gradient (i) was established, as illustrated in Figure II .4. The overall trend of the outflow behavior indicates a nonlinear increase in velocity with increasing gradient. The measured flow velocities ranged from 0.092 to 0.365 cm/s across the tested gradient range, indicating a progressive increase in seepage intensity and the potential initiation of particle migration.

In the initial stages of the experiment, under relatively low hydraulic gradients, a phenomenon of seepage-induced compaction was observed. During this phase, the flow velocity decreased slightly despite the increase in hydraulic head, as the upward seepage caused a rearrangement of particles and a reduction in pore space. As the hydraulic gradient continued to rise and approached a certain threshold, known as the critical hydraulic gradient, a distinct transition in flow behavior was noted. This point, referred to as the permeation transition point, marked the onset of internal instability. Before reaching this point, the flow velocity showed a decreasing trend with increasing gradient due to compaction effects. Once the critical gradient was exceeded, the flow velocity began

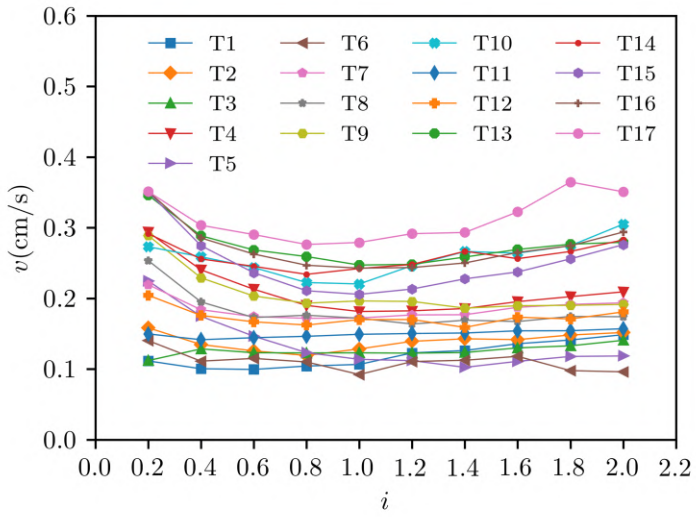

Figure II .4: Relationship between flow velocity and hydraulic gradient

to increase, and the relationship between velocity and gradient became either linear or nonlinear depending on factors such as the gradation coefficient and the initial porosity of the sample.

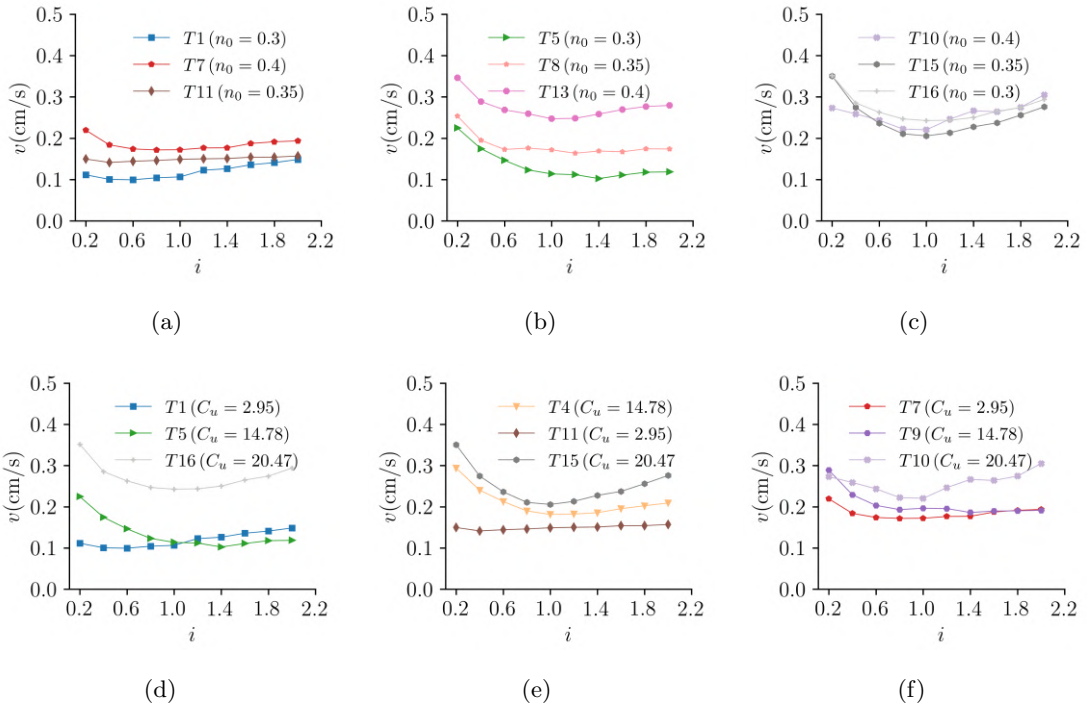

Figure II .5: The relationship between flow velocity and hydraulic gradient under different factors: (a) B1 gradation, (b) B2 gradation, (c) B1 gradation, (d) $n_0 = 0.3$, (e) $n_0 = 0.35$, (f) $n_0 = 0.4$

Comparing different porosity levels under the same gradation, the B1 mixture (Figure II .5(a)) exhibits an initial increase in permeability with increasing porosity. However, in group T7 ($n_0 = 0.4$), which has a higher porosity, more flow channels and particle activity space are available internally, resulting in a relatively smaller change in permeability compared to groups T1 ($n_0 = 0.3$) and T11 ($n_0 = 0.35$) before reaching the critical gradient. After surpassing the critical hydraulic gradient, all experimental groups transition from compaction to flow development stages. In lower porosity groups T1 and T11, flow velocities increase almost linearly with hydraulic gradient, while minor fluctuations are observed in group T7.

Under B2 gradation (Figure II .5(b)), permeability initially increases with increasing porosity, mainly due to the presence of 42.24% coarse particles ($d > 5$ mm) forming a load-bearing skeleton. The internal structure with stable skeleton formations containing

larger particles provides more space for fine particle movement with increasing porosity. However, due to better filling of fine particles, the initial variation in permeability is relatively small. After surpassing the critical gradient, flow velocities fluctuate as the internal structure of the B2 gradation continuously changes under hydraulic forces.

For B3 gradation (Figure II .5(c)), with 70.24% skeleton particles, the irregular packing of these coarse particles results in increased internal structural instability, causing fluctuating flow channels due to particle rearrangement. No clear correlation is observed between initial flow velocity and porosity. As shown in Figure II .5(a)–Figure II .5(c), increasing porosity at a constant gradation coefficient leads to greater fluctuations in flow velocity development. Permeability initially increases with porosity ($k = \frac{v}{i}$), and higher porosity samples exhibit relatively smaller changes in permeability before reaching the critical gradient compared to lower porosity samples.

Comparing experimental data results for different gradations under the same porosity level, at $n_0 = 0.3$ and $n_0 = 0.35$ (Figure II .5(d) and Figure II .5(e)), significant differences in flow velocity development are observed. Despite maintaining the same porosity level, differences in internal structure due to varying gradations are considered to be the primary factors affecting behavior. Gradations with higher skeleton particle content, such as B3 ($C_u = 20.47$), are generally expected to form larger and more connected pores internally, which may contribute to increased particle activity compared to B1 ($C_u = 2.95$) and B2 ($C_u = 14.78$). This could result in greater flow velocity fluctuations. At a porosity of 0.40 (Figure II .5(f)), gradations with higher skeleton particle content, such as B2 and B3, tend to develop larger, better-connected internal pores. However, at higher porosity levels, internal particle activity appears to increase, leading to more random particle motion and larger fluctuations in flow velocity. Figure II .5(d)-II .5(f) suggest that an increasing gradation coefficient under the same porosity level is associated with greater fluctuations in flow velocity development.

3.1.2 Relationship between incremental hydraulic gradient and mass migration rate

This relationship provides insight into the onset and progression of fine particle migration under controlled seepage conditions.

Based on the previously defined cumulative mass migration rate (m_e), the particle migration response of the sample under incremental hydraulic gradients was analyzed. The variation of m_e with increasing hydraulic gradient is shown in Figure II .6, illustrating how particle migration evolves as the hydraulic load is increased stepwise.

Overall, the analysis reveals that within the hydraulic gradient range of 0.2 to 2.0, group T10 exhibits the most pronounced variation in mass migration rate. The fluctuations in mass migration across the different groups correspond closely with the development of flow velocity. As the hydraulic gradient increases progressively, each group displays distinct peaks in cumulative mass migration rate, with the occurrence of these peaks aligning well with the onset of seepage transition points.

Comparing different experimental groups with the same gradation but different porosity levels, variations in cumulative mass migration rates are observed as the gradation coefficient and porosity change. For B1 gradation (Figure II .7(a)), in group T1 with a porosity of 0.30, the mass migration rate is the lowest, while there is little difference in cumulative rates between groups T11 and T7 with porosities of 0.35 and 0.40, respectively. This suggests that in gradations with smaller coefficients of uniformity, the denser internal structure is less susceptible to damage, and fine particles are less prone to migration. As porosity increases to a certain critical porosity, the loss of internal particles becomes less correlated with changes in porosity and more correlated with the proportion of erodible fine particles to the total mass.

For B2 gradation (Figure II .7(b)), comparing cumulative mass migration rates of three different porosity samples, group T8 with a porosity of 0.35 exhibits the lowest rate, while group T13 with a porosity of 0.40 develops more rapidly and reaches a higher cumulative value. This indicates that in gradations with moderate coefficients of uniformity, the

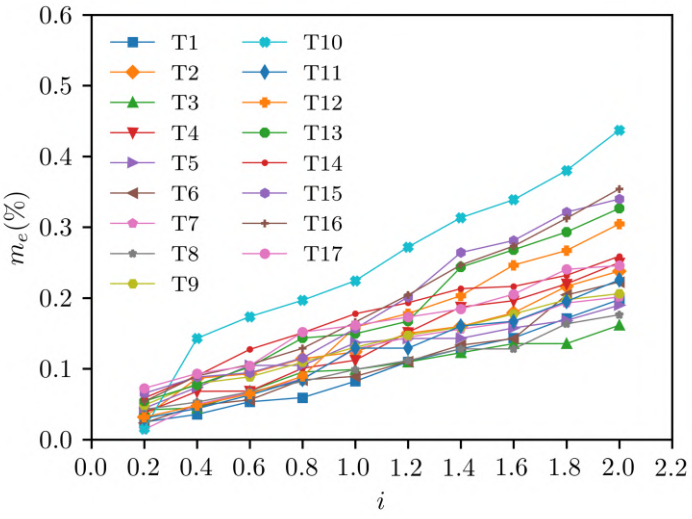

Figure II .6: Relationship between cumulative mass migration rate and hydraulic gradient

denser internal structure exhibits stronger stability, and fine particles are less susceptible to migration. As porosity increases, particle migration becomes more active, significantly higher than in groups with lower porosity.

For B3 gradation (Figure II .7(c)), comparing cumulative mass migration rates of three different porosity samples, group T15 with a porosity of 0.35 shows relatively lower migration in the early stages. However, after the hydraulic gradient increases to 1.2, it surpasses group T16 with a porosity of 0.30, though the difference is not significant. Group T10 with a porosity of 0.40 exhibits the fastest development and the highest cumulative mass migration rate. Comparing data from different gradations under the same porosity level (Figures II .7(d)–II .7(f)), it is evident that in gradations with larger coefficients of uniformity, the larger pore channels under hydraulic forces are more susceptible to particle migration, with initial porosity having less impact. As porosity increases to a certain critical value, the loss of internal particles becomes less correlated with porosity changes and more dependent on the proportion of mobilizable fine particles relative to the total mass.

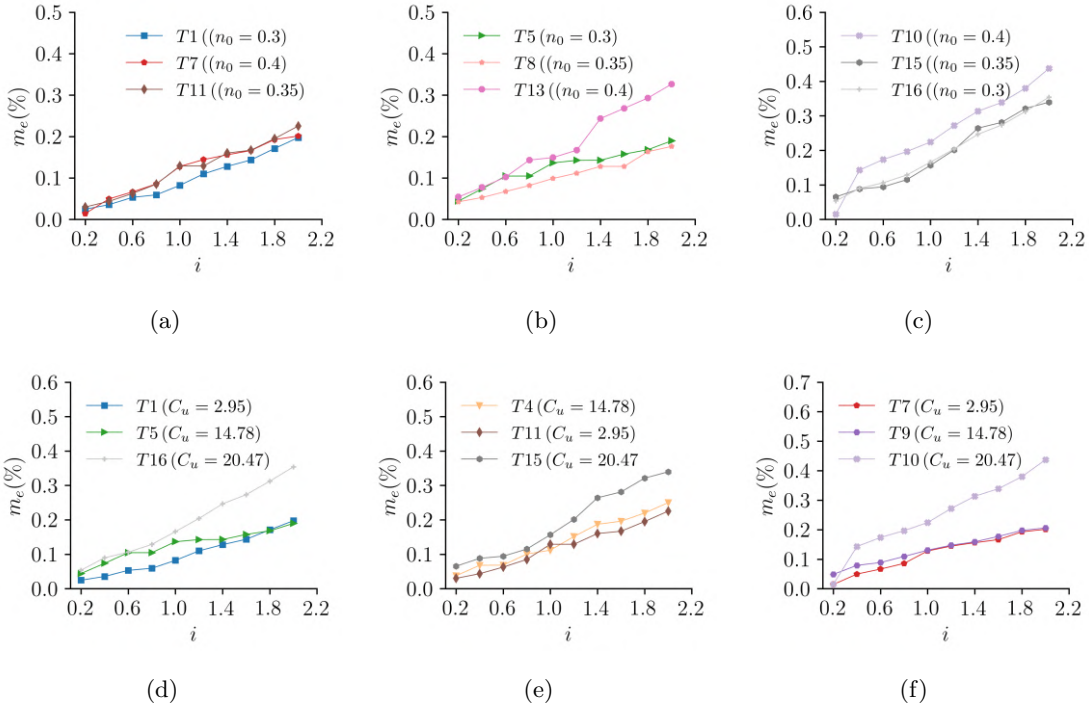

Figure II .7: Relationship between mass migration rate and hydraulic gradient under different factors: (a) B1 gradation, (b) B2 gradation, (c) B1 gradation, (d) $n_0 = 0.3$, (e) $n_0 = 0.35$, (f) $n_0 = 0.4$

3.2 Characteristics of fine particle movement

3.2.1 Image analysis

It is widely recognized that the properties of the microscopic structure vary with changes in soil particle composition (Kay and Angers, 2001). These changes in microstructure alter the contact relationships among particles, which in turn influence the soil's seepage behavior. In this study, digital imaging was employed to trace particle movement, providing supplementary evidence for analyzing particle migration patterns in soil mixtures.

Due to differences in sample parameters and external hydraulic environments, the extent of fine particle mobility within the specimens varied considerably. Based on qualitative observations from sequential microscopic images during testing, we propose a preliminary classification of particle movement behavior into three categories, according to the observed degree of activity: no apparent particle movement (I), individual particle motion along seepage channel (II), and large-scale particle motion and upper part densification (III). This qualitative classification is intended as a descriptive framework to interpret observed patterns, rather than a strict quantitative standard. The movement behavior in each group is summarized in Table II .4.

For motion state I, the sample shows minimal particle migration and only traces of fine particles are observed to migrate within the observation range. Water flow is visible throughout the observation, but fine particles exhibit no significant changes in their overall structure (Figure II .8).

In motion state II, some samples exhibit particle movement within the microscopic observation range under hydraulic action. However, the movement modes vary and include the following cases:

(1) In-situ oscillation and rotation (II-i). In-situ oscillation and rotation without net displacement. Trace particles show no obvious displacement but oscillate or rotate in situ with the water flow. Large bubbles formed by the coalescence of small bubbles are trapped in the pores and undergo continuous shape changes due to water flow impact. The trapped bubbles oscillate at the water-air interface (Figure II .9).

(2) Short-range particle migration localized along seepage channels (II-ii). Small-scale migration occurs along the seepage channel, converging in the main flow path and causing local clogging over short distances. For example, in Group T15, particle migration is observed throughout the specimen, with increasing activity from bottom to top. Fine particles converge from branch channels into the main channel, eventually forming localized

blockages (Figure II .10).

(3) Long-distance migration beyond observation range (II-iii). Relatively long-distance migration occurs along the seepage channel, with particle movement extending beyond the microscopic observation range. Group T17 exhibits such long-distance migration of fine particles, with observable loss along the seepage path. Accumulated migrating particles result in clogging, which may later be disrupted by increased hydraulic forces, leading to flushing of the blockage (Figure II .11).

In motion state III, large-scale particle motion and upper part densification. Trace fine particles are observed to resettle along zones under hydraulic action, leading to seepage-induced densification. In Group T10, a large number of particles in the upper and middle portions migrate with the water flow and are lost along the seepage paths (Figure II .12). The movement distance exceeds the field of microscopic observation, and some fine particles aggregate and deposit in tortuous, non-through pores within the visible area.

It is emphasized that this classification is based on visual interpretation under experimental conditions, and further research is needed to develop quantitative criteria for particle mobility characterization.

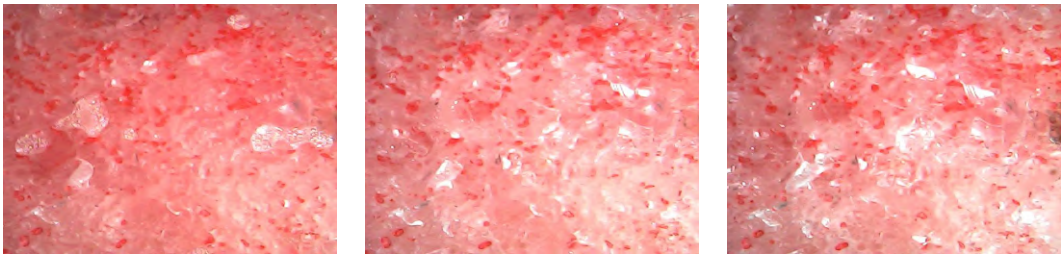

(a) (b) (c)

Figure II .8: Motion state I: No apparent particle motion (T1): (a) 5 min, $i = 0.20$; (b) 65 min, $i = 0.80$; (c) 125 min, $i = 1.80$

Differences in sample parameters lead to differences in phenomena. With the increase in gradation unevenness and sample porosity, the instability of internal particles gradually increases. No single index among the factors exhibits a clear main control feature. Under the comprehensive effect of various factors, larger pores can form within the sample skeleton particles, resulting in faster internal flow velocity, and the fine particles become more unstable and prone to damage. There are differences in zone movement within the same sample. Except for group T4, the instability of internal fine particles in the other groups follows the phenomenon of upper > middle > lower. The phenomenon in group T4 is due to the microscopic observation point being located on the main seepage channel, where

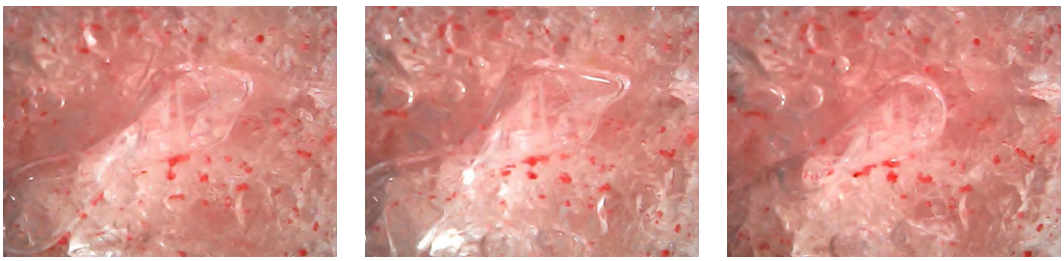

(a) (b) (c)

Figure II .9: Motion state II, II-i: In-situ oscillation and rotation (T13); (a) 5 min, i = 0.20; (b) 65 min, i = 0.80; (c) 125 min, i = 1.80

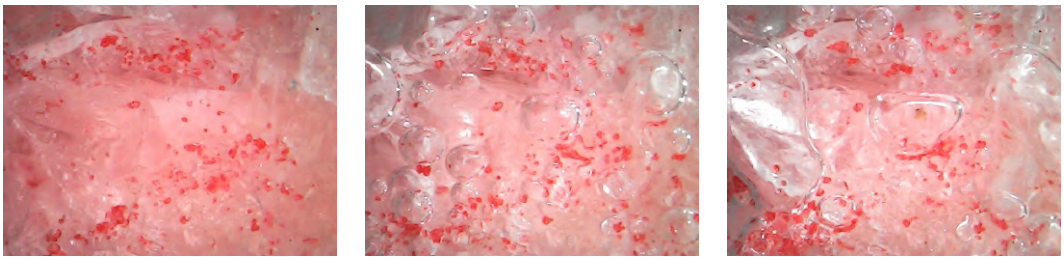

(a) (b) (c)

Figure II .10: Motion state II, II-ii: Short-distance migration and upper part clogging (T15); (a) 5 min, i = 0.20; (b) 65 min, i = 0.80; (c) 125 min, i = 1.80

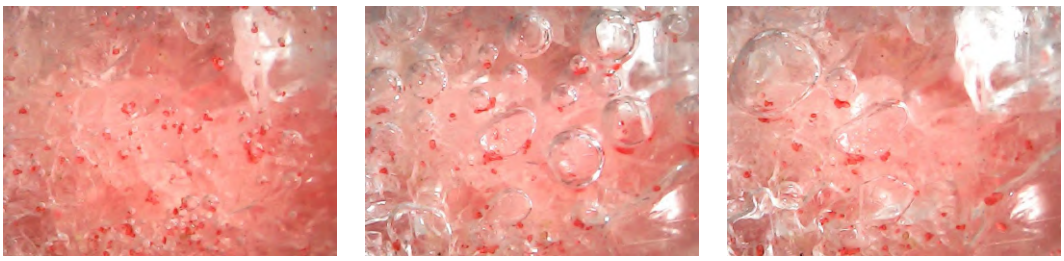

(a) (b) (c)

Figure II .11: Motion state II, II-iii: Long-distance migration beyond observation range (T17); (a) 5 min, i = 0.20; (b) 65 min, i = 0.80; (c) 125 min, i = 1.80

the flow velocity is relatively fast, and the hydraulic shear force is stronger. Additionally, comparing the initial and final images of each hydraulic gradient, it can be observed that in the range of i = 0.6-1.0, the greatest changes in particle migration of the red trace particles occur, indicating significant deformation and damage to the framework formed

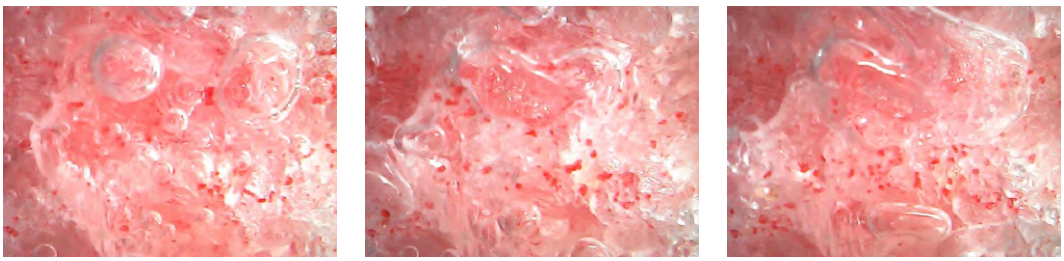

(a) (b) (c)

Figure II .12: Motion state III: Large-scale particle motion and upper part densification (T10): (a) 5 min, $i = 0.20$; (b) 65 min, $i = 0.80$; (c) 125 min, $i = 1.80$

by coarse particles.

In fact, during infiltration experiments, the liquid phase within aggregated granular materials continuously displaces the gas phase within the pores. During this process, some gas is expelled from the soil mass due to compression, while another portion becomes trapped by the water phase within the internal pores, resulting in localized decreases in permeability. The solid phase can be divided into skeleton particles and mobile particles. During the seepage process, skeleton particles do not undergo movement due to seepage forces; instead, they support each other and interlock to form pathways for the mixed fluid to pass through. Some mobile particles, under hydraulic action, migrate with the water and may settle in specific pore throats, adhering to the internal surfaces and temporarily becoming part of the granular skeleton. When hydraulic conditions change, these particles can be remobilized, initiating further particle migration

3.2.2 Post-experiment particle size characteristics in different regions

After the experiment, the samples were sieved into upper, middle, and lower layers to obtain the particle size distribution curves and related particle size parameters for each layer, studying the variation in particle size distribution caused by particle loss in different regions. The groups with the same experimental parameters were merged and summarized for uniformity coefficients and curvature coefficients (Figure II .13).

It can be observed that for $C_u = 2.95$ groups, there was little difference in the uniformity coefficient among the upper, middle, and lower layers before and after the experiment. For $C_u = 14.78$ groups, two situations were observed: the non-uniformity coefficient decreased layer by layer from top to bottom (with possibly little difference between the middle and lower layers), as seen in T2, T4, T5, T6, and T13, while some groups showed no clear

Table II .4: Modified table for particle motion classification

Motion Status		Upper	Middle	Lower	Parameters
No apparent particle motion (I)		T1	T1	T1	$C_u = 2.95, n = 0.30$
		T3	T3	T3	$C_u = 2.95, n = 0.35$
		T7	T7	T7	$C_u = 2.95, n = 0.40$
		T5	T5	T5	$C_u = 14.78, n = 0.30$
		T6	T6	T6	$C_u = 14.78, n = 0.30$
		T2	T2	T2	$C_u = 14.78, n = 0.35$
				T8	$C_u = 14.78, n = 0.35$
			T9	T9	$C_u = 14.78, n = 0.40$
			T13	T13	$C_u = 14.78, n = 0.40$
Individual particle motion along seepage channel (II)	In-situ oscillation, rotation	T9			$C_u = 14.78, n = 0.40$
		T13			$C_u = 14.78, n = 0.40$
		T12			$C_u = 20.47, n = 0.35$
		T16			$C_u = 20.47, n = 0.30$
	Short-distance migration	T11	T11	T11	$C_u = 2.95, n = 0.35$
		T4	T4		$C_u = 14.78, n = 0.35$
		T8	T8		$C_u = 14.78, n = 0.35$
			T12	T12	$C_u = 20.47, n = 0.35$
		T15	T15	T15	$C_u = 20.47, n = 0.35$
			T16	T16	$C_u = 20.47, n = 0.30$
	Migration beyond observation range	T14	T14	T14	$C_u = 14.78, n = 0.35$
		T17	T17	T17	$C_u = 14.78, n = 0.35$
		T10			$C_u = 20.47, n = 0.40$
Large-scale particle motion (III)				T4	$C_u = 14.78, n = 0.35$
			T10	T10	$C_u = 20.47, n = 0.40$

trend in the change of non-uniformity coefficient, such as T8, T9, T14, and T17. For $C_u =$ 20.47 groups, there was a significant change in non-uniformity coefficient among the three layers compared to before the experiment, with irregular changes.

The difference in non-uniformity coefficient among layers was attributed to the migration of fine particles caused by hydraulic drag during the experiment. Based on the premise of fine particle migration, it can be assumed that when the sample non-uniformity is low, the amount of fine particle migration is small, resulting in minor changes in internal non-uniformity. Conversely, when the sample non-uniformity is high, there is more space for particle movement inside, and long-distance migration is more likely to occur, leading to differences in particle size distribution along the direction of water flow.

The variation in non-uniformity reflects the reorganization of particle size distribution inside the sample before and after the experiment. Directly conducting layered sieving and statistical extraction of parameters for samples after hydraulic particle migration neglects the influence of the collected lost particles on the total mass of the material and the proportion of particles of each size. Limited by the sieve pore size at the bottom

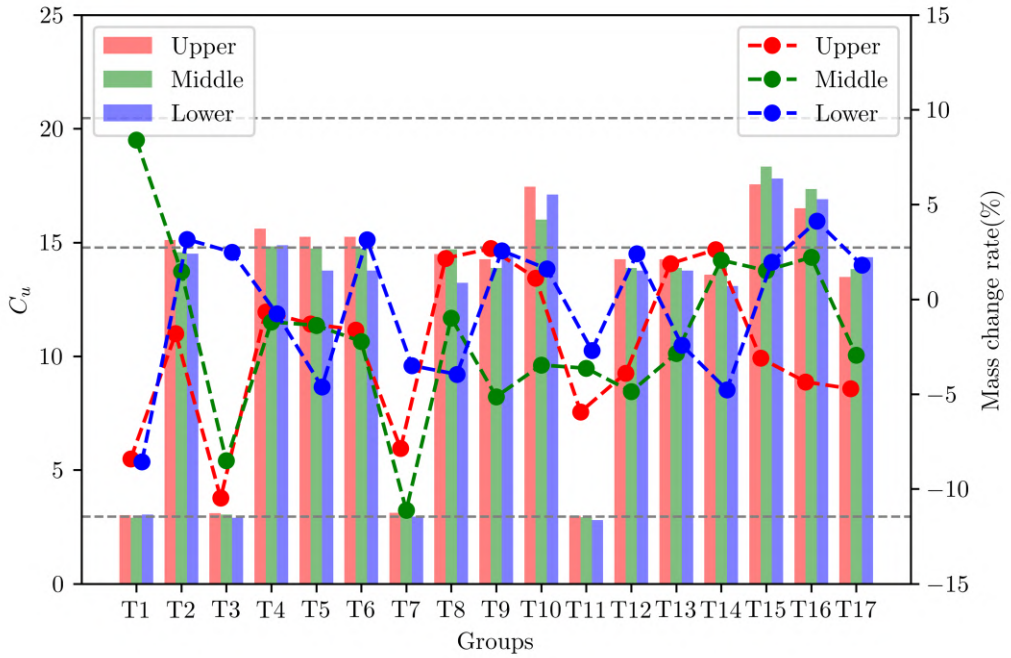

Figure II .13: Non-uniformity coefficients and mass change rates of upper, middle, and lower layers after experiments for each group: The bar chart represents the non-uniformity coefficients at the three layer positions, while the dotted line chart represents the mass change rates

of the testing instrument (2mm), particles larger than 2mm cannot be lost. Therefore, the proportion of particles larger than 2mm remains essentially unchanged. The mass obtained from sieving particles larger than 2mm can be used to calculate the total mass of each layer, and the actual proportion of particles of each size can be obtained based on the original total mass.

Figure II .13 presents the results of the reverse calculation of mass proportions, from which the mass change rate of each layer can be derived. All test groups exhibited an overall mass loss, with distinct variations in mass changes across different layers. A common feature among the groups is the mass loss observed in the upper layers. The differences mainly lie in the evolution of mass in the lower layers: in some cases, mass accumulation occurred, while in others, the mass input was less than the output, resulting in a net mass loss.

The variation in layer mass is related to the imbalance in mass input and output among layers, fundamentally determined by the ease of movement of fine particles within the material and the size of permeable pores. When fine particles move easily but have limited migration distances due to pore characteristics, they only affect local permeability. However, if there are permeable channels available for long-distance migration of fine particles, the fine particle content in each layer will decrease, resulting in a total mass loss in the specimen. It is worth noting that the calculated mass loss differs from the mass of lost particles collected through sedimentation, as hydraulic particle migration carries away a large amount of suspended fine particles that cannot be collected in sedimentation tanks.

3.3 Filtration behavior patterns

Previous analyses have indicated that the filtration behavior of soil is closely related to hydraulic action, porosity, and the coefficient of uniformity. When the hydraulic gradient changes, the fine particles in the region remain generally stable under normal hydraulic gradient conditions. However, when the hydraulic gradient is relatively low, the migration of fine particles within the pore structure is limited, and the porosity tends to gradually decrease due to particle rearrangement and compaction in the later stages of seepage. The velocity variation curve shows that an increase in porosity is generally accompanied by an increase in flow velocity. This elevated flow velocity enhances the hydrodynamic forces acting on fine particles, promoting their migration and removal. As a result, the increase in flow velocity and fine particle migration reinforce each other, exhibiting a self-reinforcing process. When the hydraulic gradient is very high, as the porosity in the region continues

to increase, the soil structure becomes more and more loose, and the average contact force between particles is smaller compared to conditions with a lower hydraulic gradient. This indicates that the region's resistance to particle migration is weaker at this time. Conversely, when the hydraulic gradient is lower, more fine particles become clogged in the region, the particle arrangement becomes tighter, and the average contact force between particles increases, resulting in a more stable structure. The possible relationship between the mechanical behavior of local particles and hydraulic characteristics is shown in Figure II .14. It can be inferred that when the phenomenon of fine particle filtration in individual regions transitions to a collective phenomenon under critical conditions, the weakening of local resistance will ultimately affect the overall seepage stability of the sample.

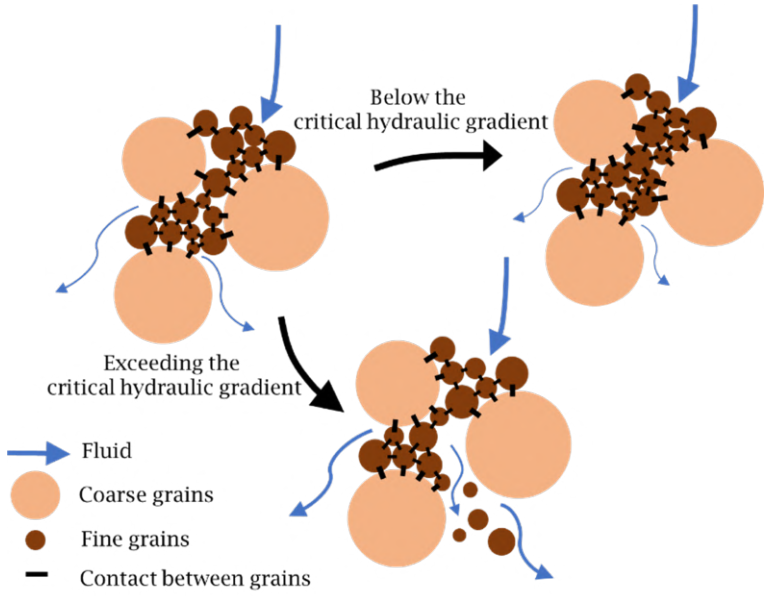

Figure II .14: Filtration behavior patterns influenced by hydraulic gradient

When the soil's coefficient of uniformity varies, there exists a threshold for the impact of the coefficient of uniformity on soil filtration behavior. When the coefficient of uniformity exceeds this threshold, the soil structure becomes unstable, and it is prone to damage under hydraulic action, causing fine particles to undergo filtration (Figure II .15). Once this process reaches a certain extent, it can even affect the overall structure of coarse particles. Conversely, when the coefficient of uniformity is below this threshold, the interaction forces between particles are stronger, leading to a denser accumulation that is less susceptible to disruption by the hydraulic gradient.

Regarding porosity, there also exists a threshold for its impact on soil filtration behavior. When the porosity is below this threshold, the voids between coarse particles are

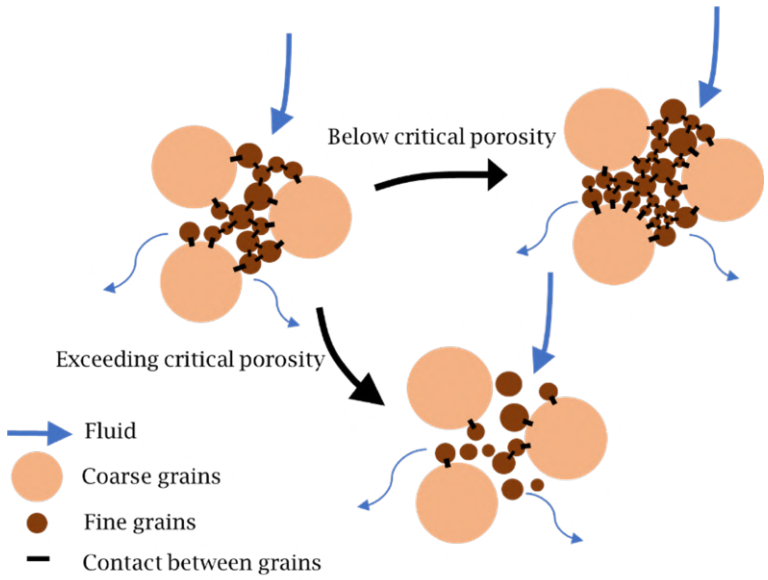

Figure II .15: Filtration behavior patterns influenced by the coefficient of uniformity

extensively filled with fine particles, resulting in tight connections between particles and a stable skeletal structure (Figure II .16). This primarily manifests as overall deposition. However, when the porosity exceeds this threshold, fine particles undergo filtration under the action of the hydraulic gradient, further increasing the porosity and compromising the structural integrity, leading to an unstable skeleton.

3.4 Internal stability

Internal stability describes the soil's ability to resist particle migration and reflects its resistance to structural degradation under seepage forces. Therefore, the extent of hydraulically induced instability is an important indicator for evaluating internal stability. Within the soil mass, fine particles can exhibit different transport phenomena during self-filtration. Flowing soil, piping, contact particle movement, and contact loss represent different characteristics of seepage-induced particle migration.

While numerous approaches exist for assessing internal stability, this study conducted a comparative evaluation using several representative methods. The results are presented in Figure II .17. It is evident that different criteria yield varying judgments on the internal stability of granular materials with different parameters. In some cases, they even produce completely contradictory results. For instance, the Burenkova method tends to be conservative, classifying all groups as unstable. In contrast, the Wan & Well method is more aggressive, classifying all groups as stable. The judgment results of these criteria

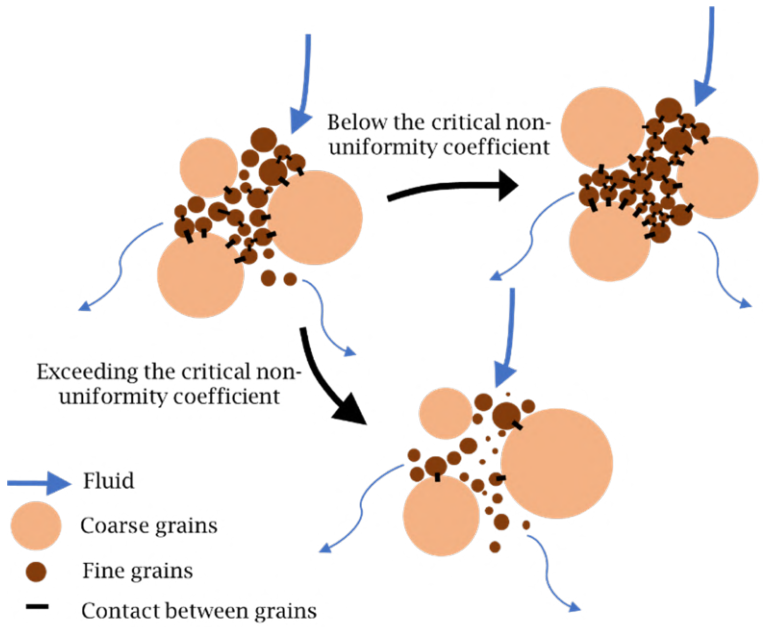

Figure II .16: Filtration behavior patterns influenced by porosity

sometimes deviate from actual observations. The Kezdi criterion classified groups with $C_u = 2.95$ and $C_u = 14.78$ as stable, yet in actual tests, fine particles were observed to migrate. The Andrianatrehina method only classified the T3 group with $C_u = 2.95$ and $n_0 = 0.35$ as unstable. However, in actual tests, the T4 group exhibited the largest scale of fine particle movement, while the T3 group showed no significant particle movement under microscopic observation. This discrepancy could be due to method-specific biases and particle segregation during the compaction process.

Considering the results of multiple criteria, the Istonima criterion appears to be relatively accurate. The deviations in judgment by various criteria for the fused quartz sand accumulation material are due to the insufficient use of judgment criteria in specific internal stability criteria and the incomplete consideration of controlling factors. Most methods judge the medium using direct or indirect indicators. Direct methods assess stability based on the amount of eroded fine particles that flow out, while indirect methods judge based on changes in seepage characteristics.

It is important to note that the movement or even long-distance migration of internal fine particles under hydraulic action does not necessarily mean they can flow out of the sample. The internal structure is complex, with small pore throats and high tortuosity, which may result in the filtration effect of fine particles. This introduces bias when using mass migration amounts amounts for judgment. Seepage characteristics can indirectly

Table II .5: Soil internal stability criteria control variables and indexes

Criterion	Control variable	Evaluation indicator
Istomina (1957)	$C_u = d_{60}/d_{10}$	$C_u \leq 10$ (S) $10 \leq C_u \leq 20$ (T) $C_u \geq 20$ (U)
Kezdi (1969)	$(d_{15c}/d_{85f})_{\max}$	$(d_{15c}/d_{85f})_{\max} \leq 4$ (S) $(d_{15c}/d_{85f})_{\max} > 4$ (U)
Burenkova (1993)	$h' = d_{90}/d_{60}$ & $h'' = d_{90}/d_{15}$	$0.76\log(h'') + 1 < h' < 1.86\log(h'') + 1$
Wan and Fell (2008)	$h' = d_{90}/d_{60}$ & $h'' = d_{20}/d_{15}$	$30/\log(d_{90}/d_{60}) > 110$ & $15/\log(d_{20}/d_{15}) < 15$ (S) $(30/\log(d_{90}/d_{60}) < 80)$ & $(30/\log(d_{90}/d_{60}) < 80 \mid 15/\log(d_{20}/d_{15}) > 22)$ (U) Other (T)
Andrianatrehina et al. (2016)	$\Delta P_{\max}$	$\Delta P_{\max} < 5\%$ (S) $\Delta P_{\max} \geq 5\%$ (U)

Notes: (1) d_x: The particle size corresponding to the cumulative mass fraction x of particles smaller than a certain size within the coarse particle group. (2) $(d_{15c}/d_{85f})_{\max}$: The maximum filtration ratio corresponding to different separation particle sizes. (3) $h' = d_{90}/d_{60}$: Represents the degree of non-uniformity in the coarse particle portion. (4) d_{90}/d_{15}: Represents the degree of non-uniformity in the fine particle portion. (5) $\Delta P_{\max}$: The maximum value of the gradation difference between the upper and lower layers. (6) S: Stable, T: Transitional, U: Unstable.

reflect the internal condition of particle accumulations, but the quantitative indicators related to internal stability need further clarification.

To improve the judgment of stability by considering the gradation characteristics of accumulated granular materials, it is helpful to also incorporate porosity into the evaluation. This can be done by using the optimal fine particle content when the pores within the particle skeleton are filled, aiding in the determination of seepage failure forms (GB50487-2008, 2008):

$$P_{cp} = \frac{0.30 + 3n^2 - n}{1 - n} \tag{II .3}$$

where P_{cp} is the optimal fine particle content, and n is the porosity.

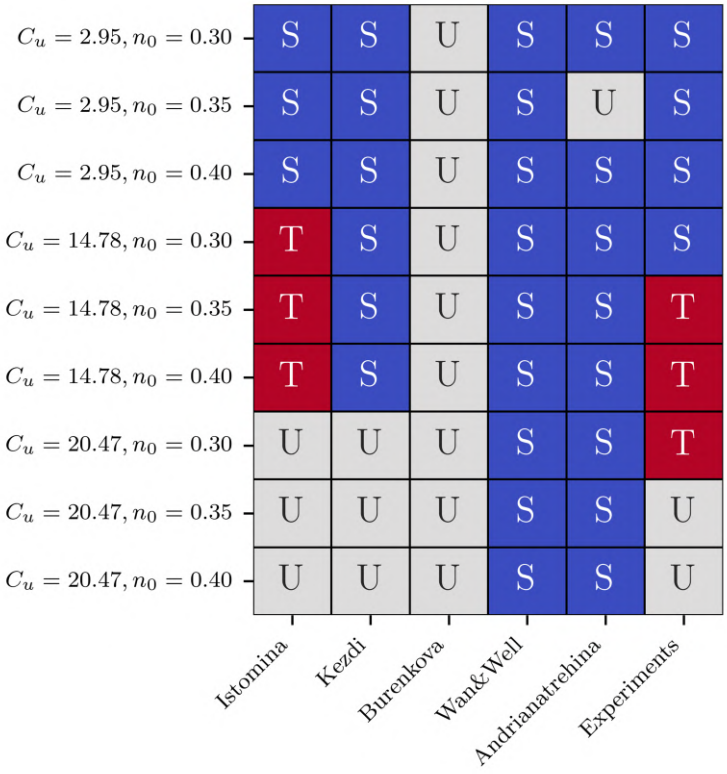

Figure II .17: Evaluation results using various criteria.(S for stable, T for transitional, U for unstable)

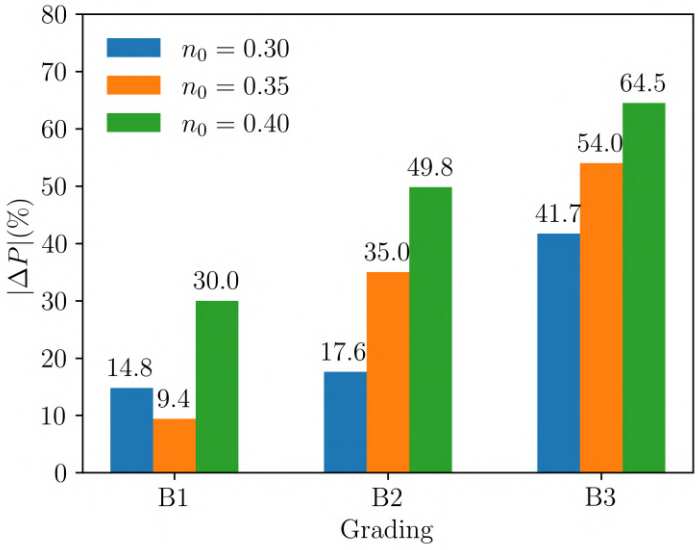

Figure II .18: $|\Delta P|$ under different gradation and porosity conditions

The optimal fine particle content P_{cp} was calculated for different porosities n, and compared with the actual fine particle content P of the sample. The value of P was determined using the post-migration particle size distribution, based on the coarse–fine boundary defined as $d' = \sqrt{d_{10} \cdot d_{70}}$. The percentage of particles smaller than this threshold was considered as the fine particle content P. The absolute difference between the two, $|\Delta P| = |P - P_{\mathrm{cp}}|$, was used to evaluate the deviation under various gradation and porosity conditions (Figure II .18).

It was found that $|\Delta P|$ is positively correlated with both the coefficient of uniformity and porosity. Among all the tested combinations, the group with $C_u = 20.47$ and $n = 0.40$ showed the greatest difference. Theoretically, this condition allows for the largest space for fine particle migration, indicating the lowest internal stability, which was also confirmed by experimental observations.

Based on this analysis, considering both the porosity n and the coefficient of uniformity, along with the results of the cylindrical infiltration tests for different porosities and coefficients of uniformity, a new method for stability judgment was proposed. This method takes into account both the porosity n and the coefficient of uniformity (Table II .6).

Table II .6: Modified Istomina Criterion considering n and C_u

Control Variable	Evaluation Indicator
	$\lvert\Delta P\rvert \geq 50\% \mid C_u \geq 20$
$n\&C_u$	$30\% < \lvert\Delta P\rvert < 50\% \ \& \ C_u < 20$
	$\lvert\Delta P\rvert < 30\% \ \& \ C_u < 20$

4 Conclusions

This chapter introduces the experimental investigation into the sensitivity of cumulative mass migration rates to various factors, such as hydraulic gradient, coefficient of uniformity, and porosity. Through experiments conducted with a self-developed rigid cylindrical seepage visualization device on transparent fused quartz sand, the study reveals the relationships between these factors and the internal instability of the sample under seepage conditions.

The results demonstrate that the hydraulic gradient has the most significant influence on the mass migration rate, followed by the coefficient of uniformity and porosity. These findings emphasize the positive correlation between the uniformity and porosity of the

granular media and the stability of fine particle movement. The greater the uniformity and porosity, the more pronounced the movement of fine particles, leading to higher cumulative mass migration rates. Furthermore, the study highlights the non-linear development of flow velocity during the downward seepage process, with a critical transition point marking the shift from seepage compaction to particle migration.

The chapter also identifies five distinct characteristic states in the movement of fine particles, with stratification occurring due to the varying ease of particle migration within the material. These characteristic states are observed based on the visual and experimental analysis of mass migration behavior under seepage flow:

1. No apparent particle motion (Type I): Fine particles remain stationary, and the soil structure remains stable under hydraulic loading.

2. Individual particle motion along seepage channel (Type II-i): Fine particles show slight vibration or rotation without significant displacement, often accompanied by bubble formation and movement.

3. In-situ oscillation, rotation (Type II-ii): Fine particles migrate over short distances along seepage paths, gradually accumulating and causing local clogging without major structural change.

4. Migration beyond observation range (Type II-iii): Fine particles travel longer distances, leading to accumulation and eventual flushing of blockage as hydraulic forces increase.

5. Large-scale particle motion (Type III): Disruption of the particle skeleton occurs, with significant particle loss and local compaction under flow.

The study concludes that the Istonima criterion, when incorporating both gradation parameters and porosity, provides a relatively accurate method for predicting internal stability. It effectively accounts for the combined influence of multiple factors on granular instability.

Chapter III

Numerical Approach Dynamic Fluid Meshs: Application to Internal Erosion

1 Introduction

To better visualize the dynamic process of fine particle migration in soils and capture the mechanisms of water-soil interactions, this study introduces an enhanced numerical method: the coupling of Dynamic Fluid Mesh (DFM) and Discrete Element Method (DEM). Building on the traditional Pore Network Model and Discrete Element Method (PNM-DEM), this approach addresses limitations in simulating complex particle movements and dynamic fluid behaviors. By dynamically updating fluid paths and pressure fields, the DFM method effectively handles systems with high fine particle content and significant porosity changes. Treating the fluid as a compressible medium and incorporating fluid state equations further allows the model to explore the interplay between temperature, density, and pressure, advancing the study of multi-physics coupling.

This chapter establishes the governing equations for hydraulic interactions and material exchange and validates the DFM-DEM approach through one-dimensional simulations of seepage behavior. The mass migration rate and pore structure evolution at a fine particle content of 5% are analyzed, revealing the fundamental mechanisms of suffusion. Additionally, the potential for grid changes under different particle filling states is discussed to optimize the fluid–solid coupling process. A comparison with static fluid grids highlights the advantages of DFM-DEM in capturing the dynamic behavior of fine particle migration, providing a reliable foundation for further studies and engineering applications.

2 Coupling of DFM-DEM

Figure III .1 presents the workflow of the DFM-DEM coupling model utilized in this study. Initially, a DEM model is established to distinguish between coarse and fine particles. A tetrahedral grid is then constructed by using the Delaunay algorithm (Persson and Strang, 2004) in MATLAB, based on the coarse particles distribution. Subsequently, the porosity and permeability of each fluid cell are computed considering the positions and sizes of all particles. Darcy's law is employed to calculate the fluid velocity field. Assuming that the fluid is compressible, and the fluid pressure is obtained by solving the fluid state equation. Then, the fluid-particle interaction forces are applied to each particle, and the process is iteratively repeated. The fluid grid, porosity, permeability, flow forces, pore density, and pore pressure are updated at predetermined time intervals. The program terminates when the total number of steps reaches the specified limit. The following subsections provide a detailed description for each step.

2.1 Mechanical model in DEM

In a Discrete Element Method (DEM), the relationship between force and displacement is achieved through tangential and normal springs (III .2(a)). In this paper, the force-displacement relationship for two elastic spheres is considered using a linear contact model with the cut-off limits. The normal force ($\boldsymbol{F}_n$) and relative normal displacement (X_n) between the two contacted particles considered can be simulated using normal springs

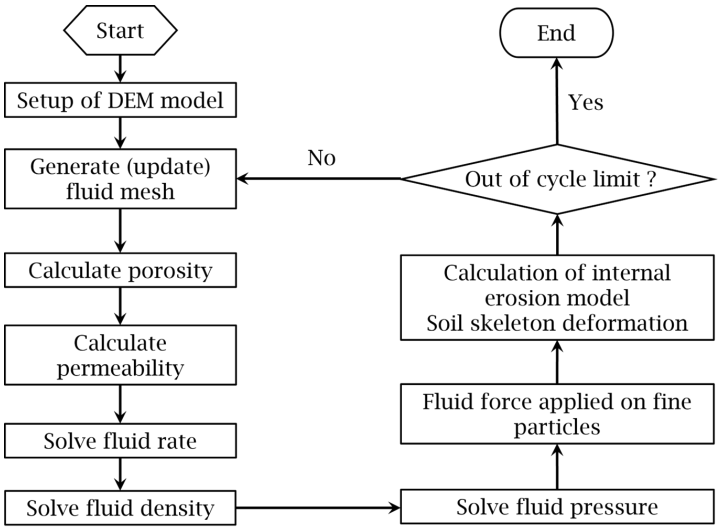

Figure III .1: The flowchart of the proposed numerical approach

between the particles:

$$\boldsymbol{F}_n = \begin{cases} K_n X_n & X_n < X_b \\ 0 & X_n > X_b \end{cases} \tag{III .1}$$

here, the X_n is the relative displacement between the two connected particles, as shown in Figure III .2(a). It is defined as positive in traction; and negative, that means the supposition part of the two connected particles, is in compression. And the X_b is defined as the cut-off for the traction, it is the function of the strength in traction of material, the stiffness of the springs and the radius of soil particle. The K_n is the normal stiffness of the normal spring between the two connected particles, as shown in Figure III .2(a).

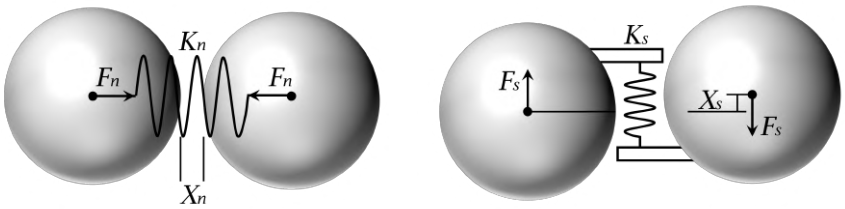

(a) (b)

Figure III .2: Mechanical relationships in the linear spring contact model

Similarly, the shear force ($\boldsymbol{F}_s$) and shear displacement (X_s) of the tangential spring between the same connected particles pair, as shown in III .3(b), have the relation as:

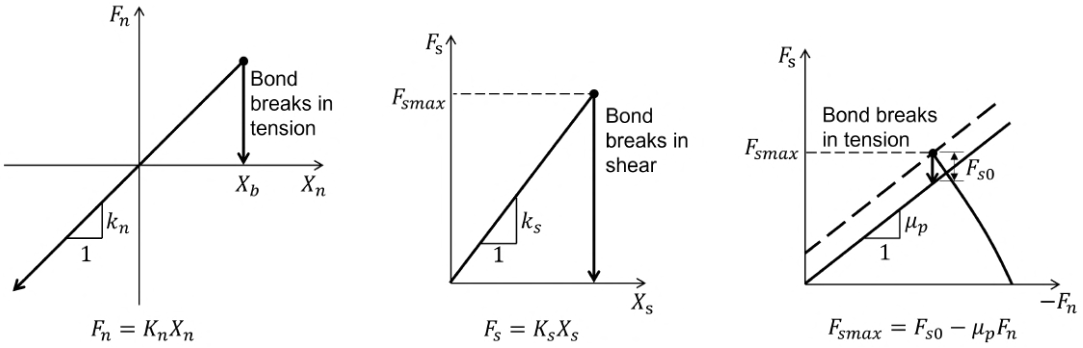

(a) (b) (c)

Figure III .3: Force-displacement law for the linear component of the linear-based models: (a) normal force versus relative normal displacement, (b) shear force versus relative shear displacement, and (c) slip envelope

$$\boldsymbol{F}_s = K_s X_s \tag{III .2}$$

here, K_s is the stiffness of the tangential spring.

The tangential spring also has a failure criterion, which is based on the Mohr-Coulomb criterion (Place and Mora, 1999), as:

$$F_{smax} = F_{s0} - \mu_p F_n \tag{III .3}$$

where F_{smax} is the maximum shear force, F_{s0} is the initial shear strength due to the cohesion between the connected particles, and μ_p is the coefficient of friction between them.

Furthermore, it is worth mentioned that the dynamic integration process is adopted in our numerical approach (DEM), and the energy dissipation processes is essential for reproducing the real scenarios in the soil. Energy dissipation is typically guarantee by damping and/or viscosity. Liu et al. (2013) defined the global damping ($\boldsymbol{F}_v$) as:

$$\boldsymbol{F}_v = \eta \boldsymbol{x'} \tag{III .4}$$

where $\boldsymbol{x'}$ is the current velocity of the element and η is the viscosity.

Thus, when considering the deformation of a discrete element assembly under force equilibrium, it can be generalized as a spring-mass system, described by the equation as following:

$$m\boldsymbol{x''} + \eta \boldsymbol{x'} + k\boldsymbol{x} = 0 \tag{III .5}$$

where $\boldsymbol{x''}$ is the current acceleration of the particle element, $\boldsymbol{x}$ is the current displacement of the particle element, m is the mass of current particle, k is the global stiffness of all the connected spring of the particle considered.

2.2 DFM and fluid calculations

In this study, the fluid calculations, namely the permeability and fluid velocity, are based on the Dynamic Fluid Mesh (DFM). The DFM was constructed based on the positions of coarse particles, without considering the influence of coarse particle mass on the mesh centroid, as shown in III .4(a). Percolation paths connected two tetrahedral mesh centroids, with their length being the distance between the two centroids. In III .4(b), material exchange within each fluid mesh took place through every face of the tetrahedra.

However, these material exchange faces were irregular triangles, with areas overlapping coarse particles that hindered fluid exchange.

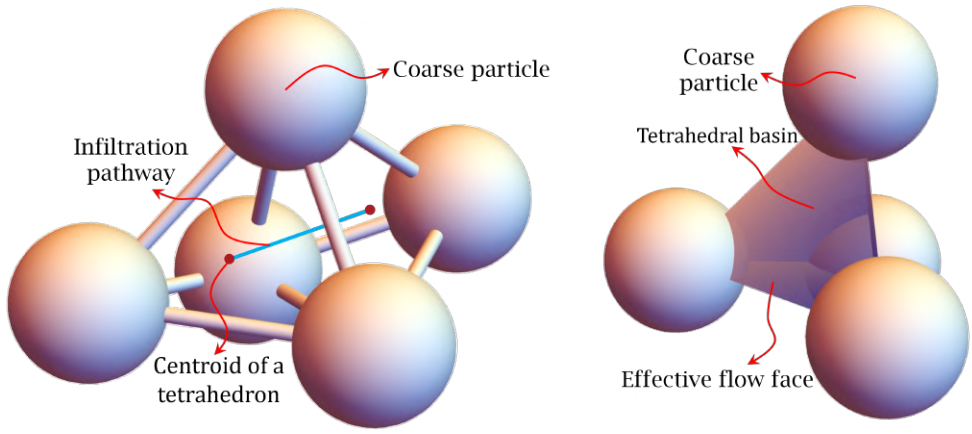

(a) (b)

Figure III .4: Illustration of material transport in the fluid grid

In reality, the effective volume and effective permeable surface of the permeation domain take into account both the volume of coarse and fine particles. To obtain the porosity of each tetrahedron, the combined volumes of coarse and fine particles within each tetrahedron are calculated separately. For coarse particles, the volume of tetrahedra embedded within the particles is first calculated. Then, a volume correction factor is applied to the embedded tetrahedra to add a small additional volume near the spherical boundaries. Furthermore, to provide geometric continuity and avoid spurious boundary effects, a virtual particle is inserted at the tetrahedral nodes located on the outer boundary (III .5). Subsequently, the volume of coarse particles within the tetrahedra is calculated using the same method, with a coefficient slightly larger than that applied to prevent the formation of large flow channels at the boundary before. This represents the boundary of the rubber membrane in the experiment (Chang and Zhang, 2011). For the fine particles, the total volume is recorded within the tetrahedron where the particle's center of mass is located. The porosity (ϕ) is calculated as follows:

$$\phi = \frac{V_{tet} - V_{coarse} - V_{fine}}{V_{tet}} \tag{III .6}$$

where ϕ is the porosity calculated, V_{tet} is the volume of the polyhedral mesh, V_{coarse} is the volume of the coarse particles embedded in current tetrahedron, and V_{fine} is the volume of the fine particles included in current tetrahedron.

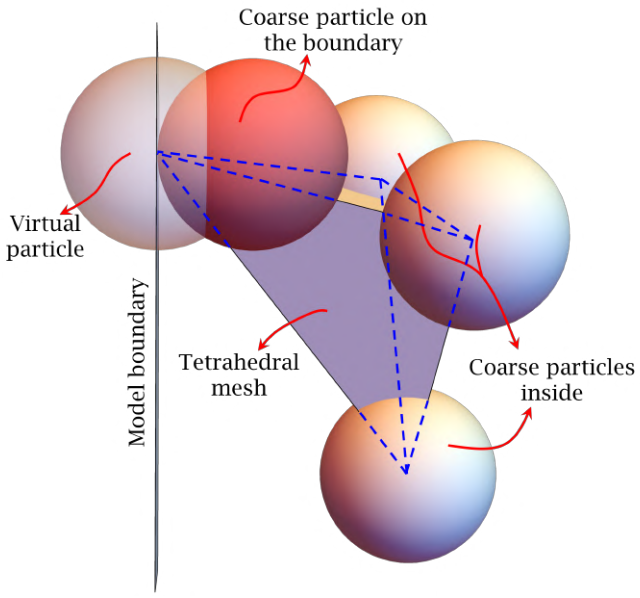

Figure III .5: Insertion of a virtual particle at the boundary for computation purposes

The permeability is obtained using the Kozeny-Carman equation (Carman, 1956; Kozeny, 1927):

$$K = \frac{\phi^3}{c(1-\phi)^2 S^2} \tag{III .7}$$

where K is the matrix permeability, c is the Kozeny-Carman constant (dimensionless), and S is the specific surface area of the solid phase.

The Kozeny-Carman equation has been reformulated to incorporate more geometric information based on the average particle diameter d_m^2 (Sullivan and Hertel, 1942). For spherical grains, the two parameters $d_m = \frac{6}{S}$ and $c = 5$ are given, and the equation becomes:

$$K = \frac{d_m^2 \phi^3}{180(1-\phi)^2} \tag{III .8}$$

where d_m is the average diameter of the fine particle.

The flow with low Reynolds number in porous media is described by Darcy's law:

$$\boldsymbol{v} = -\frac{K}{\mu\phi}\nabla p \tag{III .9}$$

where $\boldsymbol{v}$ is the fluid velocity, p is the fluid pressure, and μ is the dynamic viscosity of the fluid.

2.3 Interaction forces

It is evident that the case we considered is fully hydro-mechanical coupling. After the application of fluid, the particles experience forces exerted by the fluid, which influence their movement. For coarse particles, the fluid primarily acts on them through pressure, and the force exerted by the fluid on the coarse particles is given by:

$$\boldsymbol{F}_f = \sum_i p_i S_i \tag{III .10}$$

where p_i is the pore water pressure and S_i is the surface area of the particles within the i-th fluid mesh.

As for fine particles, they are more influenced by the fluid, and the interaction between the fluid and the particles is primarily composed of drag force and buoyancy. The drag force is calculated based on the following formula (Di Felice, 1994):

$$\boldsymbol{F}_d = \boldsymbol{F}_0 \phi^{-\chi} \tag{III .11}$$

where $\boldsymbol{F}_d$ is the drag force exerted by the flowed fluid on the particles, $\boldsymbol{F}_0$ is the drag force on an individual particle, ϕ is the porosity as given in Eq.(III .6), and χ is the Di Felice correction factor for porosity, which is dimensionless.

The drag force on an individual particle can be calculated using the following formula:

$$\boldsymbol{F}_0 = \frac{1}{2} C_d \rho_f \pi r^2 \left|\boldsymbol{u} - \boldsymbol{v}\right| (\boldsymbol{u} - \boldsymbol{v}) \tag{III .12}$$

where C_d is the drag coefficient (dimensionless), ρ_f is the fluid density in kilograms per cubic meter, r is the particle radius, $\boldsymbol{v}$ is the fluid velocity, and $\boldsymbol{u}$ is the velocity of the particle.

The drag coefficient is defined as (DallaValle, 1948):

$$C_d = 0.63 + \frac{4.8}{\sqrt{R_{ep}}} \tag{III .13}$$

where R_{ep} is the Reynolds number.

The Di Felice correction factor χ is given by:

$$\chi = 3.7 - 0.65 \exp\left[\frac{-(1.5 - \log(R_{ep}))^2}{2}\right] \tag{III .14}$$

The Reynolds number is calculated as:

$$R_{ep} = \frac{2\rho_f r \left|\boldsymbol{u} - \boldsymbol{v}\right|}{\mu} \tag{III .15}$$

Therefore, the force exerted by the fluid on a fine particle is given by:

$$\boldsymbol{F_f} = \boldsymbol{F_d} - \frac{4\pi r^2}{3}\rho_f \boldsymbol{g} \tag{III .16}$$

where, $\frac{4\pi r^2}{3}\rho_f \boldsymbol{g}$ represents the buoyant force acting on an individual fine particle.

2.4 Coupling Process

According to Newton's second law, the balance equation is given as:

$$\frac{\partial \boldsymbol{u}}{\partial t} = \frac{\boldsymbol{F_m} + \boldsymbol{F_f}}{m} + \boldsymbol{g} \tag{III .17}$$

where $\boldsymbol{u}$ is the velocity of the particle, t is the time, $\boldsymbol{F}_m$ is the mechanical force acting by the particles connected with current one, $\boldsymbol{F}_f$ is the fluid force acting on current particle, m is the mass of the particle, and $\boldsymbol{g}$ is the gravitational acceleration.

Therefore, the balance equations, for coarse particles and fine particles respectively, are given as:

$$\frac{\partial \boldsymbol{u}}{\partial t} = \frac{K_n X_n + \eta \boldsymbol{u} + \sum_i p_i S_i}{m} + \boldsymbol{g} \tag{III .18}$$

$$\frac{\partial \mathbf{u}}{\partial t} = \frac{K_n X_n + \eta \boldsymbol{u} + \left(3C_d \rho_f \pi r^2 \left|\boldsymbol{u} - \boldsymbol{v}\right| (\boldsymbol{u} - \boldsymbol{v})\right) \phi^{-\chi} - 8\rho_f \boldsymbol{g}}{6m} + \boldsymbol{g} \tag{III .19}$$

In our study, it is supposed that the fluid is compressible, and thus the fluid pressure is the function of the temperature and the density of the fluid. The state equation for the fluid then can be written as:

$$p = f\left(\rho_f, T\right) \tag{III .20}$$

Zhu et al. (2023) try to obtain the relationship between the pore pressure and the volumetric mass of water under saturated vapor pressure and constant temperature, via the best fitting. In case of isothermal process, taking 20°C as an example, the equation simplifies to:

$$p = \frac{\rho_f - 999.75}{4.615 \times 10^{-7}} \tag{III .21}$$

The volumetric mass of the fluid, water for example, is then given as:

$$\rho_f = \frac{M}{V_{tet} - V_{coarse} - V_{fine}} \tag{III .22}$$

here, M is the mass of water in the tetrahedron at the given instance before the material exchange. The flow rate through the current considered pore for a given time step is defined as Q:

$$Q = \sum_{j=1}^{n} \boldsymbol{n_j} \cdot \ \boldsymbol{v_j} A_j \Delta t^f \tag{III .23}$$

where $\boldsymbol{n}_j$ is the normal vector of the flow surface j, $\boldsymbol{v}_j$ is the velocity of the incoming fluid unit corresponding to the flow surface j, A_j is the effective flow area of each unit surface, and Δt^f is the duration of the seepage in current time step.

The new mass of the fluid in the current tetrahedron for the next time step, is then updated as:

$$M' = M_0 + Q\rho_f \tag{III .24}$$

Finally, we obtain the coupled equation for fluid pressure and particle motion:

$$p = \frac{M_0 + \sum_{j=1}^{n} n_j v_j A_j \Delta t^f \rho_f - 999.75V(x)}{4.615 \times 10^{-7} V(x, y, z)} \tag{III .25}$$

where $V(x, y, z)$ is a function of the particle's position.

2.5 Model validation

To validate the performance of the adopted method, a one-dimensional fluid-solid coupling problem is considered initially. Then, this problem is extended to three dimensions, and the DEM-PNM predictions are compared with finite element analysis results. After confirming the effectiveness of the coupled field equations, the development of fine particles migration within the soil in a three-dimensional domain is demonstrated.

Figure III .6 presents the geometric shape of the validation model for soil seepage and the applied boundary conditions. The height of the sample is $L = 1$ m. The upper surface (at $z = 1$ m) is subjected to a constant pressure $p_1 = 1 \times 10^5$ Pa, while the initial pressure inside the soil sample is $p_0 = 0$ Pa (barometric pressure). The soil skeleton is considered to be a homogeneous material with a porosity $\phi = 0.2$. The permeability of the material, K, is specified as 1.0×10^{-10} m^2, and the dynamic viscosity of the fluid, μ, is specified as 1.01×10^{-3} Pa $\cdot$ s. In the numerical computations, the model is constructed by considering 100 material points (Figure III .6), with the diameter of an individual particle of $\Delta x = 0.01$ m, and a time step chosen as $\Delta t^f = 1 \times 10^{-10}$ s. All displacements are constrained, and only seepage flow occurs. The investigated soil sample is assumed to be fully saturated, with the assumption that the fluid is compressible.

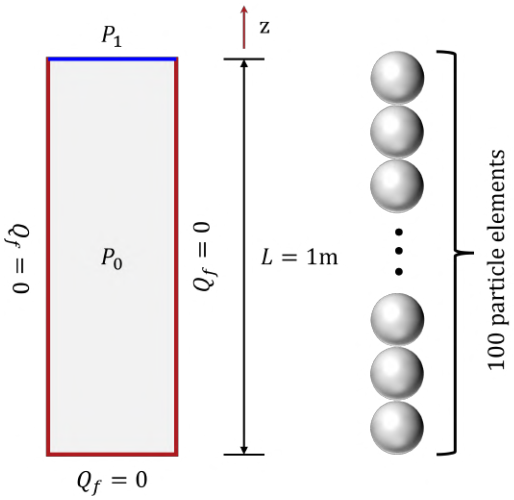

Figure III .6: Geometric shape of the soil seepage validation model and pre-scribed boundary conditions

When considering the one-dimensional seepage problem, for a given representative elementary volume (REV), the flow conservation is given by:

$$\frac{\partial Q}{\partial t} + \text{div}(v) = 0 \tag{III .26}$$

With respect to the definition of density, this equation can be transformed into:

$$\frac{\partial \left(m/\rho_f\right)}{\partial t} + \text{div}(v) = 0 \tag{III .27}$$

Taking into account the influence of porosity, this equation can be modified as:

$$\frac{\partial \left(pV\phi/\rho_f\right)}{\partial t} + \text{div}(v) = 0 \tag{III .28}$$

The flow of low Reynolds number fluids in porous media is described by Darcy's law:

$$\frac{\partial \left(pV\phi/\rho_f\right)}{\partial t} - \text{div}\left[\frac{K}{H\phi} H\phi \text{grad}(p)\right] = 0 \tag{III .29}$$

Furthermore, if we only consider the one-dimensional problem of hydraulic head variation, the governing equation is given by:

$$\frac{\phi V}{\rho_f}\frac{\partial p}{\partial t} = \frac{K}{4.615 \times 10^{-7} H\phi}\frac{\partial^2 p}{\partial x^2} \tag{III .30}$$

Indeed, the computation of parabolic partial differential equations using the finite element method is well-established (e.g., for the heat equation). Therefore, the finite

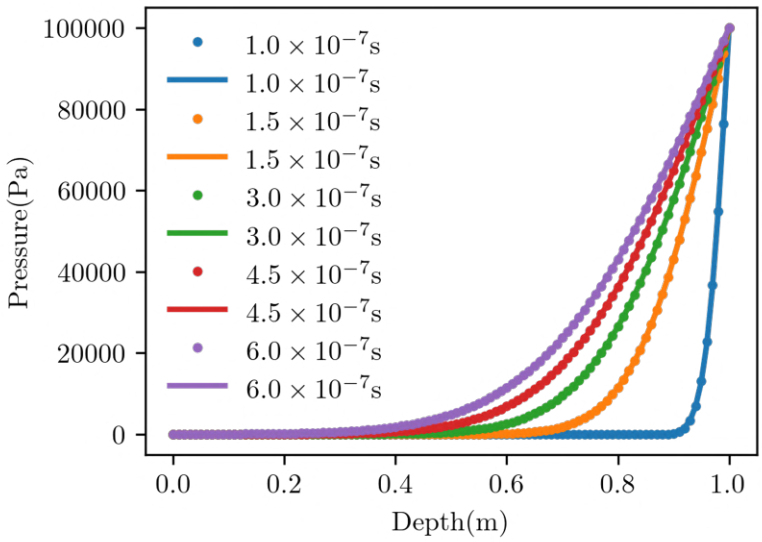

Figure III .7: The comparison of FEM and DEM (1D) calculation results: Lines represent the results of FEM calculations, while dots represent the results of DEM calculations with the proposed approach

element computation results are considered reliable. The hydraulic head variation of this 1D model was computed using the DEM and compared with the results obtained from the Finite Element Method (FEM) (Figure III .7). It can be observed that the results from both methods exhibit good agreement, indicating the accuracy of this method within the DEM framework.

It should be noted that in 3D seepage calculations, the fluid grid is defined using tetrahedral structures, and the manner of fluid transport and pathways differs from the 1D case. Therefore, we validated the 3D tetrahedral grid model using the results obtained from the 1D computations. For the aforementioned model computation, Figure III .8 shows the distribution of fluid pressure obtained using the tetrahedral grid method at a time of 1×10^{-6} s. Each red point represents the pressure of a fluid grid, and the blue line represents the validated results obtained from the 1D computation. It can be observed that the 1D and 3D results exhibit good consistency but also show some differences. The main reason for this discrepancy is that the 1D model assumes a square seepage area and complete uniformity in particle packing. In comparison, the 3D model better reflects the actual conditions. Based on the aforementioned work, we believe that the tetrahedral grid model can be applied to more complex geotechnical problems.

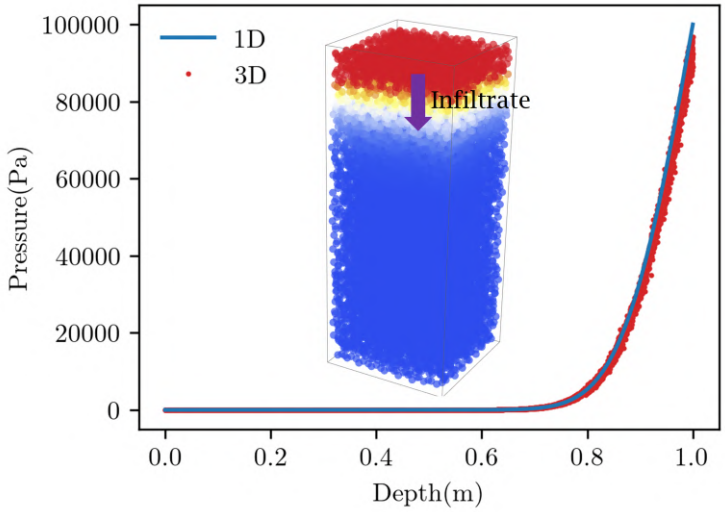

Figure III .8: Distribution of fluid pressure in the validation model computed using the tetrahedral grid method at a time of 1×10^{-6} s

3 Results and discussions

3.1 Modeling and testing of fine particles migration

In this study, the pipeline particle migration process is similar to the laboratory setup by Fleshman and Rice (2014). In the initial stage, a uniform hydraulic gradient is applied to the soil sample to avoid any converging or diverging flow conditions.

3.1.1 Model setup

As shown in Figure III .9(a), the rectangular soil (sand) sample in this study is modeled with dimensions of 10 mm (length) $\times$ 10 mm (width) $\times$ 20 mm (height). Prior to applying the flow, the particles are randomly generated and the settle is not allowed. The flow domain is determined by the tetrahedral structure formed by the coarse particles. It should be noted that, unlike the validation model, here the volume of the tetrahedra is calculated based on Eq.(III .6). Since the tetrahedral grid on the boundary is established based on the virtual particles, their volumes are also calculated based on the position of the virtual particles, which replace the real volumes. The model setup for the boundary using real and virtual elements is illustrated in Figure III .9(b) and Figure III .9(c), respectively.

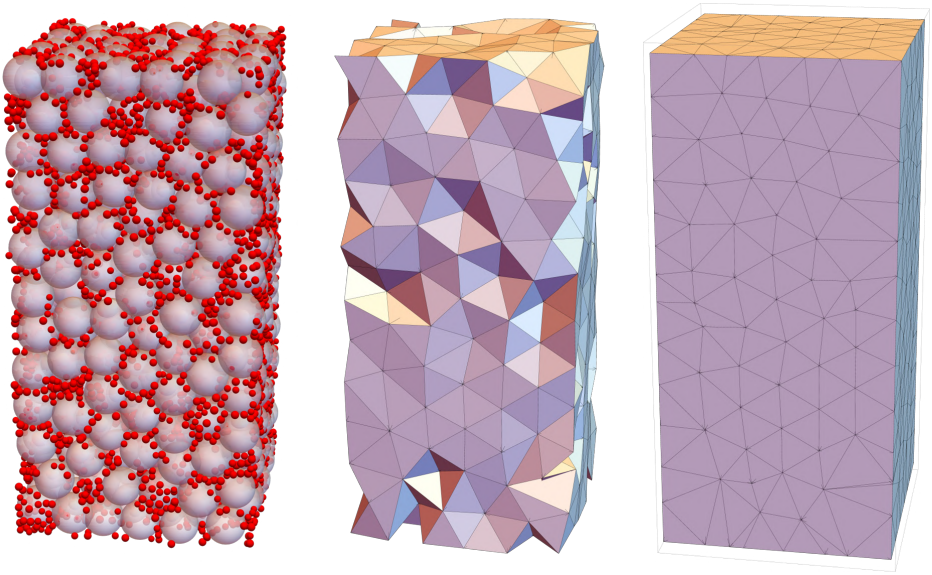

(a) (b) (c)

Figure III .9: The numerical model construction process: (a) particle-packed soil sample: depicts the geometry of the soil sample with particle packing, (b) fluid grid partition before boundary treatment: illustrates the partitioning of the fluid grid before applying the boundary treatment, (c) fluid grid partition after boundary treatment using virtual particles: displays the partitioning of the fluid grid after implementing the boundary treatment with the use of virtual particles

3.1.2 Materials and parameters

In this study, a granular sample with a graded distribution of particles is generated by packing particles in a rectangular empty box Figure III .9(a), and the input parameters are listed in Table 1. In the specimen, the entire model's porosity has been set to 0.25. Sand grains are modeled as perfect spheres, with the average diameter of coarse particles being 5 times larger than that of fine particles. The study takes into account the friction coefficient between particles but does not consider the effects of angularity. Fine particles constitute 5% of the total weight of the specimen. In the numerical samples, the particle sizes of both coarse and fine particles are linearly distributed within the specified range. The fluid enters from the top and exits from the bottom of the model (Figure III .5). The sand grains are modeled as perfect spheres. The soil particles are considered to be perfect spheres. In DEM, the selection of Young's modulus serves as a preparatory step in our simulation. Its significance lies in its crucial role in determining both the DEM time step and particle overlapping. In existing numerical studies, the Young's modulus is defined in

a wide range, from 10^6 Pa to 10^{10} Pa (El Shamy et al., 2010; Xiong et al., 2021b; Yang et al., 2019b; Zhou and Ooi, 2009; Zhou et al., 1999, 2010, 2011). Considering that a smaller Young's modulus allows for larger time steps without significantly affecting the physical behavior of the particle system (Chand et al., 2012), a Young's modulus in the order of 1.0×10^9 Pa is chosen in this study, ensuring sufficiently small particle overlap. Table III .1 contains the other parameters used in this study.

Table III .1: Parameters of the model

Shape	Cube	Porosity	0.25
Particles			
Density	2650 kg/m^3	Friction coefficient	0.5
Young's modulus	1.0×10^9 Pa	Poisson ratio	0.2
Time step	1.0×10^{-7} s		
Coarse particles		*Fine particles*	
Diameter	$1.6 - 1.8$ mm	Diameter	$0.26 - 0.34$ mm
Normal stiffness	4.5×10^8 N/m	Normal stiffness	8.0×10^5 N/m
Tangential stiffness	8.0×10^7 N/m	Tangential stiffness	1.8×10^5 N/m
Particle number	554	Particle number	5195
Fluid			
Dynamic viscosity coefficient	1.0×10^{-3} Pa $\cdot$ s	Gravitational acceleration	9.8 m/s^2
Time step	1.0×10^{-5} s		

The other parameter considered in the model is damping, which measures the ability of energy dissipation during particle collisions. Critical damping is used to dissipate energy effectively. In this study, we set the critical damping at 1%. For multi-element systems, the optimal damping can be obtained using the following semi-empirical formula (Chun et al., 2017):

$$\eta = \frac{d}{V^{1/3}}\sqrt{8mk} \tag{III .31}$$

where V represents the volume of the model, d is the diameter of the element, m is the mass of the element, k is the stiffness of the element.

Apart from the Young's modulus and critical damping, the parameters such as the Poisson's ratio and friction coefficient are given in Table III .1. The Poisson's ratio is considered to have a minor influence on the macroscopic behavior, therefore typical values are assigned to the particles and boundary elements. The choice of friction coefficient between particles is not a trivial matter for PNM-DEM simulations, as the critical state friction angle increases with the increase in the interparticle friction angle, according to Horne's theory. In this study, the friction coefficient for particles is set to 0.5 (Cavarretta et al., 2010; Fall et al., 2014). Regarding the influence of water flow on the interparticle friction coefficient, there is currently insufficient research. Fall et al. (2014) indicates that the sliding friction on sand can be greatly reduced by adding some but not excessive amounts of water. In this study, the soil is fully submerged, so there is no further reduction in the friction coefficient. As for the fluid phase, a compressible and laminar Newtonian fluid flow is assumed. In the case of pipe mass migration, the fluid medium is water, and the flow remains in a relatively low Reynolds number regime.

After the simulation, a further check on the Reynolds number of the particles was conducted. It was found that under the hydraulic gradient used in this study, the Reynolds number of the particles ranged from 0 to 600, indicating a well-established laminar flow regime. Throughout the simulation, the particles underwent 100 iterative motions while the fluid was updated once. The density and viscosity of the water, along with other fundamental properties, can be found in Table III .1.

3.1.3 Boundary conditions

In traditional laboratory pipe experiments, the hydraulic gradient along the soil sample is typically controlled by two separate water tanks. In this study, the hydraulic gradient is derived from the equivalent pressure difference, i.e., $i = \frac{\Delta h}{L} = \frac{\Delta p}{gL}$, where Δh is the head difference across the sample, L is the sample height, Δp is the applied hydraulic pressure difference between the inlet and outlet boundaries, and g is the acceleration due to gravity. In the numerical simulation, the pressure difference between the inlet and outlet boundaries is set to 10 kPa and 0 kPa, respectively, resulting in a linear distribution of water pressure within the sample. It should be noted that the hydraulic pressure difference is the ratio of pressure difference to water density. In the experiments conducted by Fleshman and Rice

(2014), the inner wall of the container was coated with a layer of sand grains. Therefore, in our simulation, the mechanical properties of the wall are set to be the same as those of the particles.

3.1.4 Calculation results

In the testing of the model, the simulation was run for a total of 0.05 s. As shown in Figure III .10(a), the model was divided into five zones (labeled I-V), and the mass of fine particles in each zone was monitored. The particle content, defined as the ratio of the mass of fine particles in each zone to the total mass of fine particles in the model, is plotted in Figure III .10(b). It can be observed that the particle content varies the most in Zone V and the least in Zone IV. The particle content in Zones I and II decreases with the infiltration time, while the particle content in Zone V increases with the infiltration time. The particle content in Zones III and IV shows little variation, indicating that the particle clogging and loss are balanced. It is worth noting that the particle migration in Zone I has not stabilized. Therefore, in subsequent calculations, a longer duration was considered to determine the critical particle content for stable particle migration, which will help address some important engineering issues.

Figure III .11 shows the variation of particle content in Region I over time, depicting the evolution of mass migration in three stages: initial stage, deceleration stage, and stable stage. In the initial stage, particles in the region are mobilized by fluid flow and gravity. During this stage, a significant amount of fine particles is transported, leading to a rapid increase in fluid velocity within the pores. The mass migration curve exhibits a roughly linear trend during this stage. In the deceleration stage, the mass migration rate gradually slows down, and the fluid velocity within the pores stabilizes. In the stable stage, the particle migration process tends to reach a steady state, with fluid velocity within the grid remaining nearly constant. During this process, a discontinuity in the mass migration rate (highlighted in red in Figure III .11) indicates a rapid loss of fine particles in localized pores during that period, highlighting the high sensitivity of particle migration in these regions.

In Figure III .12, we have sliced the simulated specimen along the $x = 0.05$ plane, and we can observe the difference in particle distribution at two different time points: 0 s and 0.05 s. The seepage process can be divided into two states: particle clogging and erosion. When particles accumulate in a pore, the porosity decreases, resulting in a decrease in seepage velocity and a smaller fluid force acting on the particles, leading to particle clogging. Conversely, as fine particles are washed away under seepage, the porosity

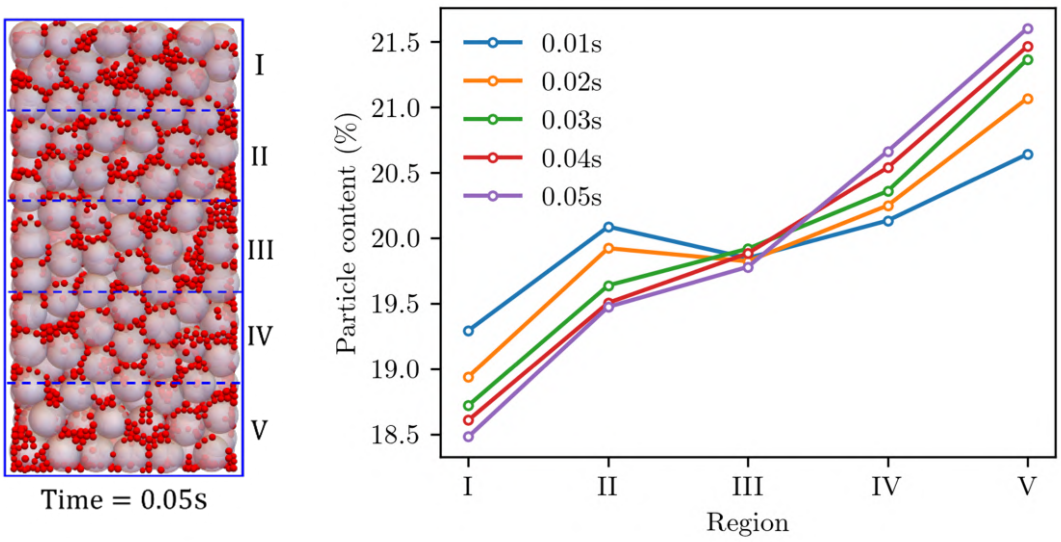

(a) (b)

Figure III .10: Illustrates the variation of particle content: (a) The model is divided into five regions (labeled as I-V) when the infiltration duration is 0.05 s. (b) The ratio of the mass of fine particles in each region to the total mass of fine particles in the model is monitored

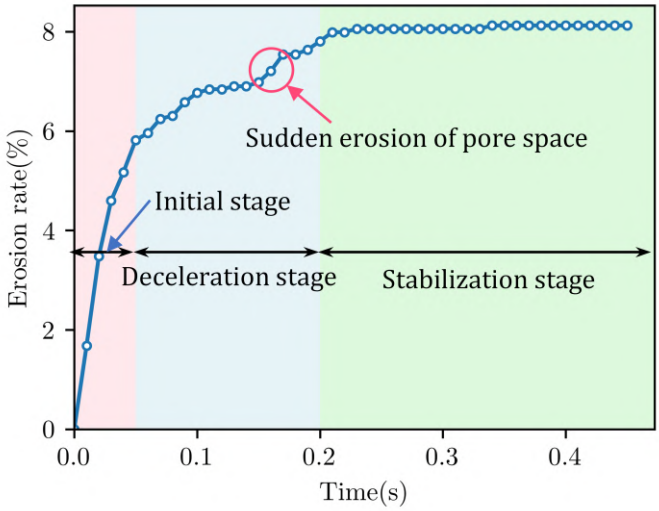

Figure III .11: Variation of cumulative mass migration rate over time in Region I

increases, and the fluid force becomes stronger, resulting in significant erosion.

Figure III .13 shows the distribution of fluid velocity at different times. It can be

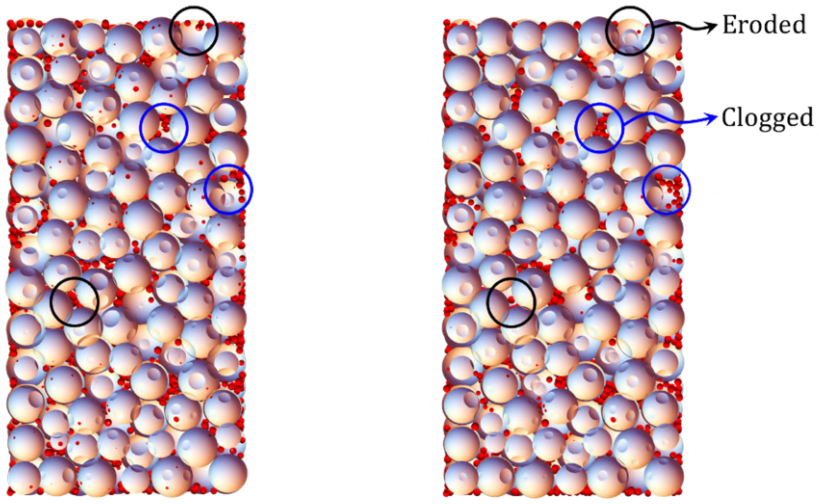

(a) (b)

Figure III .12: Cross-sectional profile of the model along the $x = 0.05$ plane at two different time points: 0 s and 0.05 s

observed that the distribution of fluid velocity remains relatively stable over time. To further investigate the variation of flow velocity during the migration process, we analyzed the average velocity in Region I (as shown in Figure III .14). The average flow velocity in this region initially increases and then stabilizes over time, which is consistent with the relationship between cumulative mass migration rate and time shown in Figure III .11. This indicates that after fine particle migration occurs, the increase in porosity leads to an increase in fluid velocity.

3.2 Development of the dynamic fluid mesh

In gap-graded soils, the content of fine particles has a significant impact on the internal particle arrangement of the soil. When the content of fine particles is high, the internal particle arrangement becomes more complex.

Specifically, an increase in the content of fine particles leads to the occurrence of more underfilled, filled, and overfilled states within the soil Figure III .15. These different filling states affect the pore channels and particle skeleton structure of the soil, thereby influencing the stress state of the soil.

Previous studies have demonstrated that an increase in fine particle content intensifies particle migration processes within soils (Shire et al., 2016). A higher proportion of fines tends to exacerbate soil instability by altering pore structure and impeding fluid

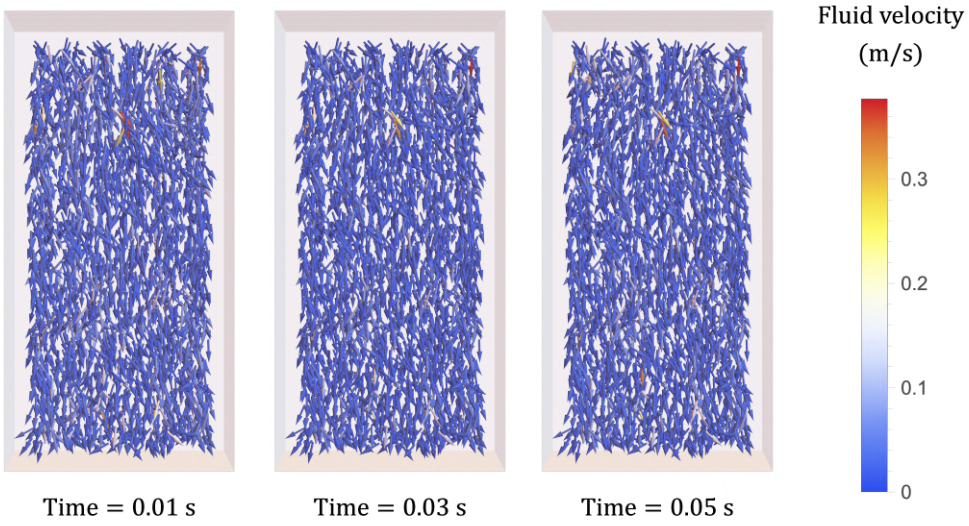

Figure III .13: Variation of fluid velocity during the migration process: the red arrows indicate higher fluid velocities, resulting in faster mass migration rates

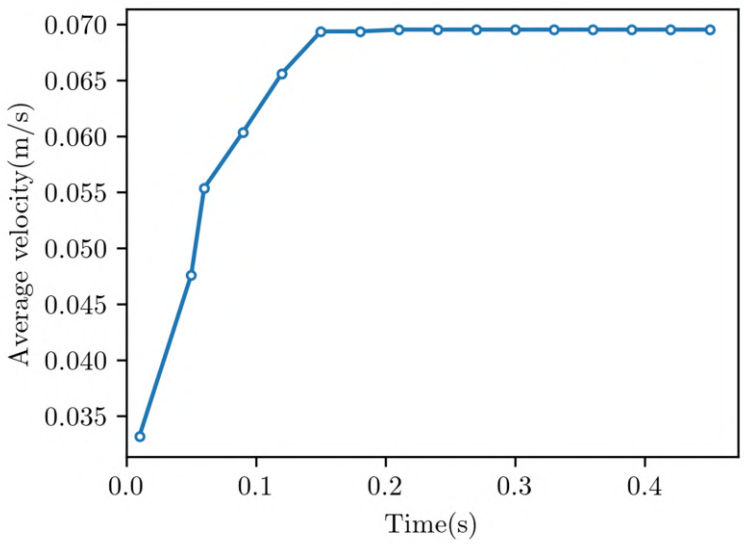

Figure III .14: Variation of average velocity magnitude in Region I with time

flow. Specifically, fine particles can accumulate within pore spaces, leading to clogging that restricts seepage channels, increases internal hydraulic resistance, and consequently amplifies the rate and extent of mass migration.

However, the behavior of underfilled and overfilled soils is more complex. In these states, both the clogging effect of fine particles and the weakening effect of coarse particles

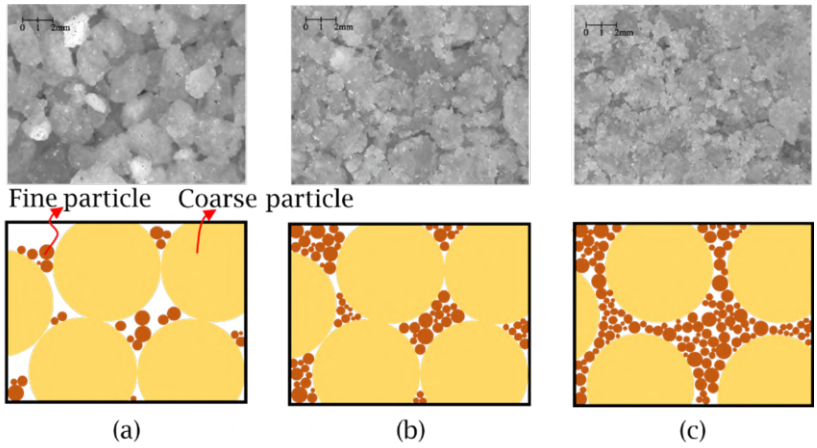

Figure III .15: Three Filling States of the Soil (Ouyang and Takahashi, 2016): (a) Underfilled; (b) Filled; (c) Overfilled

influence the soil. The clogging effect of fine particles can slow down the onset of particle migration, while the weakening effect of coarse particles promotes it. Therefore, at higher fine particle contents, the internal particle arrangement of the soil becomes more complex, requiring further research to better understand the influence of fine particles on the soil's stress state and migration dynamics.

Given the above background, the Dynamic Fluid Mesh (DFM) method is an effective simulation tool that can accurately describe the complex stress state and particle structural changes in the soil (Zhang et al., 2020). It is particularly useful in the computation of interactions between fluid and solid phases. In the soil, when the particle skeleton undergoes movement during loading or seepage processes, the dynamic fluid mesh method can capture the deformation of the mesh. When significant movements of coarse particles occur, the mesh is reconfigured into a tetrahedral structure to adapt to the new particle positions. Especially when considering the scenario of fine particles overfilling into the pores of coarse particles, the dynamic fluid mesh method can handle large particle displacements and ensure that the mesh structure in the computation remains consistent with the actual situation.

In the DFM method, a key issue is how to regenerate the hydraulic conditions. In this study, we recorded the pressure and positions of tetrahedral mesh in each cycle. Before the next cycle calculation, we called the old (previous cycle) fluid mesh data, found the closest old mesh, and assigned the hydraulic conditions to the new mesh (Figure III .16). This way, even if significant displacements of coarse particles occur, the redefined tetrahedral mesh and the fluid solver conditions are updated promptly, ensuring the accuracy of the

computation.

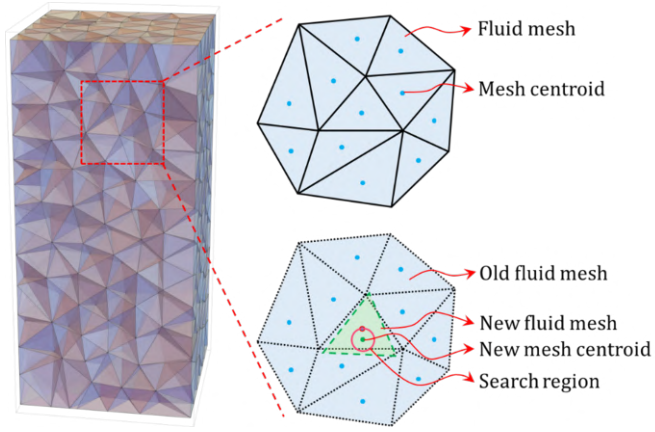

Figure III .16: Data assignment search after fluid mesh position changes in the DFM method

In summary, the dynamic fluid mesh method holds significant value in simulating the mechanical behavior and structural changes of soil with a higher proportion of fine particles. This approach effectively captures particle movement and reassembly, enhancing the accuracy and reliability of computational results. Nonetheless, further experimental and numerical investigations are necessary to comprehensively understand the impact of fine particle content on soil stress and its correlation with fine particle migration behavior. To provide more insights, we conducted simulations for an additional model with 30% fine particle content and 0.4 porosity, maintaining the same parameters as the previous case. Notably, this model exhibited more pronounced fine particle loss and consequential mesh changes (Figure III .17). In conclusion, this method adeptly models the motion of coarse particles and efficiently updates the mesh.

4 Conclusions

This chapter introduced a novel DFM-DEM coupling method to simulate fine particle migration in embankments. The model effectively captured permeability changes due to particle movement and their feedback on fluid interactions. A layered analysis approach provided a realistic representation of mass migration evolution in gap-graded soils.

The results indicate that particle migration evolves through three stages: an initial linear increase, a deceleration phase, and a stable phase where migration nearly ceases. Seepage behavior alternates between particle clogging (reduced porosity and velocity) and active migration (increased porosity and fluid effects). The method also performs well in

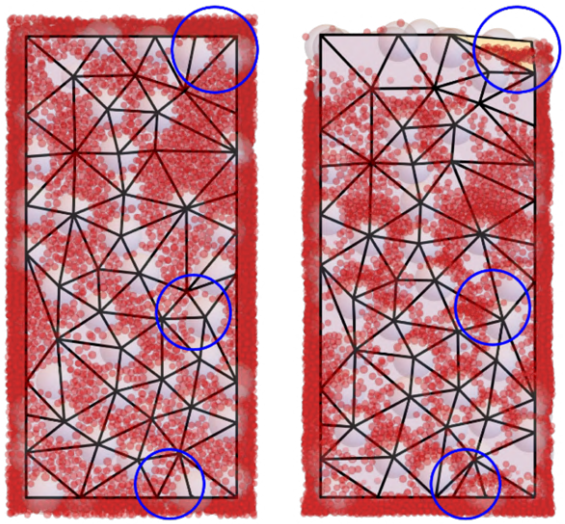

(a) (b)

Figure III .17: Changes in fluid mesh before and after particle migration: (a) Before migration, (b) After migration. The blue circles in the figure indicate the main areas where mesh changes occur. The mesh is shown in opaque, while particles are shown transparently within the blue circles

dynamic fluid grids, accurately modeling particle movement and soil mechanics.

However, two limitations remain: difficulties in precisely calculating porosity in flattened pores and potential inaccuracies in water pressure estimation when fine and coarse particle sizes are similar. Future improvements, particularly integrating Lattice Boltzmann Method (LBM) techniques, could enhance model accuracy in simulating fine particle movement and mass migration dynamics.

Chapter IV

Numerical Simulation of the Impact of Multiple Factors on the Suffusion Sensitivity of Accumulated Granular Materials

1 Introduction

Soil instability induced by seepage is a complex process governed by the interplay among soil structure, hydraulic conditions, and particle-scale interactions. Although experimental investigations have provided valuable insights into the underlying mechanisms, significant challenges remain in capturing the dynamic evolution of soil porosity, fine particle migration, and the development of preferential flow paths under varying hydraulic forces. Numerical modeling serves as a powerful tool to complement experimental studies, allowing for a detailed investigation of these processes at both macroscopic and microscopic scales. By integrating numerical simulations with experimental observations, a more comprehensive understanding of seepage-induced mass migration can be achieved, ultimately improving predictive capabilities for geotechnical applications.

This chapter presents a numerical study using the Discrete Element Method coupled with the Dynamic Fluid Mesh (DEM-DFM) to simulate fine particle migration in granular materials. The model evaluates the effects of initial porosity, hydraulic gradient, and fine particle content on the progression of mass migration. By analyzing key parameters such as sample porosity, mass migration rate, fine particle displacement, and local particle

movement characteristics, the study provides a detailed assessment of how soil structure evolves under hydraulic forces. Additionally, the influence of fine particle content on mass migration is examined to determine its role in clogging behavior and permeability evolution. Experimental data are used to validate the numerical approach, ensuring its reliability in capturing particle migration behavior. The findings contribute to refining predictive models of seepage-induced soil instability and enhancing the understanding of granular structure evolution under hydraulic loading, providing valuable guidance for the design of geotechnical systems resistant to fine particle migration.

2 Model setup

To calibrate and validate the numerical model, a seepage-induced particle migration experimental setup wasestablished, as illustrated in Figure IV .1. The configuration, components, and operational procedures of this setup are identical to those described earlier in Chapter II , specifically in Figure II .1. This apparatus primarily consists of a gradient-controlled water supply system, an particle migration specimen container, an eroded particle collection device, and a seepage water collection system. The experiment was conducted in a cylindrical acrylic barrel with a diameter of 100 mm and a height of

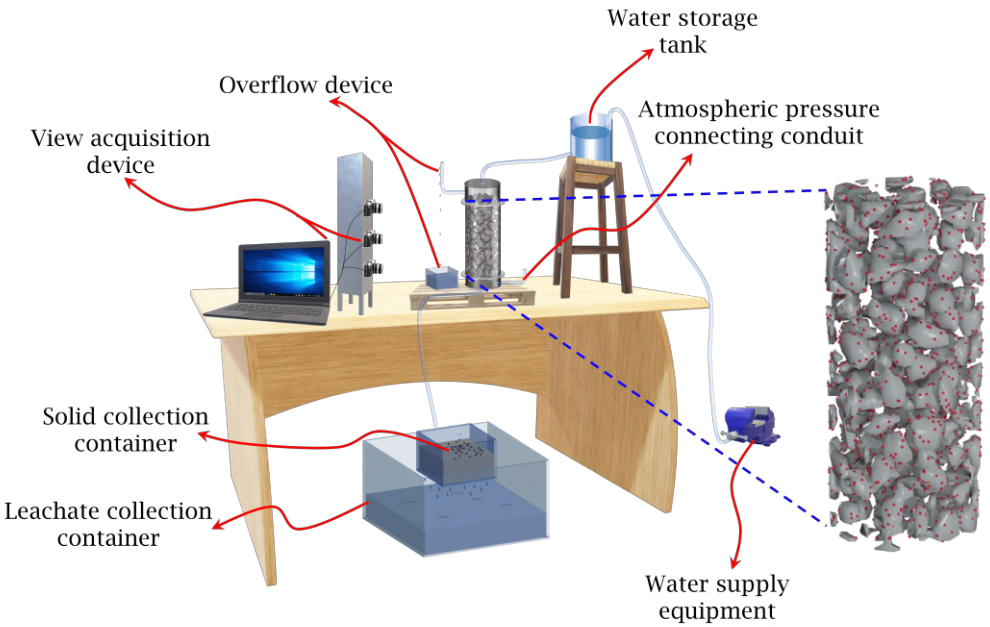

Figure IV .1: Schematic diagram of the fine particle migration test apparatus

250 mm. The water inlet, positioned above the sample, was regulated by the water supply system to adjust the hydraulic head (hydraulic gradient). Simultaneously, a collection device was employed to gather eroded particles and outflow water. Additionally, imaging equipment was utilized to observe internal changes. Fused quartz sand, known for its minimal impurities and stable properties, was used as coarse particles in transparent soil experiments Figure II .2(a). Since the internal movement of fine particles could not be directly observed, dyed colored sand was substituted for particles smaller than 0.25 mm during sample preparation to enable tracking Figure II .2(b). The particle size distribution (PSD) of these particles is represented by the black line in Figure IV .2. In this setup, a coarse sand buffer layer was placed atop the sieve, containing coarse sand with diameters greater than 2 mm (larger than the sieve aperture). The gradient-controlled water supply system comprised a water tank and an overflow pipe. The overflow pipe was positioned at the same level as the top of the cylindrical specimen, with the hydraulic head controlled through the overflow outlet. To maintain a stable and controlled hydraulic gradient during the simulation, a gradient-controlled water supply system was implemented. This system consists of a fluid inlet at the top boundary and an outlet at the bottom, where fluid is introduced at a constant pressure while the outlet is maintained at atmospheric pressure. By applying a fixed pressure difference between the inlet and outlet, a stable hydraulic head is established across the sample. This setup ensures a consistent hydraulic gradient throughout the seepage process. In this study, experiments were primarily conducted under hydraulic heads of 0.2 and 2.0.

In this chapter, simulations were performed on cylindrical specimens that matched the dimensions of the experiments (Figure IV .3(a)). As shown in Figure IV .2, the particle size distribution (PSD) used in the numerical simulations differs from that of the experimental material. To reduce computational complexity while retaining key features relevant to fine particles migration, a simplified binary PSD was employed, consisting of coarse particles (10–20 mm) and fine particles (2.5 mm). This simplification follows common practice in DEM studies (Wang et al., 2022b; Zhu et al., 2020). Although the PSD is not identical to the experimental one, it preserves the contrast in grain sizes and fine content (15%) necessary to study fine particle migration under seepage flow. The observed trends in particle migration behavior are thus expected to remain qualitatively consistent with physical phenomena.

During model generation, a rigid shell was created using a cylinder and a disc. Subsequently, the circular disc at the bottom was replaced by a square-shaped filter to better represent drainage conditions. The outlet filter is modeled as a fixed square mesh with

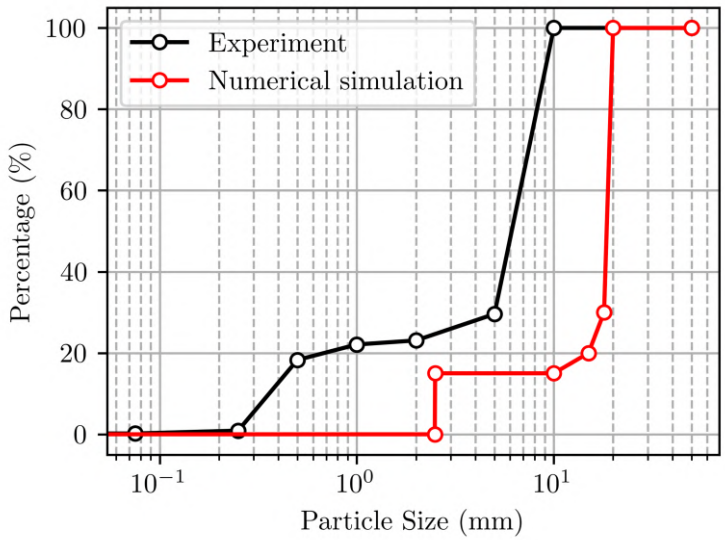

Figure IV .2: The particle size distribution of the sample used for experimental and numerical comparisons

openings of 10 mm × 10 mm (Figure IV .3(b)), which is approximately four times the diameter of the smallest particles. This configuration allows fine particles to pass through under hydraulic flow. Gravity was applied during sample preparation and allowed to stabilize prior to the application of hydraulic gradient. No fine particle migration was observed under gravity alone in the absence of fluid flow. Tetrahedral meshes were established based on the positions of coarse particles in the domain, with approximate treatment at the boundaries to ensure free movement of fine particles within the domain. The boundary conditions for the fluid were considered as unidirectional flow, with fluid entering from the top and exiting from the bottom. The surrounding surface was treated as impermeable boundaries.

2.1 Model parameters

Due to the current research focus on the interaction between fluid and particles, as well as between coarse and fine particles, the damping coefficient in the Discrete Element Method (DEM) is set to 1% of the optimal damping to reduce intense collisions between high-energy particles (Liu, 2021b). To ensure computational efficiency and maintain the particle model's stiffness similar to the experimental material, the particle's elastic modulus is set to 9.0×10^7 Pa (Zhou and Ooi, 2009), with normal and tangential stiffness values set at 6.0×10^5 N/m and 1.0×10^5 N/m (Zhang et al., 2020), respectively. In this study, a

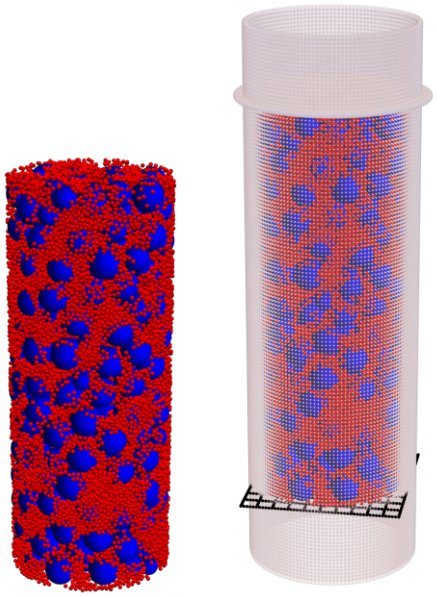

(a) (b)

Figure IV .3: Numerical model of the specimen and percolation device: (a) Cylindrical specimen, where blue spheres represent coarse particles and red spheres represent fine particles; (b) Shell restricting the displacement of the specimen, with a solid disc on top and a 10 mm-wide filter at the bottom of each cell

sliding friction coefficient of 0.5 is applied. Only spherical particles are used, and rolling resistance is not included. Thus, the influence of particle angularity and shape is only partially captured (Li and Smith, 2023, 2025).

Regarding the fluid, it is assumed to be a Newtonian fluid with a dynamic viscosity of 1.0×10^{-3} Pa·s, matching the properties of pure water at a pressure of 100 kPa and a temperature of 20°C. The time step for particle motion in the DEM simulation was set to 1.0×10^{-6} s. This value was chosen to ensure numerical stability based on the critical time step criterion, which depends on particle stiffness and mass. Specifically, the critical time step, Δt, was estimated following the approach described by Li and Smith (2025), where

$$\Delta t \leq \pi \sqrt{\frac{m}{k_n}} \tag{IV .1}$$

with m being the particle mass and k_n the normal contact stiffness of particles.

For fluid calculations, the time step is chosen to ensure convergence of the pressure-velocity coupled fluid phase equations (Muhammad, 2021), set to 1.0×10^{-4} s in this study. Other parameters are listed in Table IV .1.

Table IV .1: Input parameters used in the numerical simulation

Parameters	Value	Unit
DEM solid phase		
Density	2650	kg/m^3
Porosity	0.4	
Young's modulus	9.0×10^7	Pa
Friction coefficient	0.5	
Poisson ratio	0.2	
Normal stiffness	6.0×10^5	N/m
Tangential stiffness	1.0×10^5	N/m
Time step	1×10^{-6}	s
Gravitational acceleration	9.8	m/s^2
Fluid phase		
Fluid viscosity	1×10^{-3}	Pa·s
Time step	1×10^{-4}	s

2.2 Model validation

In this study, we define the cumulative mass loss of fine particles relative to the total mass of the initial sample as the mass migration rate. As illustrated in Figure IV .4, when fine particles filter out through the mesh, we consider that the particle is completely eroded, and its mass is accumulated in the eroded mass. Therefore, the mass migration rate can be calculated using the following formula:

$$m_e = \frac{M_e}{M_e + M_u} \tag{IV .2}$$

where, m_e represents the mass migration rate of the sample, M_e is the total mass of eroded fine particles, and M_u is the total mass of fine particles that remain uneroded.

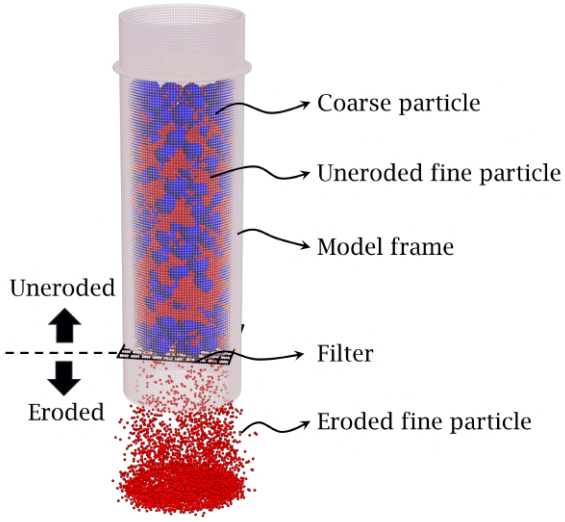

Figure IV .4: Illustrates the migration process of fine particles in the simulation model

In the experiments, the migration of fine particles occurs gradually, while in numerical simulations, particle displacement happens rapidly. Therefore, we use dimensionless time parameters to compare experimental and simulation results, but the analysis is presented in terms of experimental time. It's noteworthy that the onset of fine particle movement in experiments occurs significantly earlier compared to the migration time in the model. Conversely, in numerical simulations, particles take longer to exhibit noticeable movement, therefore, the earlier simulation periods are not compared with experimental data.

By comparing the mass migration rates over time between experiments and numerical simulations with hydraulic gradients of 0.2 and 2.0, the following conclusions were drawn: Initially, the experimental mass migration rate slightly exceeded the numerical computa-

tion. Experimental data showed a step-like change, aligning with the numerical simulation at the turning point (Figure IV .5). In the mid-term, experimental results remained higher than the numerical simulation. However, beyond the mid-term, experimental results stabilized. In contrast, the numerical simulation did not seem to reach a stable state at the end of the experiment. This disparity may be due to the slower movement of bottom particles in physical experiments caused by longer flow paths or the complex pore structure facilitating particle deposition. To quantitatively evaluate the agreement between numerical and experimental mass migration rates, root mean square error (RMSE) and coefficient of determination (R^2) were calculated (Figure IV .5). For the case with $i = 0.2$, indicating an excellent match. For $i = 2.0$, though the RMSE is slightly larger due to increased complexity in migration behavior at higher hydraulic gradients. These quantitative indicators further support the credibility of the simulation results.

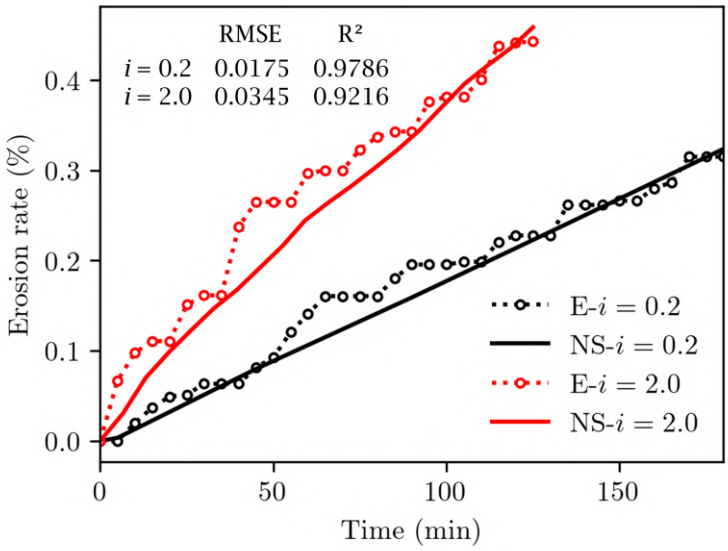

Figure IV .5: Comparison of the proportion of eroded fine particles between experiment and numerical simulation

3 Results and discussions

In order to investigate the migration process under the influence of different factors, we have chosen three different levels for hydraulic gradient and initial porosity. Specifically, the hydraulic gradient i is selected at 0.2, 1.0, 2.0, 3.0 and 4.0, while the initial porosity (n_0) is chosen at 0.3, 0.35, and 0.4. This range covers both low-gradient scenarios and higher values that can reflect localized seepage conditions in real embankment systems.

Although hydraulic gradients in the bulk of a dam structure are typically less than 0.5, localized gradients of 2.0 or greater are frequently reported and may be sufficient to initiate migration processes (Li et al., 2024). Therefore, the selected range allows for a comprehensive analysis of fine particle migration development under realistic and intensified seepage conditions.

3.1 influences of porosity

The evolution of the model's porosity is closely related to the migration of fine particles. Analyzing the variation in sample porosity initially provides insights into the particle migration process, laying the foundation for further analysis of mass migration rates and exploring the intrinsic factors governing particle movement. The overall porosity of the sample is calculated by averaging the porosity of all pores using the formula:

$$n = \frac{\sum_{i=1}^{m_p} n_i}{N_p} \tag{IV .3}$$

where, n represents the sample's porosity, n_i is the porosity of the i-th pore, and N_p is the number of pores.

As shown in Figure IV .6, initially, the porosity decreases to a minimum value, then gradually increases and tends to stabilize. There are some variations in the porosity changes under different initial porosity conditions. Moreover, under all initial porosity conditions, the maximum porosity is not reached when the hydraulic gradient is either at its maximum or minimum. This could be attributed to the fact that, at a relatively low hydraulic gradient ($i = 0.2$), coarse and fine particles initially move more uniformly, with fine particles not participating in the redistribution of the skeleton, leading to sample compaction. However, at higher hydraulic gradients ($i = 4.0$), due to significant initial migration of fine particles, the sample becomes compacted, resulting in the lowest porosity.

Analyzing Figure IV .5(a), when the initial porosity is 0.4, the porosity drops rapidly at first, indicating that the sample compacts from loose to dense. The change in porosity is controlled by the redistribution of the skeleton formed by the coarse particles. Subsequently, the porosity increases slowly and stabilizes, suggesting that the skeleton is mostly stable during this phase and the porosity change is mainly influenced by the migrate of fine particles. Figure IV .5(b) shows that, when the sample's initial porosity is 0.35, the porosity also decreases initially but not as significantly, indicating that the skeleton structure at this initial porosity is relatively stable. Once the skeleton stabilizes, the porosity increases due to the loss of fine particles. In the case of an initial porosity of 0.3 (Figure IV .5(c)), the porosity only slightly decreases before increasing, as the sample's skeleton

(a)

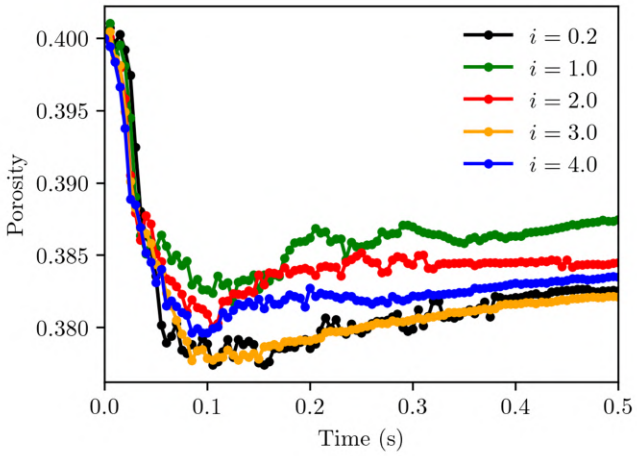

(b)

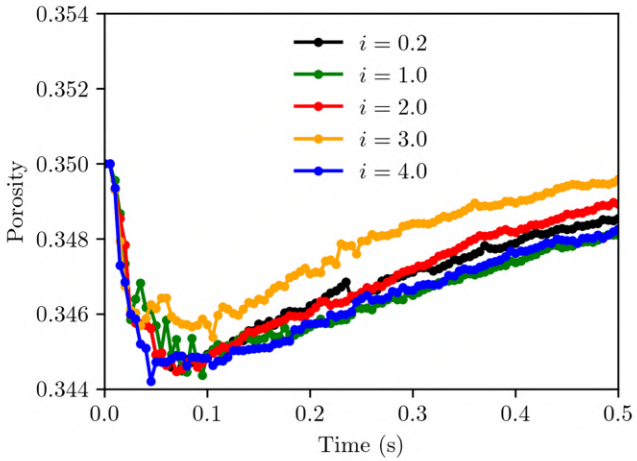

(c)

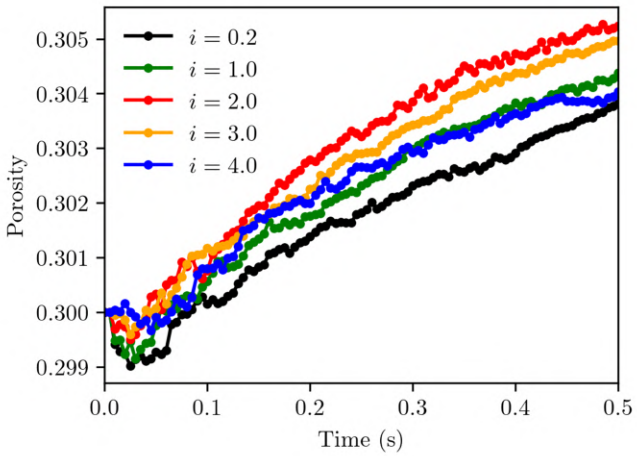

Figure IV .6: Evolution of porosity for different initial porosities: (a) $n_0 = 0.4$; (b) $n_0 = 0.35$; (c) $n_0 = 0.4$.

is stable at the beginning. Notably, after 0.4 seconds, the porosity of the sample with a hydraulic gradient of 4.0 increases very little, indicating that clogging is likely to occur in the later stages under high hydraulic gradients.

Overall, the smaller the initial porosity of the sample, the more stable the skeleton. The sample with an initial porosity of 0.4 and a hydraulic gradient of 0.2 experiences the greatest impact from fine particle migration on its skeleton.

3.2 Particle mass migration rate

Figure IV .7 illustrates the variation in total mass migration rates of fine particles over time for models with three different initial porosities under varying hydraulic gradients. As infiltration progresses, the mass migration rate gradually increases, initially undergoing an acceleration phase of differing durations depending on the hydraulic gradient. Subsequently, the mass migration rate (the mass of particles migrating per unit time) gradually decreases until it stabilizes at a relatively constant value by the end of the process. When the hydraulic gradient is larger, particle migration initiates earlier during infiltration, but the proportion of migrating fine particles varies with the initial porosity.

Figure IV .6(a) shows the effect of different hydraulic gradients on the mass migration rate when the initial porosity is relatively high ($n_0 = 0.4$). During the early to mid-stages of infiltration (time < 0.35 s), the mass migration rate is highest under a hydraulic gradient of 2.0. In the later stages, the mass migration rate peaks under a hydraulic gradient of 4.0, where a higher gradient leads to greater particle migration. The rates for hydraulic gradients between 1.0 and 4.0 are relatively similar, indicating that when the initial porosity is high, further increases in the hydraulic gradient beyond a threshold of 1.0 do not significantly enhance porosity development. This analysis suggests that for a relatively loose initial sample, a higher hydraulic gradient allows the sample to form a stable skeleton structure more quickly while regulating the migration of fine particles.

For an initial porosity of 0.35 (Figure IV .6(b)), the mass migration rate first decreases and then increases with increasing hydraulic gradient, before decreasing again. When the hydraulic gradient is 4.0, the mass migration rate after 0.1 s is noticeably lower than under lower gradients. Additionally, the porosities of the samples under the three hydraulic gradients are nearly identical before 0.1 s, indicating that at the early stage, fine particle movement under a high hydraulic gradient can cause clogging, resulting in a subsequently lower mass migration rate.

In Figure IV .6(c), for the denser initial sample ($n_0 = 0.3$), the maximum mass migration rate occurs when the hydraulic gradient is 2.0. The mass migration rate first increases

(a)

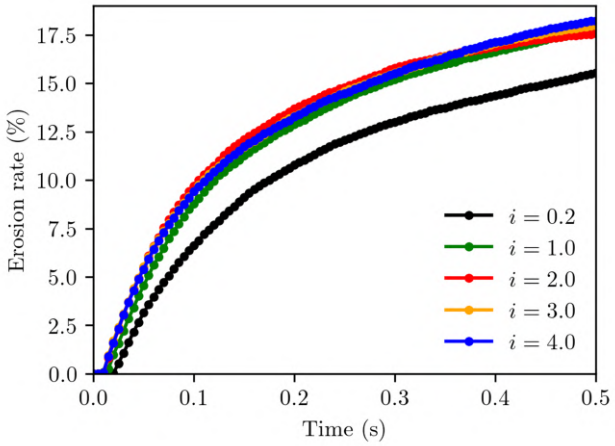

(b)

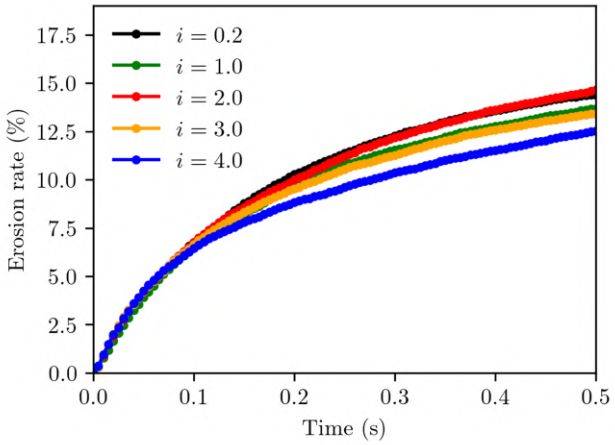

(c)

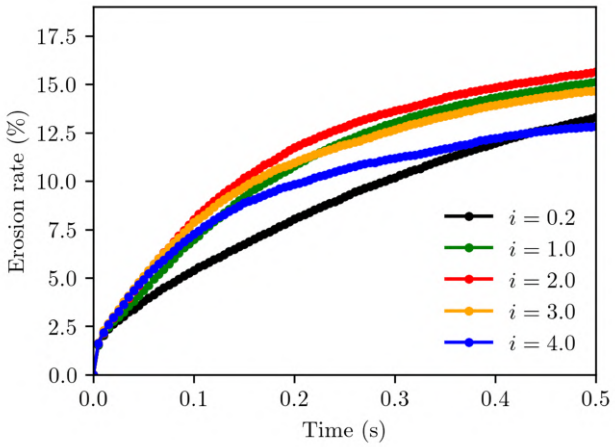

Figure IV .7: Evolution of cumulative mass migration rate: (a) $n_0 = 0.4$; (b) $n_0 = 0.35$; (c) $n_0 = 0.4$.

and then decreases as the hydraulic gradient rises. At 0.4 s, the mass migration rate of the sample under a hydraulic gradient of 0.2 exceeds that under a gradient of 4.0, further indicating that excessively high hydraulic gradients can lead to pore clogging. For samples with this initial porosity, a stable skeleton structure forms early on, and porosity variation is mainly influenced by fine particle migration.

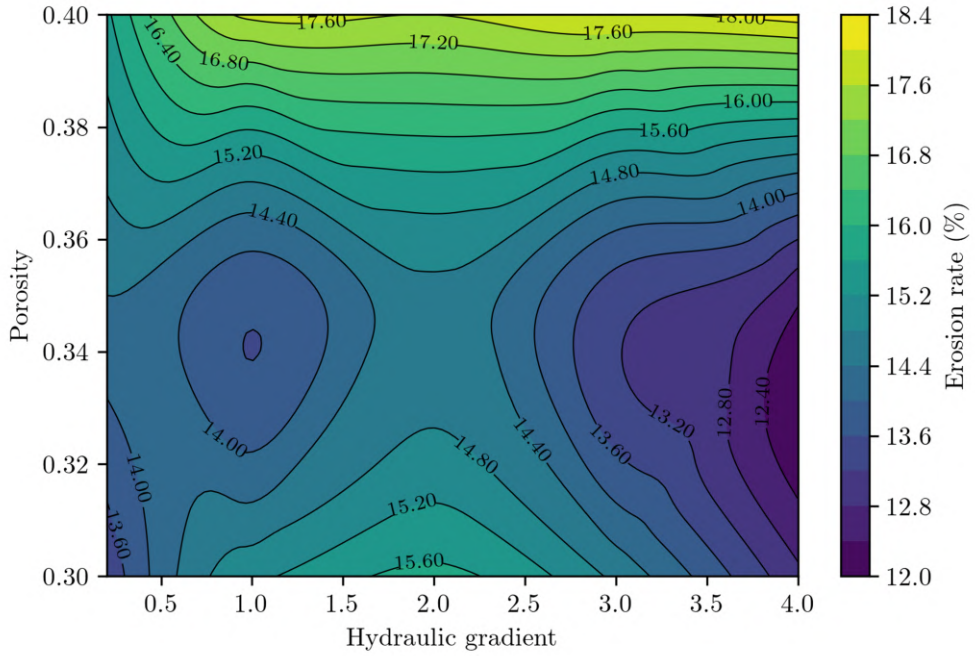

Figure IV .8: Distribution plot of the effect of initial porosity and hydraulic gradient on mass migration rate

Comparing the changes in mass migration rates under the three different porosities, it can be inferred that, due to the effect of porosity on local flow velocity and pore size, there exists a critical gap ratio. Below this critical gap ratio, mass migration weakens as the gap ratio increases; above it, mass migration intensifies significantly. This conclusion aligns with the findings of Wang et al. (2021).

To more intuitively analyze the impact of initial porosity and hydraulic gradient on fine particle migration, the final mass migration rate and total migrated mass under each condition were recorded (see Table IV .2). It can be observed that when the initial porosity is 0.4 and the hydraulic gradient is 4.0, the mass migration rate is the highest. On one hand, larger porosity facilitates the movement of fine particles within the pores, and on the other hand, a higher hydraulic gradient exerts a stronger drag force on particle movement. The maximum migrated mass occurs when the initial porosity is 0.3 and the hydraulic

Table IV .2: Mass migration rate and cumulative migrated mass under different initial porosities and hydraulic gradients

Initial porosity	Hydraulic gradient				
	0.2	1.0	2.0	3.0	4.0
0.40	15.5% (60.7g)	17.7% (69.3g)	17.6% (68.7g)	18.0% (73.0g)	18.2% (71.1g)
0.35	14.4% (60.9g)	13.7% (57.8g)	14.7% (62.1g)	13.4% (56.7g)	12.5% (53.0g)
0.30	13.3% (60.4g)	15.1% (69.0g)	15.7% (71.4g)	14.7% (66.8g)	12.9% (58.6g)

gradient is 2.0. It is hypothesized that under higher compaction, a hydraulic gradient of 2.0 acts as a threshold for particle migration. The main reason is that at the start of seepage, the skeleton is relatively stable, and a lower hydraulic gradient is insufficient to mobilize fine particles, while an excessively high gradient increases the risk of clogging.

In addition, a box plot showing the effect of initial porosity and hydraulic gradient on fine particle migration was generated (Figure IV .9). In Figure IV .9(a), it is evident that the mass migration rate is highest when the porosity is 0.4, lowest when the porosity is 0.35, and least affected by hydraulic gradient. Conversely, when the porosity is 0.3, changes in hydraulic gradient have the greatest impact on mass migration rate. Although earlier analysis showed that the mass migration rate is highest at an initial porosity of 0.4 and a hydraulic gradient of 4.0, Figure IV .9(b) further reveals that the influence of initial porosity on mass migration is greatest when the hydraulic gradient is 4.0 and smallest when the hydraulic gradient is 0.2. The average mass migration rate is highest at a hydraulic gradient of 2.0, further confirming that 2.0 acts as a threshold for fine particle migration.

3.3 Fine particle displacement during hydraulic process

To describe the process of fine particle transport, the most intuitive approach is to focus on the changes in particle displacement. This also provides a fundamental basis for future studies aiming to track the trajectories of representative particles (Dai et al., 2024b). We therefore collected data on the displacement of fine particles within the sample relative to their initial coordinates. Eq.(IV .4) was then used to calculate the average displacement of eroded particles. It is important to note that once fine particles pass through the filter, they are no longer constrained by pore conditions. Therefore, the displacement of filtered

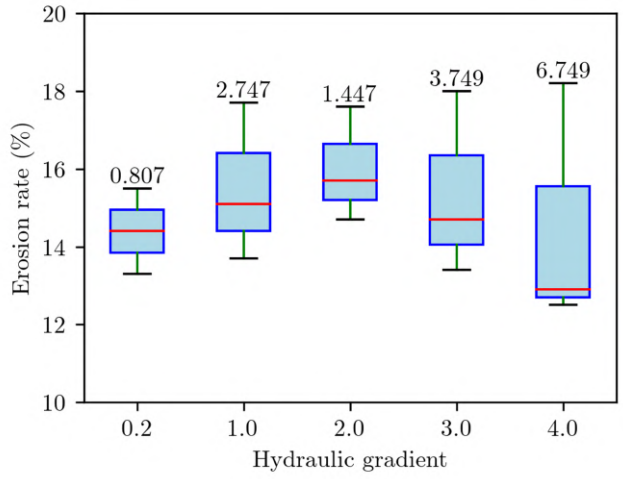

(a)

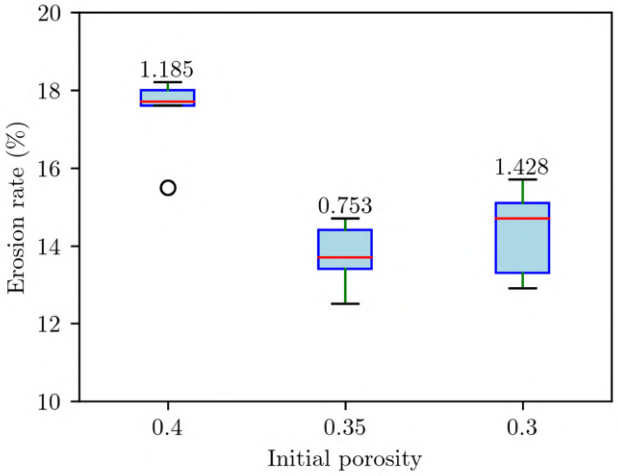

(b)

Figure IV .9: Box plot showing the effect of initial porosity and hydraulic gradient: (a) initial porosity; (b) hydraulic gradient, the numbers above the box plot represent the variance, indicating the magnitude of the impact of one factor on the mass migration rate when the other factor is constant

fine particles is not included in the statistics.

$$\overline{d} = \frac{\sum_{i=1}^{N_f} d_i}{N_f} \tag{IV .4}$$

where, $\overline{d}$ represents the accumulated average displacement of uneroded fine particles, d_i is the cumulative displacement of the i-th fine particle, and N_f is the number of uneroded

fine particles.

Fine particle migration is a process that gradually develops with the depth of the sample. As shown in Figure IV .10, the average displacement $\overline{d}$ of fine particles increases with migration time. Initially, the rate of increase in displacement is very high, indicating extensive movement of fine particles and a rapid increase in the mass migration rate. Subsequently, the rate of increase in displacement gradually decreases and approaches stability. This trend is consistent with the overall change in the mass migration rate of the model. Generally, a larger hydraulic gradient corresponds to greater displacement. When the hydraulic gradients are 2.0, 3.0, and 4.0, the displacements are relatively close, indicating that under this porosity, an increase in hydraulic gradient facilitates particle movement, but the effect is limited due to clogging effects.

For samples with different porosities, larger initial porosities result in greater average displacement of fine particles under larger hydraulic gradients (i.e., 2.0, 3.0, and 4.0). At a hydraulic gradient of 4.0, samples with an initial porosity of 0.4 exhibit the greatest particle displacement in the early stages. For porosities of 0.4 and 0.3, particle displacement increases with the hydraulic gradient (Figure IV .9(a) and Figure IV .9(c)). However, at a porosity of 0.35 (Figure IV .9(b)), the displacement of fine particles is minimal at a hydraulic gradient of 1.0, while it is relatively similar across the other four hydraulic gradients. This is primarily because, at this porosity, the sample is not compacted, and fine particles do not contribute to the formation of the structure. The displacement of fine particles is controlled by the aggregating effects of clogging and filtering under hydraulic action. For the initial porosity of 0.3 (Figure IV .9(c)), the rate of change in fine particle displacement remains high at 0.5 s for samples with a hydraulic gradient of 0.2, indicating significant fine particle migration in the samples. This observation is consistent with the variation in mass migration rate shown in Figure IV .6(c).

3.4 Evolution of force chains during the hydraulic process

Based on the above analysis, a close relationship was observed between fine particle migration and the evolution of the particle skeleton. To clarify this process, we conducted a statistical analysis of force chains within the specimen. A representative sample with an initial porosity of 0.35 and hydraulic gradients of 0.2, 2.0, and 4.0 was selected. All contact forces were classified into strong and weak force chains, based on the average magnitude of all force chains at each time step.

As shown in Figure IV .11, before the onset of significant particle migration (at $t = 0$), the force chain structure was stable, comprising both strong and weak force chains

(a)

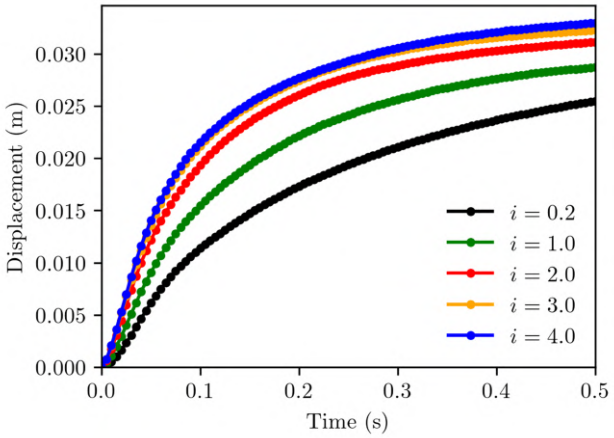

(b)

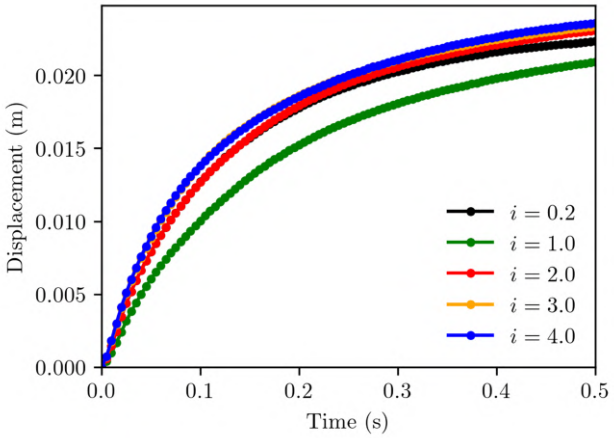

(c)

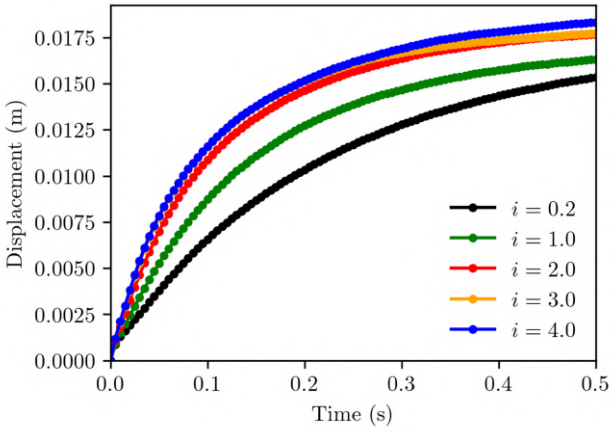

Figure IV .10: The variation of fine particle displacement within the sample model: (a) $n_0 = 0.4$; (b) $n_0 = 0.35$; (c) $n_0 = 0.4$

primarily between coarse particles. However, at the early stage of particle migration initiation ($t = 0.005, \mathrm{s}$), the skeleton structure became unstable due to the movement of

both fine and coarse particles. At this point, particle contacts were sparse, and only a few force chains existed between particles of different sizes.

As the migration process stabilized, coarse particles gradually formed a distinct skeleton, and some pores containing fine particles became blocked, leading to the development of denser force chains. The total number of force chains increased over time, as shown in Figure IV .11, indicating a transition from particle mobility to a more stable packing structure. Notably, at $t = 0.5, \mathrm{s}$, the number of force chains surpassed that observed prior to the onset of particle migration, implying that despite the loss of mobile fine particles, the remaining structure became more densely connected due to rearrangement and blockage.

In terms of force distribution, the initial skeleton was supported by both strong and weak force chains. After the migration process progressed, the final skeleton was predominantly supported by strong force chains among the coarse particles, indicating a mechanically stronger and more stable structure.

Furthermore, the specimen under a hydraulic gradient of 4.0 exhibited the highest number of force chains, suggesting that a higher hydraulic gradient promotes faster stabilization of the granular structure for a porosity of 0.35. This result is consistent with the trends observed in Figure IV .5(b) and Figure IV .6(b), where lower porosity and more pronounced particle blockage led to a lower mass migration rate. In the later stage of particle migration, the number of force chains under all three hydraulic gradients became similar, indicating that the blockage state of fine particles had stabilized.

3.5 Local fine particle migration characteristics

To better understand the behavioral patterns of fine particle movement under seepage, this study conducted a statistical analysis of particle distribution changes at different depths. In the model specimen, it was evenly divided into five layers, each with a height of 0.05 meters, labeled from top to bottom as Layer 1 to Layer 5. We analyzed the ratio of the mass of fine particles in each layer to the total mass of fine particles. Due to the significant size difference between coarse and fine particles in the model, the distribution of fine particles is not entirely uniform. Therefore, before applying a hydraulic gradient, the fine particle content in each layer is not completely the same. In this work, we considered the effect of different hydraulic gradients on the fine particle distribution. With a constant initial porosity of the specimen, the variation in fine particle distribution was generally consistent under each hydraulic gradient, indicating that the hydraulic gradient has a limited impact on fine particle distribution. Consequently, we focused on analyzing specimens with different initial porosities under a hydraulic gradient of 2.0.

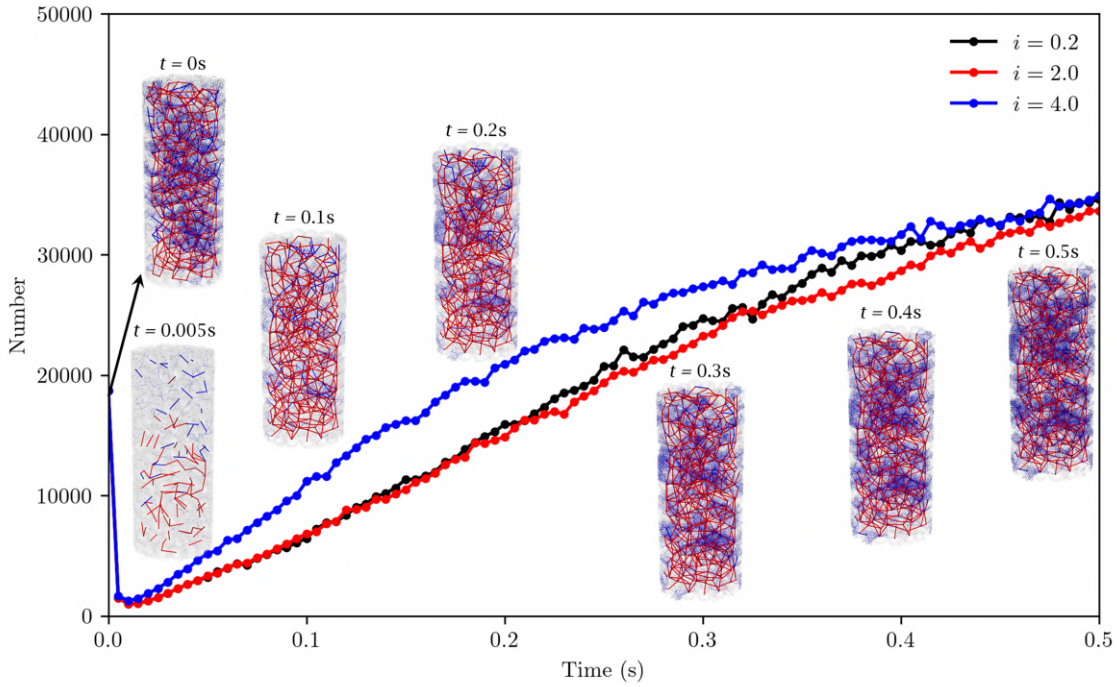

Figure IV .11: Evolution of the force chain state and the number of force chains at different times ($n_0 = 0.35$): Red lines represent strong force chains, and blue lines represent weak force chains, classified based on the average contact force at each time step. Thick lines indicate force chains between coarse particles, while thin lines correspond to force chains involving fine particles

Figure IV .12 shows the changes in fine particle distribution under three different initial porosity conditions. It is evident that for different porosities, the fine particles in the uppermost Layer 1 and the lowermost Layer 5 are continuously decreasing. Moreover, as the porosity decreases, this decreasing trend weakens, and this fine particle reduction mainly occurs in the early stages of seepage. The primary reason is that when the porosity is relatively large, the structure transitions from a loose state to a dense one. In Layer 2, when the initial porosity is 0.35, the fine particles continuously increase, indicating that this layer is prone to clogging under an initial porosity of 0.35. For Layers 3 and 4, the fine particle content shows little change compared to before the application of the hydraulic gradient, suggesting that the inflow and outflow of fine particles in the middle layers of the specimen are relatively balanced. This finding may be further validated in future experiments using colored sands to trace fine particle origins, as demonstrated in recent studies (Dai et al., 2024a).

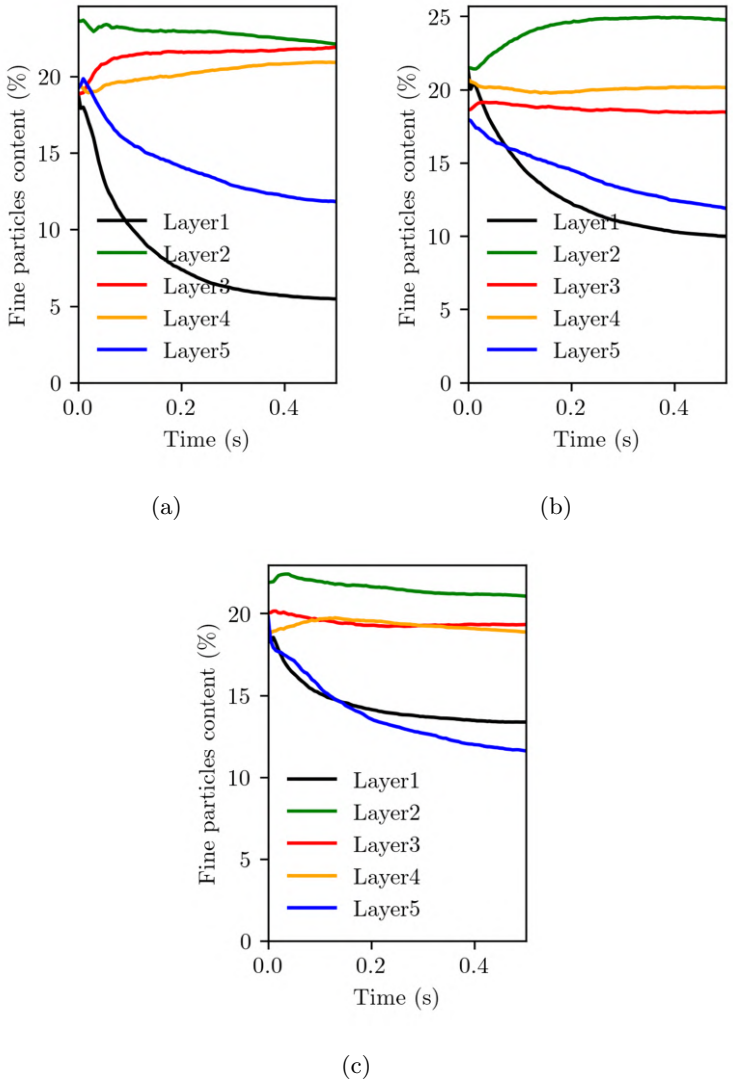

Figure IV .12: Changes in fine particle distribution under different initial porosity conditions: (a) $n_0 = 0.4$; (b) $n_0 = 0.35$; (c) $n_0 = 0.4$

In fact, the phenomena of clogging and filtration during particle migration occur randomly within the fill material. To gain a deeper understanding of the mechanisms driving these processes, an analysis of local particle behavior within the sample was conducted. A representative region beneath the specimen with an initial porosity of 0.35 was selected (Figure IV .13(a)), representing a local accumulation area of particles. Figure IV .13(b) illustrates the evolution of particle accumulation in this region under three hydraulic gradients.

Under hydraulic action, fine particles move through the throats between coarse par-

ticles. When the hydraulic gradient is 4.0, particle migration is significantly reduced compared to gradients of 2.0 and 0.2. The gaps between the upper coarse particles provide pathways for particle transport, while the lower pores show notable differences under the three hydraulic gradients. At a gradient of 4.0, a blocking phenomenon occurs (Figure IV .13(c)), whereas at gradients of 0.2 and 2.0, most fine particles pass through the pore network. The number density of fine particles in this local region was quantified (Figure IV .13(d)). Under a hydraulic gradient of 4.0, the number density initially increases rapidly before decreasing, but remains generally higher than the initial state, indicating that local clogging dominates. In contrast, at gradients of 0.2 and 2.0, the number density is lower than the initial state, showing that fine particles are efficiently transported through the pore network. These results highlight that excessively high hydraulic gradients can promote particle aggregation and clogging within local pore regions.

3.6 Influence of fine particle content

In previous studies, it has been suggested that a fine particle content around 15% may serve as a critical threshold between underfilling and filling (Ouyang and Takahashi, 2016). Clearly, the content of fine particles is a crucial indicator that determines their involvement in the formation of the specimen's skeleton. Therefore, fine particle content is another important factor deserving attention. Although previous studies have investigated the fine particle content of samples with specific gradations, there seems to be a lack of explicit focus on the role of fine particles in the skeleton.

In this context, we briefly discuss the impact of varying fine particle content on the mass migration rate. Considering an initial porosity of 0.35 and a hydraulic gradient of 2.0 as representative conditions in this study, samples with fine particle contents of 5%, 10%, 13%, 15%, 17%, and 20% were selected for calculation and analysis. The changes in mass migration rates at different fine particle contents were obtained (Figure IV .14). It is evident that when the sample is insufficiently filled with fine particles (5%-10%), the mass migration rate decreases as the fine particle content increases. When the fine particle content reaches 20%, the final mass migration rate is higher than that of samples with 10%-15% fine particle content. Additionally, within the first 0.1 seconds of particle migration, the sample with 20% fine particles exhibits an initially slow migration rate, followed by a rapid increase. This behavior can be explained as follows: when fine particles are insufficiently filled, they do not contribute to the skeleton structure, and higher concentrations of fines may cause pore blockages, reducing the mass migration rate. When fine particles are sufficiently filled, some become part of the skeleton structure under

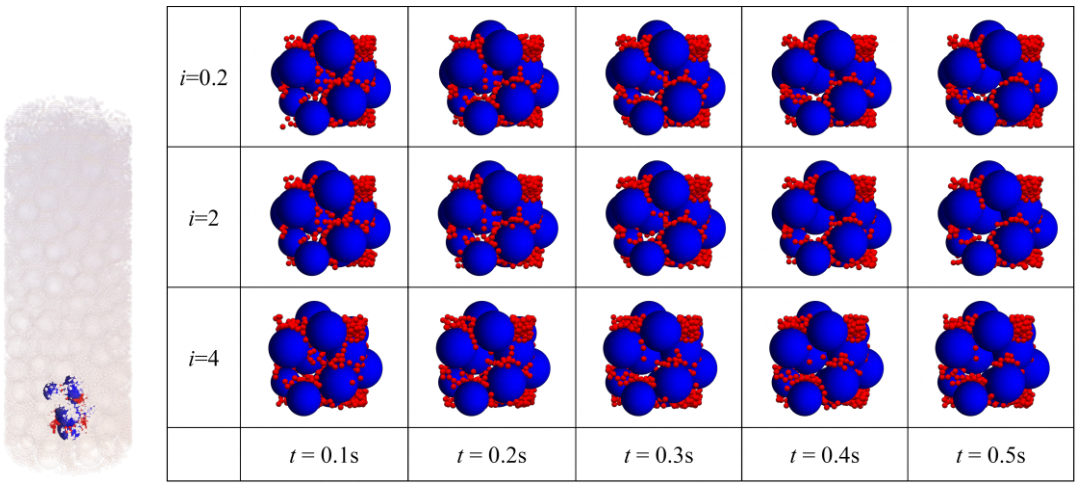

(a) (b)

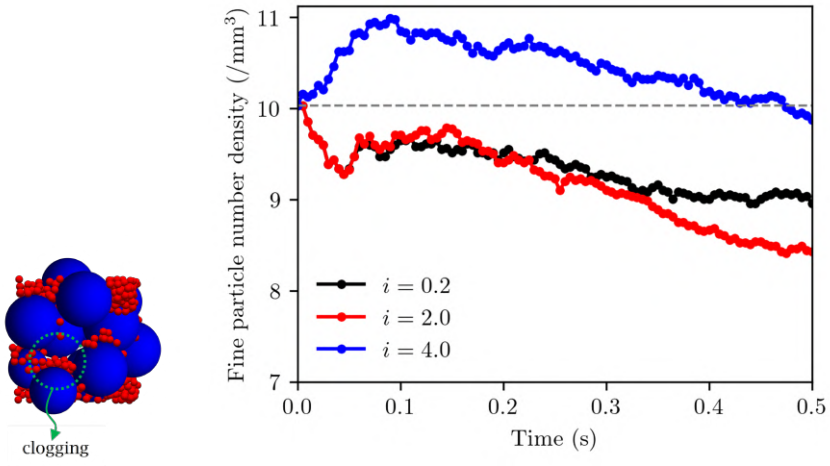

(c) (d)

Figure IV .13: Evolution of the local packing profile: (a) Local packing location, (b) Packing profile evolution, (c) Localized occurrence of clogging, (d) Particle number evolution

hydraulic action, promoting the redistribution of the skeleton, which facilitates particle migration. Once the skeleton stabilizes, the mass migration rate decreases due to the higher particle content.

To validate the aforementioned conclusions, we analyzed the changes in porosity under different fine particle contents (Figure IV .15). When the fine particle content is 5% or 10%, porosity exhibits short-term fluctuations, but the coarse particle skeleton remains essentially unchanged. Subsequently, porosity gradually increases, with changes primarily

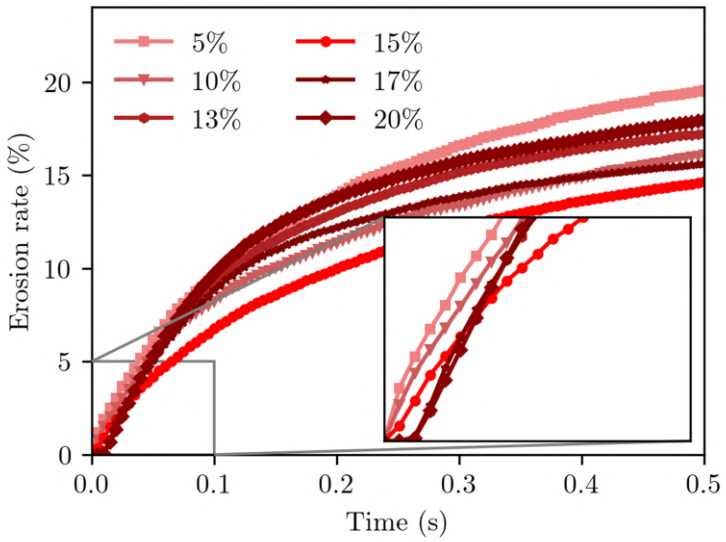

Figure IV .14: The variation in mass migration rate with different fine particle contents

influenced by the migration of fine particles. However, when the fine particle content ranges between 10% and 20%, porosity initially decreases rapidly and then increases. The increase in porosity is not solely due to fine particle migration, as the differences in mass migration rates shown in Figure IV .8 are smaller than the observed differences in porosity. This indicates that, above 10% fine particle content, water flow begins to influence the skeleton structure through the fine particles, promoting an increase in porosity. The impact of fine particle content on soil structure exhibits a threshold at 10%: below this threshold, the soil structure is largely unaffected by fine particles, and the mass migration rate decreases as fine particle content increases. Above this threshold, fine particles integrate into the skeleton, leading to higher mass migration rates.

To further clarify the influence of fine particle content on the structural stability of granular soils, the evolution of force chain networks at various fines contents (FC = 5%, 10%, 15%, and 20%) was analyzed and is presented in Figure IV .16. The proportion of fine particles participating in force chains was quantified to illustrate their role in the overall load-bearing skeleton. The results reveal a distinct threshold behavior:

At low fines contents (FC $\leq$ 10%), the fine particles contribute minimally to the contact force network, with less than 5% involvement in force chains. In this regime, fine particles primarily occupy pore spaces and do not significantly alter the structure of the soil skeleton. This partial pore clogging effect results in decreased permeability and a reduction in mass migration rate.

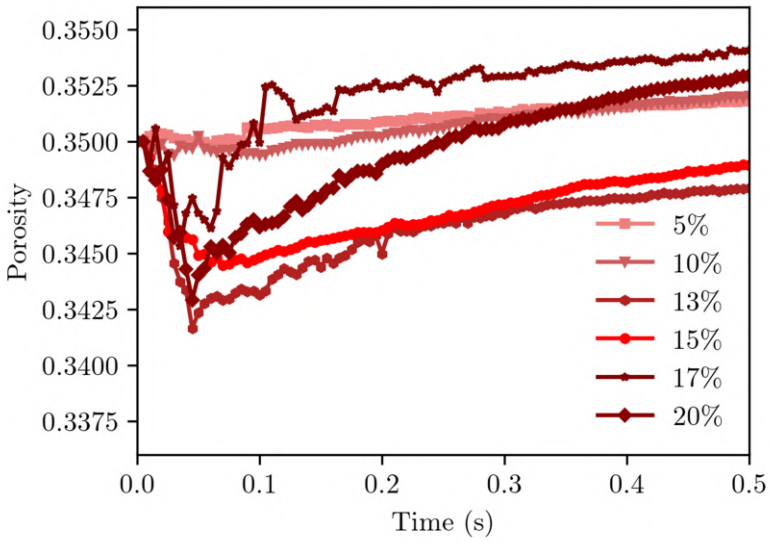

Figure IV .15: The variation in porosity with different fine particle contents

However, as the fine particle content increases beyond 10%, a noticeable transition occurs. Fine particles begin to actively participate in force transmission, with their contribution rising sharply (reaching approximately 80% at $FC = 20\%$). This structural integration suggests that fine particles become a functional part of the load-bearing framework. Although this enhances mechanical interlocking, it also increases the potential for mass migration due to the greater mobility of fines under hydraulic loads. This force chain-based analysis provides direct visual and quantitative evidence supporting the observed particle migration trends (Figure IV .14). The threshold near 10% marks a critical point at which fine particles shift from passive fillers to active structural components, fundamentally altering the mass migration behavior of the system.

In summary, these results indicate differences in particle migration mechanisms under varying fine particle contents. When the fine particle content is 5% (Figure IV .17(a)), the coarse particle skeleton remains largely unaffected, and the particle channels provide clear pathways for fine particles to migrate, resulting in a high mass migration rate. When the fine particle content increases to 10% (Figure IV .17(b)), the skeleton is still primarily composed of coarse particles. Local blockages occur due to the higher fine particle fraction, but connected migration paths are still maintained, leading to a reduced mass migration rate compared to the 5% case. As shown in Figure IV .17(c), at 15% fine particle content, the soil structure is significantly altered, with fine particles contributing to the skeleton and more areas experiencing blockages. Under these conditions, the mass migration rate is

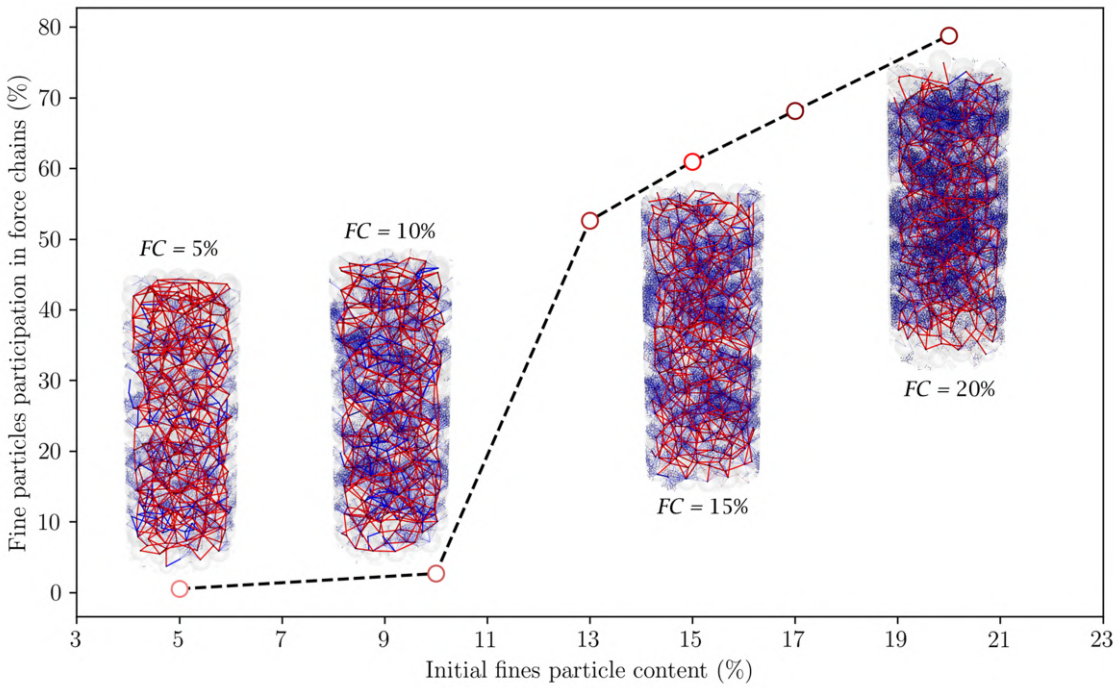

Figure IV .16: Participation of fine particles in force chains at varying initial fines contents (FC = 5%, 10%, 15%, and 20%). The solid line shows the proportion of fine particles involved in the contact force network, indicating a distinct transition threshold around FC = 10%. Insets depict the force chain structures, with red lines representing strong force chains and blue lines representing weak ones.

the lowest. When the fine particle content reaches 20% (Figure IV .17(d)), the increasing incorporation of fine particles into the skeleton destabilizes the coarse particle framework. Areas with blockages are prone to localized particle migration, resulting in an increase in mass migration rate.

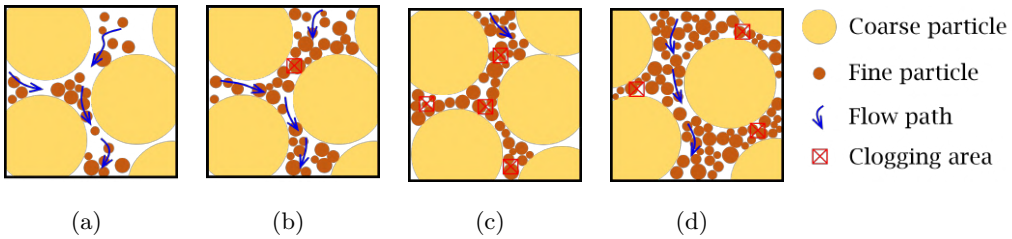

Figure IV .17: Mechanism of fine particle migration under different particle contents: (a) 5%, (b) 10%, (c) 15%, (d) 20%

4 Conclusions

This chapter employed the DEM-DFM method to investigate the impact of various factors on fine particle migration. The feasibility of the model was validated through a comparison between experimental and numerical results. The study primarily analyzed the particle migration process from the perspectives of porosity and mass migration rate, supported by mechanical and microscopic analyses. It focused on the effects of hydraulic gradient and initial porosity, with particular attention to how fine particle content influences mass migration under moderate conditions. The study explored the underlying mechanisms driving different migration rates.

The key findings indicate that hydraulic gradient and porosity exhibit threshold effects on particle migration behavior. For an initial porosity of 0.4, a higher hydraulic gradient leads to an increased mass migration rate, but beyond a threshold of 1.0, the rate stabilizes. For lower porosity, the threshold effect occurs at 2.0, where migration increases with gradient up to this point but is suppressed by particle clogging beyond it. The study also found a porosity threshold of 0.35, below which mass migration decreases with increasing porosity and above which migration intensifies. Additionally, the evolution of porosity during migration is governed first by the rearrangement of coarse particle skeletons and later by fine particle movement. The effect of fine particle content on mass migration rate can reach 30%, with a critical threshold at 10%: below this value, migration decreases as fine particle content increases, while beyond it, fine particles significantly alter the soil structure. Due to computational limitations, further research should explore multi-factor interactions, including pore throat diameter, particle gradation, and dynamic hydraulic gradients, to enhance understanding of fine particle migration mechanisms.

Chapter V

Coupled Effects of Confining Pressure, Fine Particle Content and Material Texture on Suffusion Susceptibility in Gap-Graded Soils

1 Introduction

In the previous chapter, the effects of varying hydraulic gradients, porosity, and fine particle content on soil degradation processes were investigated, revealing the fundamental mechanisms by which these factors influence the stability of granular soils. However, real-world field conditions are significantly more complex. In practical scenarios, levee materials are not only subjected to hydraulic forces but also to mechanical constraints such as confining pressure. Moreover, these materials exhibit diverse structural characteristics, including variations in particle shape, contact stiffness, and gradation structure. These additional factors can substantially alter particle migration and structural evolution, yet their roles in soil susceptibility to degradation remain insufficiently understood.

To build upon the previous findings, this chapter incorporates the influence of confining pressure, fine particle content, and material texture into a unified coupled analysis framework. By employing the hybrid DEM-DFM developed in Chapter 3, we simulate fluid infiltration and particle migration in gap-graded soils under various combinations of mechanical and hydraulic loading conditions. This modeling approach enables detailed analysis of how mechanical confinement and microstructural heterogeneity jointly affect

the particle migrate behavior of granular materials.

2 Model setup and test program

2.1 Numerical model setup for simulating fine particle migration

The simulations were conducted using cylindrical permeability tests under stress-controlled boundary conditions (Figure V .1). The sample was a cylinder with a diameter of 25 mm and a height of 50 mm. The particle size distribution in the fine particle migration simulations is consistent with that used during parameter calibration. The fluid domain matched the size of the DEM model to ensure numerical consistency. The boundary conditions were applied following the experimental method, and the treatment of fluid boundaries was carried out according to the approach proposed by Zhang et al. (2020). As shown in Figure V .1, to ensure geometric continuity and avoid artificial boundary effects, a virtual particle was inserted at the tetrahedral nodes located on the outer boundary, thereby simplifying the boundary treatment.

In the simulations of fine particle migration within the soil sample, the hydraulic gradient is generated by applying distinct fluid pressures at the inlet and outlet, while the lateral boundaries are treated as impermeable. The hydraulic gradient is calculated from the equivalent pressure difference as $i = \frac{\Delta h}{L} = \frac{\Delta P}{gL}$, where Δh is the pressure difference across the sample, L is the sample height, ΔP is the applied dynamic pressure difference between the inlet and outlet boundaries, and g is the acceleration due to gravity. A high hydraulic gradient ($i = 10.0$) was selected based on prior research (Chen et al., 2021a;

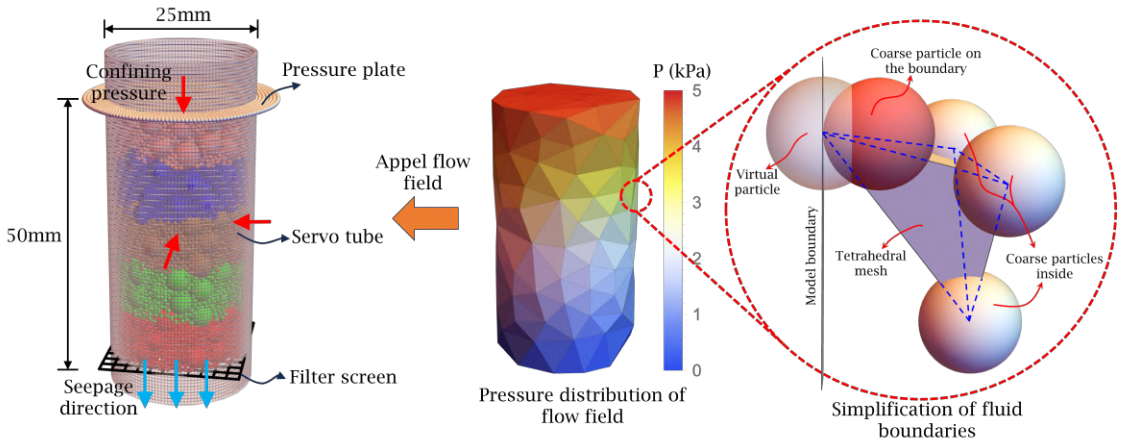

Figure V .1: Coupled DFM-DEM model for simulating fine particle migration

Zhao et al., 2025).

For the DEM boundaries, they essentially consist of clusters of particles. The stress boundary conditions of the sample are achieved by applying body forces to the boundary particles. In previous experimental studies (Fleshman and Rice, 2014), the container walls were typically lined with a layer of fine particles consistent with the test material. Therefore, in our simulations, the material properties of the boundary particles are set to be similar to those of the sample particles. During the application of stress, the bottom of the sample is confined by a fully enclosed lower pressure plate, which is fixed in both vertical and horizontal directions. To allow the eroded particles to escape from the sample, a series of evenly spaced holes, each sized 2.5 mm × 2.5 mm (three times the diameter of the fine particles), are set on the lower pressure plate before applying the hydraulic gradient simulation.

2.2 Model parameters and validation

2.2.1 Mechanical parameters and validation

To simulate the fine particle migration behavior of granular materials with varying textures, a series of laboratory tests were conducted on quartz sand to determine key mechanical parameters under drained conditions, including the internal friction angle, cohesion, and elastic modulus. Quartz sand was selected due to its high hardness and low compressibility, making it a suitable representative of hard-textured granular materials.

As shown by the black dotted line in Figure V .2, the sand was oven-dried and sieved to match a target gradation curve commonly used in previous studies (Ren et al., 2024). Cylindrical samples (20 mm diameter, 40 mm height) were prepared using a layered tamping method to ensure uniformity and consistent relative density. Triaxial compression tests were carried out under consolidated drained conditions at a constant strain rate of 0.1%/min to measure the stress-strain behavior of the material.

The numerical model was developed based on the same gradation curve used in the experiments, with simplifications made to reduce computational cost (as shown in Figure V .2). According to the Kézdi method (Kézdi, 2016) and the criteria proposed by Kenney and Lau Kenney and Lau (1985), a low gap ratio ($D_c/d_m = 4$) was adopted, and particles smaller than 1 mm were uniformly replaced with 0.8 mm particles in the simulation.

Displacement-controlled loading was applied in the DEM model, consistent with experimental procedures. The mechanical parameters were calibrated through iterative comparison with triaxial test results. The final parameter set provided a reasonable match between the experimental and numerical stress–strain behavior under different confining

pressures, supporting the model's applicability for simulating the mechanical response of hard granular materials. These calibrated parameters, along with the hydraulic properties, are used in the subsequent fine particle migration simulations.

2.2.2 Parameter identifications

This study investigates the influence of fine particle migration on fill materials with different textures. The previously validated material parameters are used to represent hard granular materials. For soft particle materials, due to the lack of direct experimental data, parameter values from Liu et al. (2023a) were referenced. These parameters were applicable to particles with sizes similar to those in this study. Elastic modulus, a critical parameter reflecting particle texture, was consistent with Liu et al. (2023a) and suitable for the particle size distribution considered here. The particle size distribution of soft materials mirrored that of hard materials, including fine particles (d_f = 0.8 mm) and coarse particles (d_c = 4-5 mm). All particle sizes fell within the range tested in the triaxial experiments (diameter = 25 mm, height = 50 mm).

The dynamic viscosity of the fluid was 1×10^{-3} Pa·s, suitable for simulating materials with varying textures. For numerical stability between the DFM and DEM domains, the time step of the DEM domain was determined using the method proposed by Liu (2021a):

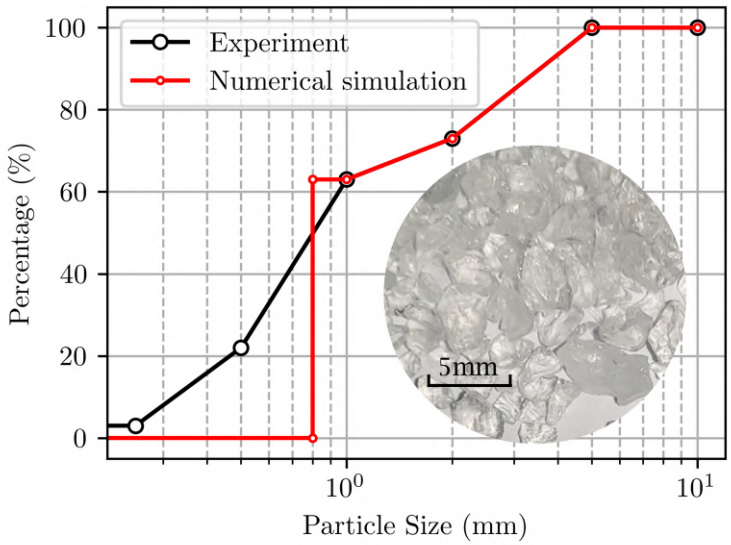

Figure V .2: Grading curves from experiments and numerical simulations for the calibration of mechanical parameters

$$T = 2\pi\sqrt{\frac{m}{k - \eta^2/(4m)}} \tag{V .1}$$

where T is the period of simple harmonic motion for a spring oscillator, k is the stiffness of the spring, and η is the optimal damping coefficient: $\eta = \frac{d}{V^{1/3}}\sqrt{8mk}$. The damping coefficient in the simulation of hydraulic conditions is set to 1% of the optimal damping. Here, d is the diameter of the unit, and V is the volume of the model.

For this study, the particle motion time step (Δt) was set to 2×10^{-7} s, and the fluid time step (Δt^f) was 2×10^{-5} s. The fluid mesh was updated every 100 particle movements. The particle and fluid properties, along with simulation parameters such as elastic modulus, particle size distribution, confining pressure, fine particle content, and hydraulic gradient, are detailed in Table V .1. These parameters ensure that the simulation results accurately reflect the mechanical and hydraulic behaviors of both hard and soft particle materials.

Table V .1: Summary of model parameters

Physical model	Sample dimension $D \times H$ (mm)	25×50	
		Hard particle	Soft particle
Fluid	Fluid viscosity, μ (Pa·s)	1×10^{-3}	1×10^{-3}
	Timestep, Δt (s)	2×10^{-7}	2×10^{-7}
Particle	Elastic modulus, E (GPa)	5	3×10^{-2}
	Poisson's ratio, ν	0.1	0.15
	Compressive strength, C_u (MPa)	20	1×10^{-3}
	Tensile strength (MPa)	0	0
	Friction coefficient, μ_i	0.9	0.6
	Density, ρ (kg/m^3)	2600	2600
	Timestep, Δt^f (s)	2×10^{-5}	2×10^{-5}

2.3 Simulation scenarios

To investigate the critical conditions of particle migration under varying confining pressures (p'), fine particle contents (FC), and material textures, seven scenarios were designed for two types of fill materials. For the hard granular material with validated

mechanical parameters, four levels of fine particle content (15%, 20%, 25%, and 30%) were considered under a confining pressure of 100 kPa. The corresponding particle size distributions are shown in Figure V .3. Previous studies have identified a critical state at which the mass migration rate begins to change significantly when the fine content reaches approximately 25%. Therefore, for the hard fill material, additional scenarios were simulated with a fine content of 25% under typical confining pressures commonly observed in embankments: 25, 50, and 100 kPa.

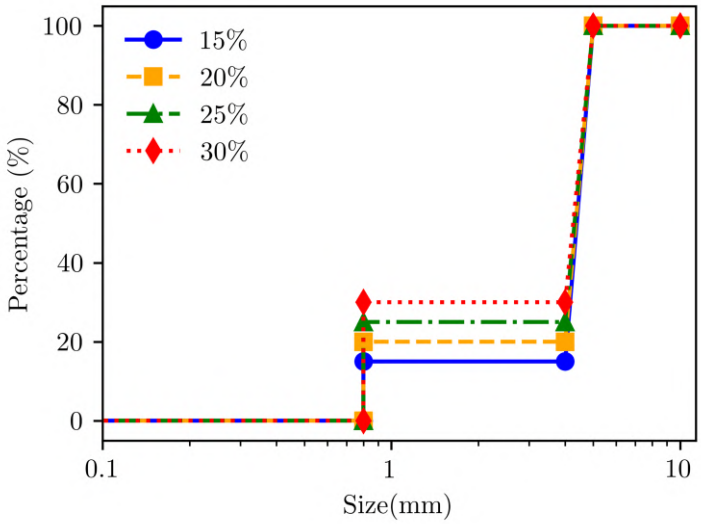

Figure V .3: The particle size distribution of the two gap-graded samples used in the simulations

To explore the influence of material texture, simulations for both hard and soft fill materials were conducted under a confining pressure of 100 kPa and a fine content of 25%, reflecting the significant porosity changes that occur during consolidation. A summary of the simulation procedures and scenarios is provided in Table V .2.

3 Results and discussions

3.1 Effect of confining pressure

The cumulative migrated fine mass (m_m), defined as the ratio of the migrated fine particle mass to the initial total sample mass, serves as a key indicator of soil particle mobility and internal instability. Figure V .4 shows the evolution of cumulative fine particle migration over time under three confining pressures: 25 kPa, 50 kPa, and 100 kPa. The process can be divided into two distinct stages. During the initial migration stage (0–0.05

Table V .2: Details of different work conditions in the numerical investigation

Sample name	Confining pressure p' (kPa)	Fines content FC (%)	Texture	Void ratio n_0	Particles number
C025-FC25-1	25	25	Hard	0.399	13966
C050-FC25-1	50	25	Hard	0.398	13966
C100-FC25-1	100	25	Hard	0.396	13966
C100-FC15-1	100	15	Hard	0.398	8504
C100-FC20-1	100	20	Hard	0.396	11236
C100-FC30-1	100	30	Hard	0.396	16701
C100-FC25-2	100	25	Soft	0.369	13966

s), fine particles near the outlet are rapidly displaced by seepage forces, leading to a sharp rise in cumulative migration. As the number of mobile fine particles decreases, the system enters a quasi-stable phase where the migration rate slows and eventually stabilizes. This

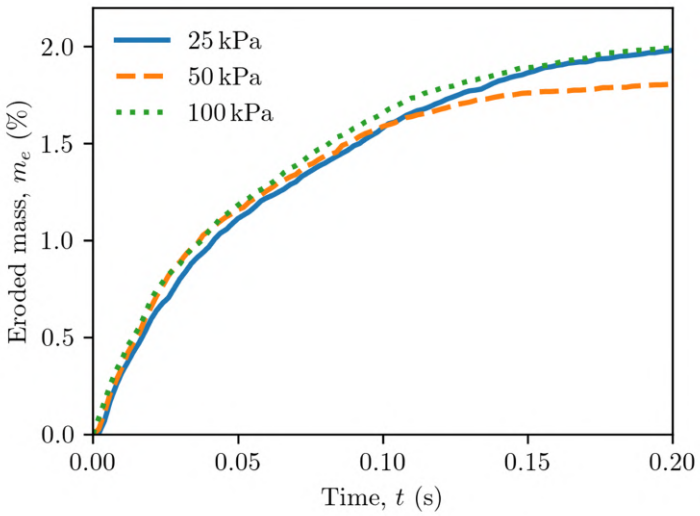

Figure V .4: Cumulative fine particle loss percentage under different confining pressures

stabilization occurs because the remaining fines become trapped within the coarse skeleton pores, and the seepage forces are insufficient to further mobilize them.

The influence of confining pressure (p') on fine mass migration displays a non-linear pattern. At low pressure ($p' = 25$ kPa), weak interparticle contacts allow fines to migrate easily, resulting in pronounced mass loss. Similarly, Zhang et al. (2023a) reported that in the early stage of fine migration, particle motion is primarily governed by fluid pressure and gravity, with limited confinement sensitivity. At moderate pressure ($p' = 50$ kPa), fines contribute to forming a stable load-bearing skeleton, reducing their mobility and lowering cumulative migration—approximately 10% less than at low or high p'. In later stages, increased confinement enhances interparticle friction and restricts migration. However, at high confinement ($p' = 100$ kPa), excessive compaction can expel fine particles from the matrix, leading to renewed migration. Liu et al. (2020) observed a similar trend in fine-rich soils, where high confinement disrupted force chain stability and promoted fine movement. These findings indicate a dual role of confining pressure: moderate confinement suppresses particle migration, while excessively low or high confinement promotes it.

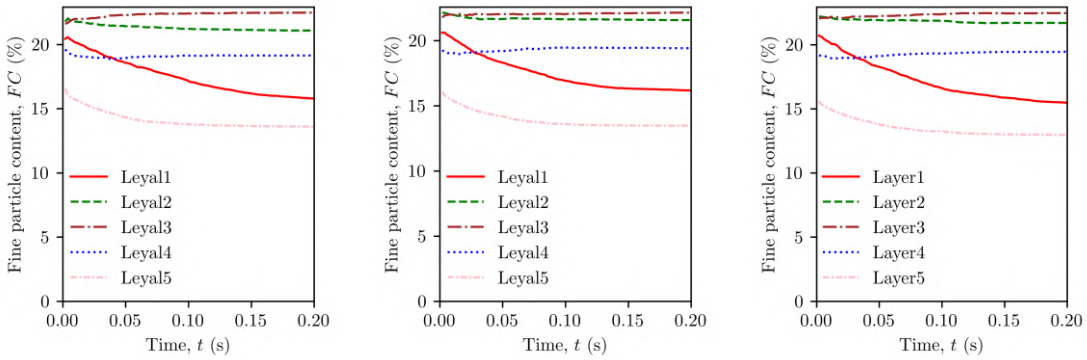

(a) C025-FC25-1 (b) C050-FC25-1 (c) C100-FC25-1

Figure V .5: Variation of the content of fine particles in each layer with time: (a) C025-FC25-1 ($p' = 25$kPa); (b) C050-FC25-1 ($p' = 50$kPa); (c) C100-FC25-1 ($p' = 100$kPa)

Previous studies have demonstrated that fine particle migration during seepage-induced instability is spatially heterogeneous. To explore the mechanisms governing pressure-dependent mass migration, each sample was evenly divided into five layers from bottom to top (each corresponding to one-fifth of the post-consolidation sample height), labeled Layer 1 through Layer 5 (Figure V .3). The proportion of fine particles in each layer relative to the total fine content was then calculated. Owing to volume deformation induced by confining and hydraulic pressures, the uppermost layer (Layer 5) generally exhibited

the lowest fine particle content.

As shown in Figure V .5, most fine particle migration and loss occurred in Layers 1 and 5. Layer 5 primarily underwent outflow, as it had no incoming supply of fines. In contrast, Layer 1, although receiving fines from upper layers, lost more particles than it gained, making it the dominant contributor to total mass loss. Layers 2 through 4 displayed near-equilibrium behavior, with inflow and outflow of fines largely balancing. Post-migration analysis revealed that Layer 5 consistently experienced a deficit of fine particles, indicating that fines embedded within the skeleton structure were difficult to mobilize or replace, thereby limiting structural stabilization.

To further elucidate the above findings, the temporal evolution of fine particle content in Layer 1 under different confining pressures was analyzed. As shown in Figure V .6, the fine particle content in Layer 1 decreases continuously over time under all three confining pressures, confirming that this outlet-adjacent layer plays a dominant role in fine mass migration. Notably, the migration behavior varies markedly with confining pressure. At low pressure ($p' = 25$ kPa), weak interparticle contacts facilitate continuous displacement of fines. At moderate pressure ($p' = 50$ kPa), the rate of decrease slows, indicating enhanced structural interlocking and a more stable particle skeleton that limits mass migration. However, at high pressure ($p' = 100$ kPa), fine mass migration accelerates sharply, likely due to overcompaction that disrupts force chains and mobilizes fines from the soil matrix. These results reaffirm the dual influence of confining pressure on particle

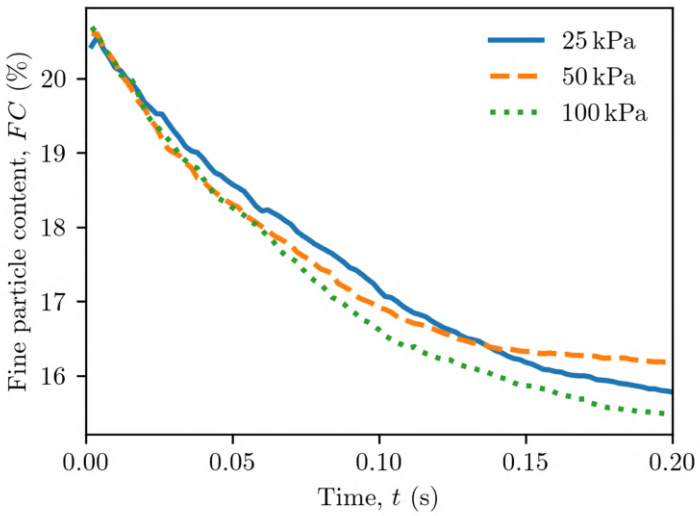

Figure V .6: The variation in fine particle content in Layer 1 under different confining pressures

migration.

By examining fine particle redistribution among the layers, the variation of fine content in Layer 1 was identified as the key factor driving differences in mass migration across confining pressures. This finding is consistent with Wang et al. (2023a). To further validate this, particle distributions in Layer 1 before and after the migration test were compared (Figure V .7). At $p' = 50$ kPa, although the overall fine content decreased relative to the pre-filling state, local clogging was observed in several pores (Figure V .8(b)). In contrast, such clogging was absent at $p' = 25$ kPa and $p' = 100$ kPa (Figures V .8(a) and V .7(c)). To clarify why clogging was most pronounced at $p' = 50$ kPa, representative pores (highlighted in green in Figure V .7) were examined. Before testing, the pore structures were comparable across all samples despite differences in confinement. After the migration process, substantial pore-structure variations emerged, demonstrating the strong hydro-mechanical coupling effect of confining pressure on fine particle migration.

The underlying mechanism of confining pressure influence can also be explored through inter-particle contact forces during fine particle migration. According to previous studies, contact forces are classified as strong or weak. Strong contacts have normal forces exceeding the average, while weak contacts are below the average (Radjai et al., 1999). These contacts are further categorized by particle types: coarse–coarse (C–C), coarse–fine (C–F), and fine–fine (F–F) (Gong et al., 2019). Thornton and Antony (1998) demonstrated that strong contacts primarily bear deviatoric stress, while weak contacts contribute more to mean stress. Figure V .8 presents the post-migration contact force networks for different confining pressures, including all contacts and strong contacts. Thick lines represent C–C contacts, and thin lines represent C–F or F–F contacts. Note that due to the high number of C–F and F–F interactions, many fine-related contacts satisfy the criteria for strong contacts.

It is evident that under 50 kPa, strong contact chains are less prevalent near the outlet zone compared to other pressures, indicating that most fine particle migration occurs in the lower part of the sample. At low pressure ($p' = 25$ kPa), inter-particle contacts are loose, allowing fluid flow to readily disturb the structure and form unstable strong chains that break easily, resulting in extensive fine particle migration. At moderate pressure ($p' = 50$ kPa), particles form a uniform and stable structure under favorable drained conditions. Although the number of strong contacts decreases, their distribution is more uniform, with no high-stress concentration zones, leading to reduced fine particle migration. Under high pressure ($p' = 100$ kPa), the system is overly compacted, causing force chains to concentrate and generate local stress peaks. These stress zones can expel fine particles

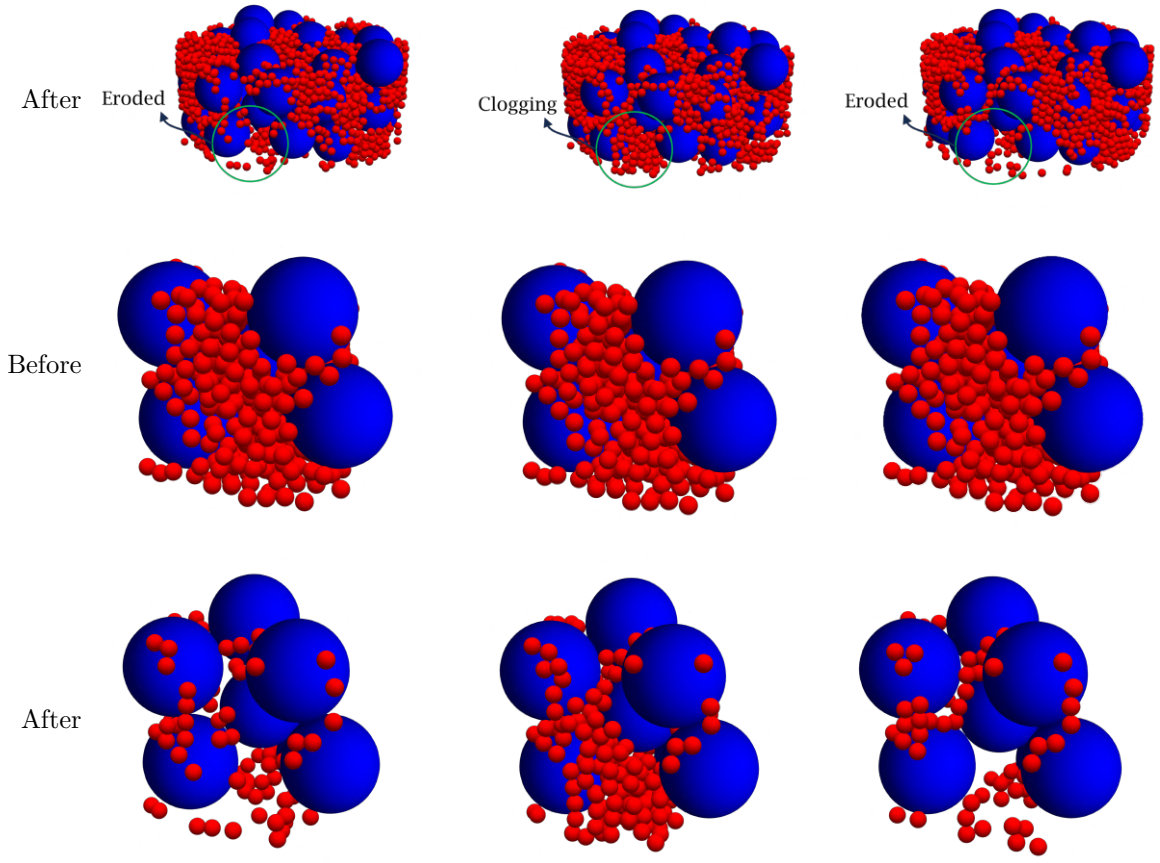

(a) C025-FC25-1 (b) C050-FC25-1 (c) C100-FC25-1

Figure V .7: Variability of particle migration in Layer 1 of different confining pressure: (a) C025-FC25-1 (p' = 25kPa); (b) C050-FC25-1 (p' = 50kPa); (c) C100-FC25-1 (p' = 100kPa)

from the skeleton, creating flow paths and enhancing fine particle migration.

3.2 Effect of initial fine particle content

Fine particle content is also a key factor influencing fine particle migration. As shown in Figure V .9, the temporal evolution of migration mass is strongly affected by the initial fine content (FC). When FC = 15%, the migration rate is relatively low and quickly stabilizes, indicating that the particle skeleton is robust and resists fine particle movement. As FC increases to 20% and 25%, the migration mass rises significantly, suggesting enhanced mobility of fine particles, formation of preferential migration channels, and more pronounced particle redistribution. Notably, when FC reaches 30%, although

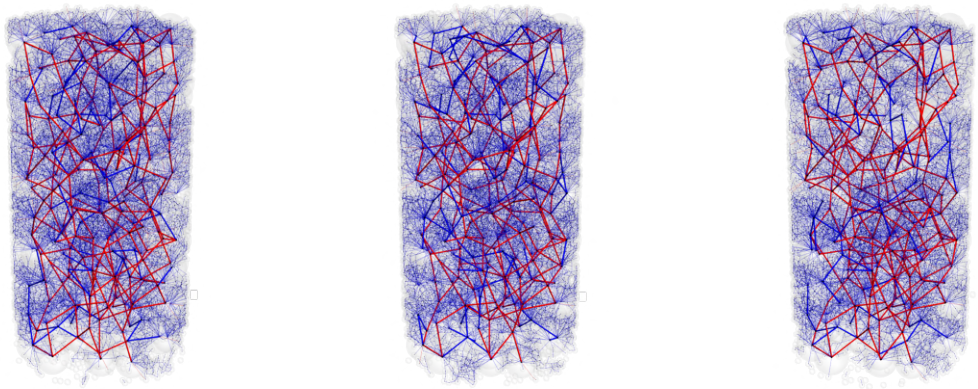

C025-FC25-1 C050-FC25-1 C100-FC25-1

(a) All contacts

C025-FC25-1 C050-FC25-1 C100-FC25-1

(b) Strong contacts only

Figure V .8: Particle distribution before and after fine particle migration in representative pores: (a) all contacts; (b) strong contacts only

the total migrated mass remains high, the migration rate becomes lower than that of FC = 25% after approximately 0.08 seconds. This behavior may be attributed to clogging or self-filtration effects caused by excessive fine particles within the pores, which restrict further particle loss.

To clarify this threshold behavior, a quadratic fit was performed on the final migrated mass versus FC (see Figure V .10). The fitted curve reveals a distinct extremum at around $FC \approx 26.5\%$, corresponding to the maximum fine particle migration. This parabolic trend confirms the presence of a nonlinear relationship between fine content and the intensity of particle movement. Specifically, when the fine content is too low, the skeleton is stable and

particle migration is limited; when it reaches a critical range (near 25–27%), migration is maximized. Beyond this point, excessive fines can accumulate and block pore pathways, leading to reduced migration. These findings strongly support the existence of a critical threshold effect, consistent with previous studies such as Li et al. (2020) and Minh et al. (2014), which have reported similar migration-suppressing phenomena under high-fine-

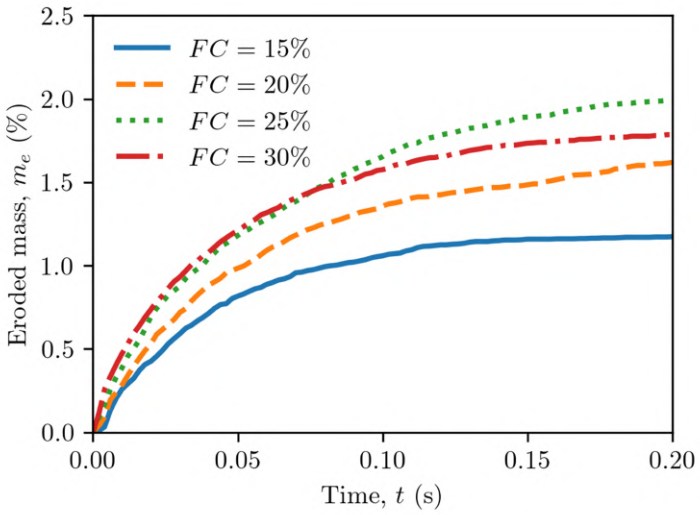

Figure V .9: Cumulative fine particle loss percentage under different initial fine particle content

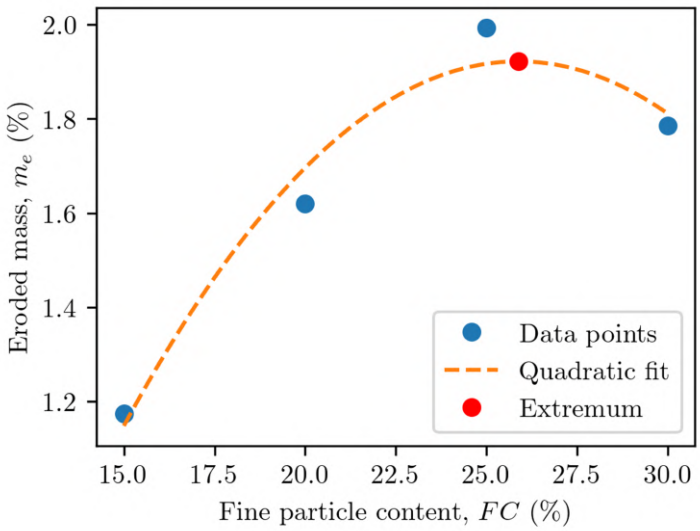

Figure V .10: Quadratic relationship between fine particle content and the final migrated mass, highlighting an optimal FC range for maximum fine particle movement

content conditions.

Fine particle loss induces notable changes in soil structure, directly influencing its mechanical and hydraulic properties. Figure V .11 presents the evolution of volumetric strain (ε_v) over time, revealing the influence of fine content on structural rearrangement and further explaining the particle migration trends observed in Figure V .9. Overall, volumetric strain increases significantly with rising FC, indicating that the soil structure experiences noticeable loosening or expansion. At $FC = 15\%$, the volumetric strain is the lowest (around 1%), reflecting a stable skeleton with minimal fine particle migration. As FC rises to 25%, both volumetric strain and migrated mass increase concurrently, suggesting that greater structural deformation facilitates the movement of fine particles and activates particle migration. Interestingly, although $FC = 30\%$ yields the highest volumetric strain (close to 6%), the migrated mass is lower than at $FC = 25\%$. This suggests that an excessive fine content initially loosens the structure and promotes channel formation, but the subsequent clogging effect hinders further particle migration. These findings indicate that fine particle migration is jointly regulated by particle mobility and the evolution of the granular structure.

Figure V .12 displays the distribution of particle contact types within strong and weak contacts before and after particle migration, under different fine contents. The variation in contact types is primarily observed in the strong contacts, which represent the main load-bearing pathways in the granular system. Prior to particle migration, as FC increases from 15% to 25%, the proportion of strong contacts between coarse

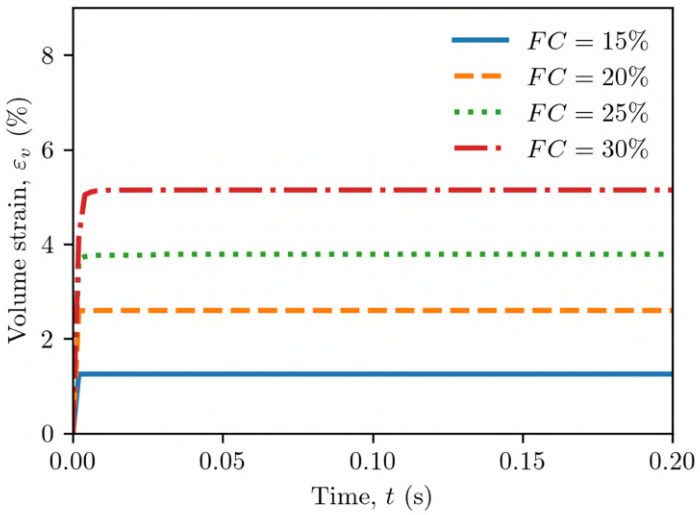

Figure V .11: Volumetric strain under different initial fine particle contents

particles (C–C) decreases significantly, while those involving fine particles (C–F and F–F) increase. Notably, at FC = 30%, the proportion of C–C contacts exceeds that at FC = 25%, indicating that at 25% FC, fine particles are more effectively embedded within the skeleton and participate in load-bearing. After particle migration, the proportion of C–F contacts increases substantially, reflecting the redistribution of fine particles under seepage, which refill the voids between coarse grains. Although this redistribution increases the total number of contacts, the newly formed C–F contacts contribute less to mechanical strength and disrupt the previously dominant C–C contact chains, thereby reducing overall structural stability. This transition is particularly evident when FC is in the range of 25%–30%, where the structure becomes increasingly fine-dominated, significantly elevating the risk of particle migration.

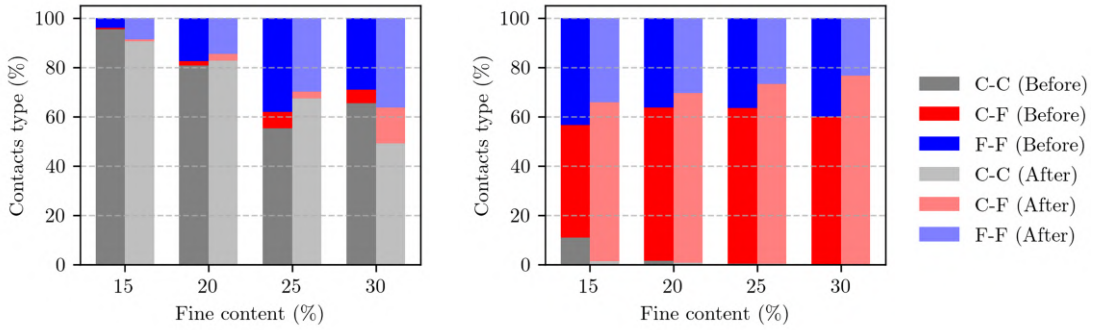

(a) Strong contacts (b) Weak contacts

Figure V .12: Particle distribution before and after fine particle migration in representative pores: (a) all contacts; (b) strong contacts only

Figure V .12 illustrates the distribution of weak contact types for varying fine particle contents. The results show that C–F contacts consistently dominate the weak contact network. Additionally, the proportion of F–F contacts increases with higher FC, indicating that under high fine content, the structure contains a large number of loose C–F and F–F contacts, lacking a stable skeleton. The fine particle migration process further promotes detachment and rearrangement of particles, increasing the proportion of weak contacts, particularly C–F and F–F. In contrast, C–C weak contacts remain minimal, suggesting that coarse particles primarily engage in strong contacts, forming the main load-bearing skeleton. Overall, an increase in fine content weakens the structural integrity of the system, making it more susceptible to particle migration under seepage.

3.3 Effect of texture

The texture of fill materials is a critical factor influencing their susceptibility to fine particle migration. This study compares the migration responses of two fill materials with different textures. As illustrated in Figure V .13, particle texture has a significant impact on the evolution of particle movement. Compared to hard-textured materials, soft-textured fills exhibited faster and more pronounced particle migration within a shorter time frame. This is primarily due to the higher deformability and mobility of soft particles, which leads to a looser granular skeleton and facilitates the detachment and transport of fine particles under seepage forces. Additionally, under confining pressure, soft materials undergo more substantial initial compaction, resulting in a higher concentration of fine particles per unit volume, which increases the likelihood of pore channel formation and particle migration.

In contrast, hard-textured materials exhibit stronger interparticle interlocking and more stable structures, maintaining a robust force-chain network formed by strong contacts. This structural stability resists seepage-induced disturbances and slows the progression of migration.

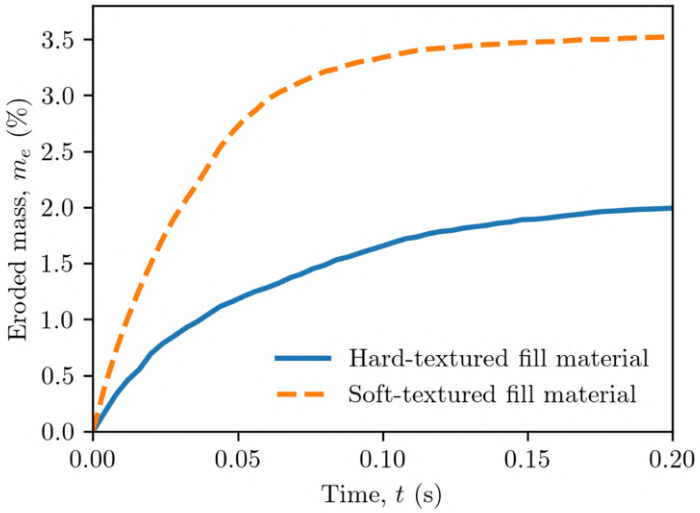

Figure V .13: Cumulative fine particle loss percentage under different texture in embankments fill materials

Once the granular structure is established, the stress transmission characteristics differ significantly between textures. To explore the evolution of anisotropy, we analyzed the orientation distribution of normal contact forces in both material types (Figure V .14(a)). In hard materials, increasing confining pressure amplifies the initial anisotropy. While local

structural degradation may occur due to the loss of fine particles, the overall structure remains stable under pressure, preserving the continuity of the force chains. Strong contact forces inhibit fine particle migration, maintaining a relatively stable stress distribution and enhancing anisotropy after fine particle migration.

In contrast, soft materials exhibit a clear reduction in anisotropy following fine particle migration (Figure V .14(b)). The weak interparticle contact forces allow fine particles to migrate and rearrange easily, loosening the structure and promoting homogenization. The strengthening effect of confining pressure is limited in this case, and significant relative particle displacements disrupt the initial anisotropic configuration. With ongoing fine particle loss, increased porosity, and particle rearrangement, the mechanical response of soft materials tends toward isotropy, weakening their overall structural stability. This vulnerability is particularly critical in levees or earth structures composed primarily of soft soils, where seepage can induce large-scale instability or even failure.

From a macroscopic perspective, confining pressure plays a dual role: it influences both material stability and anisotropy. In hard-textured materials, higher confining pressure enhances interparticle contact forces, promoting directional force chains that improve both anisotropy and structural resistance to disturbance. In soft materials, however, the inherently weak contact forces limit the structural benefits of increased pressure, failing to suppress fine particle migration or pore expansion. As a result, even at higher confining pressures, anisotropy is difficult to maintain.

To further explore the underlying mechanisms of structural instability during fine particle migration, we conducted strain energy analysis for the two samples (C100-FC25-1: hard-textured; C100-FC25-2: soft-textured). The strain energy at each contact consists of a normal component (E_{sn}) and a tangential component (E_{st}), calculated as follows (Hanley et al., 2018; Wang and Arson, 2018):

$$E_{sn} = \frac{2}{5} |F_n| \, s \tag{V .2}$$

$$E_{st} = E_{st}^{\beta-1} + \frac{\left|F_t^{\beta-1} + F_t^{\beta}\right|}{2} \frac{\left|F_t^{\beta} - F_t^{\beta-1}\right|}{k_t} \tag{V .3}$$

where F_n and s are the normal force and overlap between particles, respectively. $E_{st}^{\beta-1}$ is the tangential component of the strain energy at the previous timestep $\beta - 1$, F_t^{β} and $F_t^{\beta-1}$ are the tangential forces at the current and previous timesteps, and k_t is the tangential stiffness.

As shown in Figure V .15, we focused on the evolution of strain energy after 5×10^{-3} s,

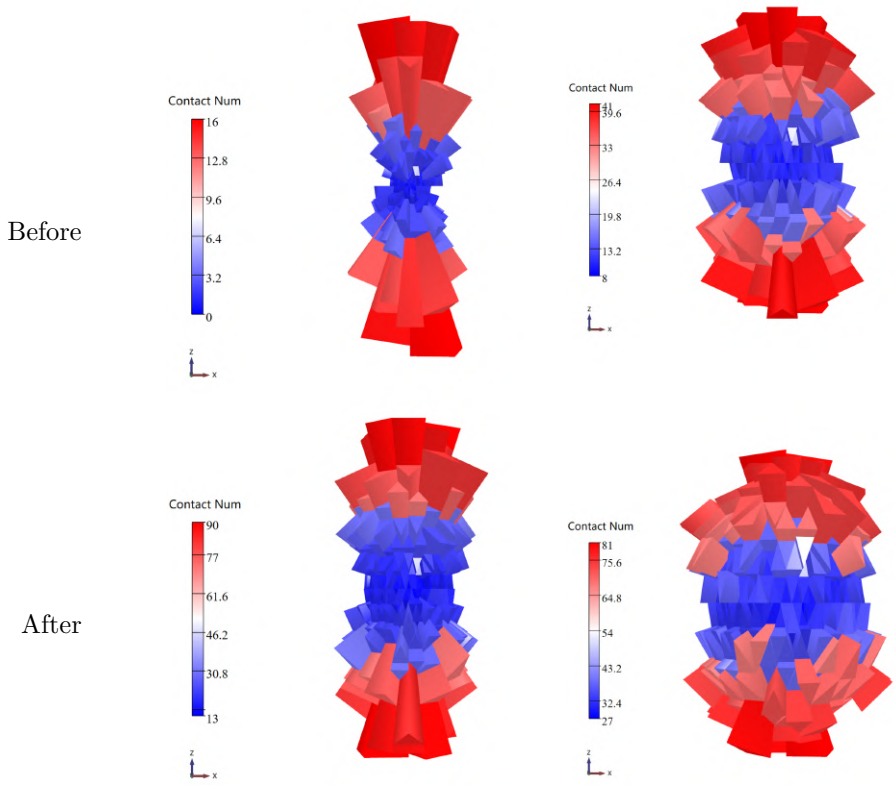

(a) C100-FC25-1 (b) C100-FC25-2

Figure V .14: Orientation distribution of normal contact forces before and after fine particle migration in fill material samples with different textures: (a) C100-FC25-1 (Hard-filler material); (b) C100-FC25-2 (Soft-filler material)

as the initial filling phase is dominated by volumetric deformation, which masks the subsequent structural response. In the early stages, due to particle migration and rearrangement, both samples exhibited a rapid drop in total strain energy. For the hard-textured sample (C100-FC25-1), the strain energy remained at a relatively low level overall, with a noticeable energy drop around 0.022 seconds, indicating a sudden structural adjustment and energy release.

In contrast, the soft-textured sample (C100-FC25-2) maintained a higher level of strain energy without distinct drops, suggesting a greater capacity for energy storage during continuous deformation. This energy was primarily dissipated through localized fine particle migration, allowing the structure to remain in a relatively stable state.

Hard-textured materials are more prone to global structural instability but can achieve partial stability through energy release and structural readjustment. Soft-textured materi-

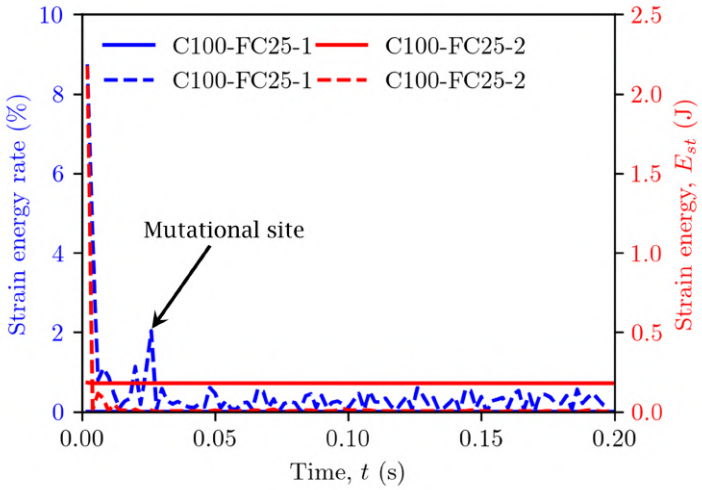

Figure V .15: Typical strain energy and strain energy change rate in two texture samples

als, on the other hand, possess a greater energy storage capacity and better local stability, yet are more susceptible to structural loosening and homogenization under seepage conditions, ultimately compromising their load-bearing capacity. These findings highlight the importance of considering material texture, confining pressure, and fine particle content when selecting fill materials for levee construction to enhance structural resilience and resistance to fine particle migration.

In this study, we summarize the failure modes of two textured filler materials, as depicted in Figure V .16. The failure of hard-textured materials during fine particle migration is primarily governed by their ability to release strain energy efficiently. Due to the high rigidity and friction between particles, the coarse particle skeleton undergoes structural adjustments early in the process, redistributing contact forces and achieving a more stable configuration. These adjustments result in a rapid dissipation of stored strain energy, preventing significant particle migration or localized instabilities. Consequently, the overall skeleton integrity is maintained, and the material stabilizes as the structure evolves to accommodate the applied stresses.

In soft-textured materials, failure is primarily localized and driven by fine particle migration. During fine particle migration, fine particles are mobilized and transported, leading to a reduction in coarse particle contacts and the formation of weak force chains in areas of particle loss. This process disrupts the load-bearing skeleton, particularly in the bottom layers, where the concentration of migrating fine particles creates flow paths and local instabilities. Unlike hard-textured materials, soft-textured materials exhibit limited

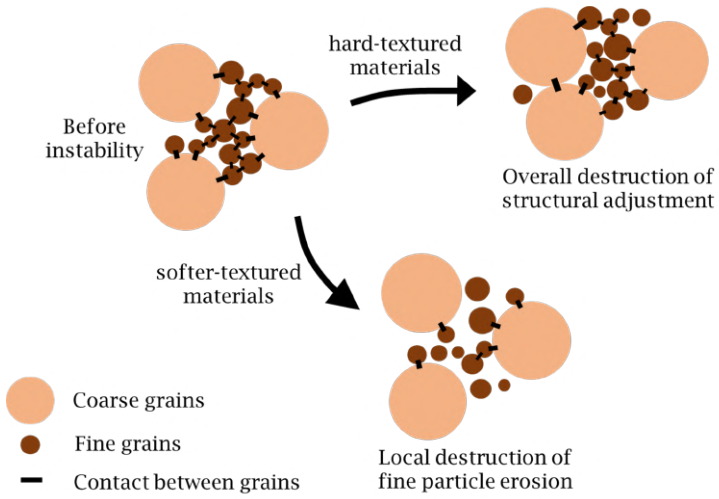

Figure V .16: The failure modes of two textured filler materials

structural adjustments and retain higher strain energy, resulting in prolonged instability in affected regions.

4 Conclusions

This chapter employed a coupled DEM–DFM simulation approach to investigate the combined effects of confining pressure (p'), initial fine particle content (FC), and material texture on the susceptibility of gap-graded soils to fine particle migration. The model effectively captured the macro- and micro-mechanical responses of soils and highlighted how different physical parameters govern particle migration behavior.

The results reveal that confining pressure regulates fine particle migration by shaping contact force chains and pore structures: moderate pressure (50 kPa) promotes stable configurations that resist particle loss, whereas low pressure induces looseness and high pressure causes stress concentration, both facilitating particle migration. Fine particle content exhibits a threshold effect: moderate levels enhance migration by increasing particle mobility, while excessive fines ($FC > 27\%$) cause clogging, reduce migration, and weaken structural integrity by disrupting coarse–coarse contacts. Material texture also plays a critical role: hard-textured fills maintain contact networks and resist deformation, improving stability; in contrast, soft-textured materials deform easily and are more prone to localized particle migration under seepage.

Despite these insights, two main limitations remain. First, the simulation uses idealized conditions and does not account for real-world factors such as irregular particle

shapes. Second, chemical interactions between particles, which may influence migration behavior, are not considered. Future studies should incorporate these aspects to improve the model's realism and provide a more comprehensive understanding of fine particle migration mechanisms in granular soils.

Chapter VI

Conclusions and perspectives

1 Conclusions

This study explored the fine particle migration behavior of granular materials under seepage flow, combining laboratory experiments with multi-scale numerical simulations. Key factors such as hydraulic gradient, particle gradation, porosity, fine particle content, confining pressure, and material texture were systematically examined. The main conclusions and perspectives are summarized below.

- A series of seepage experiments were conducted using a self-developed rigid cylindrical apparatus with transparent quartz sand to examine the influence of physical parameters on fine particle migration. Results show that mass migration rates are most sensitive to the hydraulic gradient, followed by the coefficient of uniformity and porosity. Higher uniformity and porosity facilitate more active particle movement and enhanced erosion. A distinct transition point was observed in the flow process, marking the shift from seepage-induced compaction to active particle migration. Fine particles exhibited stratified migration characteristics. Among commonly used internal stability criteria, the Istonima criterion demonstrated reliable performance, particularly when gradation and porosity were considered jointly.

- A coupled DFM-DEM method was developed and validated to simulate fine particle migration and pore evolution in non-uniform soils. Simulations revealed three stages of particle migration: initiation, deceleration, and stabilization, with dynamic transitions between clogging and particle transport driven by fluid–particle interactions. This method is effective under dynamic fluid mesh (DFM) conditions, offering high stability and accuracy. Limitations remain in estimating porosity for flat pore

geometries and when fine particle sizes are comparable to coarse grains.

- Using the DEM-DFM model, the effects of initial porosity, hydraulic gradient, and fine particle content on migration thresholds were analyzed. Results indicate clear nonlinear threshold behavior, with critical transitions occurring at hydraulic gradients between 1.0 and 2.0, and a porosity threshold near 0.35. A fine particle content threshold of 10% was identified: below this, structural clogging enhances stability, while higher contents destabilize the grain skeleton and intensify particle migration. This study reveals a coupled mechanism of particle transport, porosity restructuring, and erosion evolution across macro- and micro-scales, providing new insights into threshold-driven migration behavior.

- Confining pressure and material texture were introduced as additional factors to evaluate their impact on suffusion susceptibility. Fine particle migration mainly occurred at the initial and final stages of transport and was significantly influenced by interparticle friction and material stiffness. Hard-textured soils, under high confining pressure and near-critical fine content (25–27%), tended to exhibit overall structural collapse. In contrast, soft-textured soils with uneven pore structures displayed more localized instability. Analysis of force chains and strain energy evolution indicated that material texture plays a key role in governing migration pathways and structural resilience.

2 Perspectives

This thesis focuses on the investigation of fine particle migration in granular materials under seepage flow. A series of experimental and numerical procedures have been carried out to identify the key influencing factors and to better understand the mechanisms of fine particle migration and structural instability. In the near future, this research can be extended in the following directions:

- In future work, the experimental approach could be extended to include soil samples with a broader range of particle shapes and more complex material compositions, helping to bridge the gap between laboratory conditions and field environments. The integration of image recognition techniques and particle image velocimetry (PIV) would enable precise, visual tracking of fine particle migration, facilitating detailed and quantitative analysis of particle transport and the associated erosion processes.

- Regarding model development, the DFM-DEM coupling framework could be enhanced by increasing mesh resolution and improving the efficiency of fluid–solid interactions. Incorporating advanced techniques, such as the Lattice Boltzmann Method (LBM), may provide more accurate pore pressure predictions and more effectively capture the migration and redistribution of fine particles within complex pore networks.

- Further research is needed to elucidate the mechanisms controlling migration thresholds. Establishing quantitative relationships between microstructural parameters, such as pore throat size distribution, and critical fine particle migration conditions would enable more reliable predictions of soil instability. In addition, developing erosion stability maps under varying hydraulic and mechanical loading scenarios could facilitate a transition from threshold identification to proactive control and risk mitigation strategies.

- Finally, a deeper understanding of the role of material texture and local structural failure is essential. Future studies should consider incorporating more realistic soil textures and chemical environmental factors, as well as exploring the influence of variable confining pressures and loading paths. These efforts will help improve the prediction of failure mechanisms in real-world geotechnical structures such as levees and slopes and support the development of more robust design guidelines.

References

Abdelhamid, Y. and El Shamy, U. (2016). Pore-Scale Modeling of Fine-Particle Migration in Granular Filters. *International Journal of Geomechanics*, 16(3):04015086.

Ahlinhan, M. F. and Adjovi, C. E. (2019). Combined Geometric Hydraulic Criteria Approach for Piping and Internal Erosion in Cohesionless Soils. *GEOTECHNICAL TESTING JOURNAL*, 42(1):180–193.

Ahmadi, M., Shire, T., Mehdizadeh, A., and Disfani, M. (2020). DEM modelling to assess internal stability of gap-graded assemblies of spherical particles under various relative densities, fine contents and gap ratios. *Computers and Geotechnics*, 126:103710.

American Society of Civil Engineers (1891). Report of the Committee on the Cause of the Failure of the South Fork Dam. *Transactions of the American Society of Civil Engineers*, 24(1):431–461.

Andrianatrehina, L., Souli, H., Rech, J., Taibi, S., Fry, J.-J., Ding, L., and Fleureau, J.-M. (2016). Analysis of the internal stability of coarse granular materials according to various criteria. *European Journal of Environmental and Civil Engineering*, 20(8):936–953.

Bai, S. S., Jin, Q., Zhang, D. S., and Zhou, Z. Q. (2024). Theoretical Formula of the Critical Hydraulic Condition of Suffusion Initiation. *Soil Mechanics and Foundation Engineering*.

Bedja, M., Umar, M., and Kuwano, R. (2022). Influence of density on the post-suffusion behavior of gap-graded sand with fines. *Soils and Foundations*, 62(3):101159.

Beggs, G. E., Enger, M. L., Fogg, R. J., Immerman, H. T., Krynine, D. P., Marston, F. A., Paaswell, G., Proctor, R. R., Terzaghi, C., White, L., Gilboy, G., Hollister, S. C., Knappen, T. T., Harza, L. F., Richardson, E. A., Strohl, R. M., Creager, W. P., Feld, J., Chang, Y. L., Senour, C., Burmister, D. M., Taylor, D. W., Johnson, L. H., Tschebotareff, G. P., Wells, W. L., Streiff, A., Dore, S. M., and Hough, B. K. (1938). Discussion on Application of Soil Mechanics. *Transactions of the American Society of Civil Engineers*, 103(1):1449–1502.

Benamar, A., Correia dos Santos, R. N., Bennabi, A., and Karoui, T. (2019). Suffusion evaluation of coarse-graded soils from Rhine dikes. *Acta Geotechnica*, 14(3):815–823.

Bendahmane, F., Marot, D., and Alexis, A. (2008). Experimental Parametric Study of Suffusion and Backward Erosion. *Journal of Geotechnical and Geoenvironmental Engineering*, 134(1):57–67.

Bi, J., Zhang, H., Luo, X., Shen, H., and Li, Z. (2021). Modeling of internal erosion using particle size as an extra dimension. *Computers and Geotechnics*, 133:104021.

Bonelli, S., Fell, R., and Benahmed, N. (2013). Concentrated Leak Erosion. In *Erosion in Geomechanics Applied to Dams and Levees*, chapter 4, pages 271–341. John Wiley & Sons, Ltd.

Buchanan, S. J. (1938). Closure to "Buchanan on Application of Soil Mechanics". *Transactions of the American Society of Civil Engineers*, 103(1):1449–1502.

Bui, H. H. and Nguyen, G. D. (2017). A coupled fluid-solid SPH approach to modelling flow through deformable porous media. *International Journal of Solids and Structures*, 125:244–264.

Burenkova, VV. (1993). Assessment of suffusion in non-cohesive and graded soils. *Filters in geotechnical and hydraulic engineering*, pages 357–360.

Cao, Z., Sun, W., Xie, Q., Wu, Z., Fu, X., Fumagalli, A., Tian, D., and Liang, L. (2022). Fluid–solid coupled model for the internal erosion of gap-graded soil–rock mixtures with different fines contents: Its verification and application. *Hydrological Processes*, 36(9):e14677.

Cao, Z., Xiao, Z., Cai, Y., and Han, J. (2024). Investigation of Suffusion in Soil with Arching Based on CFD–DEM Simulation. *International Journal of Geomechanics*, 24(3):04024014.

Carman, P. C. (1956). Flow of gases through porous media.

Cavarretta, I., Coop, M., and O'sullivan, C. (2010). The influence of particle characteristics on the behaviour of coarse grained soils. *Géotechnique*, 60(6):413–423.

Chand, R., Khaskheli, M. A., Qadir, A., Ge, B., and Shi, Q. (2012). Discrete particle simulation of radial segregation in horizontally rotating drum: Effects of drum-length and non-rotating end-plates. *Physica A: Statistical Mechanics and its Applications*, 391(20):4590–4596.

Chang, D. and Zhang, L. (2011). A stress-controlled erosion apparatus for studying internal erosion in soils. *Geotechnical Testing Journal*, 34.

Chang, D., Zhang, L., and T.H.Xu (2012). Laboratory Investigation of Initiation and Development of Internal Erosion in Soils under Complex Stress States.

Chang, J., Xu, Y., Xiao, J., Wang, L., and Jiang, J.-Q. (2022). Water–soil chemical mechanism and soil structural stability of expansive soil under the action of acid rain infiltration. *Bulletin of Engineering Geology and the Environment*, 81(10):438.

Chang, K.-T., Lee, K. Z.-Z., and Wu, H.-Y. (2020). Internal erosion failure of uniform sands under confinement and constricted seepage exit. *Water*, 12(9):2417.

Chen, C. and Zhang, L. (2023). Hydro-mechanical behaviour of soil experiencing seepage erosion under cyclic hydraulic gradient. *Géotechnique*, 73(2):115–127.

Chen, C., Zhang, L. M., and Chang, D. S. (2016). Stress-Strain Behavior of Granular Soils Subjected to Internal Erosion. *Journal of Geotechnical and Geoenvironmental Engineering*, 142(12):06016014.

Chen, C., Zhang, P., Zhang, L., Zhang, J., Xue, J., and Lu, H. (2024). Internal erosion in granular soils with different microstructures under cyclically increased hydraulic gradients. *Journal of Hydrology*, 639:131601.

Chen, L., Wan, Y., He, J.-J., Luo, C.-M., Yan, S.-F., and He, X.-F. (2021a). Experimental study on the suffusion mechanism of gap-graded soils under an exceedance hydraulic gradient. *Natural Hazards*, 109(1):405–439.

Chen, S., Li, M., Zhang, F., and Wang, T. (2025). Coupled DFM-DEM-EFCM investigation on the suffusion in gap-graded clayey sands. *Computers and Geotechnics*, 179:107004.

Chen, T., Hu, Z., Yang, Z., and Zhang, Y. (2023). A resolved CFD–DEM investigation into the onset of suffusion: Effect of confining pressure and stress anisotropy. *International Journal for Numerical and Analytical Methods in Geomechanics*, 47(16):3018–3043.

Chen, X., Fang, M., Li, B., Rostami, A., Guo, L., and Cai, Q. (2021b). Experimental study on seepage-induced concentrated leak erosion in sand under triaxial testing conditions. *Arabian Journal of Geosciences*, 15(1):74.

Cheng, K., Zhang, C., Peng, K., Liu, H., and Ahmad, M. (2021). Un-resolved CFD-DEM method: An insight into its limitations in the modelling of suffusion in gap-graded soils. *Powder Technology*, 381:520–538.

Choe, Y., Choi, H., and Won, J. (2024). Suffusion of a sand–clay mixture: Impact of the ionic-concentration gradient, clay type, sand-grain size and hydraulic gradient. *Géotechnique*, 74(10):1004–1018.

Chowdhury, M. U. (1948). The control of seepage under dams on pervious foundations.

Chun, L., Xiaoyu, Z., and Qiang, X. (2017). Energy conservation simulation of three dimensional discrete element model: A case study of landslide. *Chinese Journal of Underground Space and Engineering*, 13(S2):698–704.

Cui, Y., Yin, Y., and Guo, C. (2021). Investigation of Internal Erosion of Wide Grading Loose Soil—A Micromechanics-Based Study. In Arbanas, Z., Bobrowsky, P. T., Konagai, K., Sassa, K., and Takara, K., editors, *Understanding and Reducing Landslide Disaster Risk: Volume 6 Specific Topics in Landslide Science and Applications*, pages 155–161. Springer International Publishing, Cham.

Dai, S., He, X., Tong, C., Gao, F., Zhang, S., and Sheng, D. (2024a). Stability of sandy soils against internal erosion under cyclic loading and quantitatively examination of the composition and origin of eroded particles. *Canadian Geotechnical Journal*, 61(4):732–747.

Dai, S., Zhang, S., Gao, F., He, X., and Sheng, D. (2024b). Investigation of particle segregation in a vertically vibrated binary mixture: Segregation process and mechanism. *Computers and Geotechnics*, 169:106236.

DallaValle, J. M. (1948). Micromeritics: The technology of fine particles.

Dallo, Y. A. (2021). Discussion of "Influence of particle-size distribution homogeneity on shearing of soils subjected to internal erosion". *Canadian Geotechnical Journal*, 58(1):151–153.

Deng, Z., Chen, X., Jin, W., and Wang, G. (2023a). Effect of Gradation Characteristics and Particle Morphology on Internal Erosion of Sandy Gravels: A Large-Scale Experimental Study. *Water*, 15(14):2660.

Deng, Z., Wang, G., and Jin, W. (2023b). Coupling of hydraulic loading and surcharge pressure during suffusion in sandy gravels. *Géotechnique Letters*, 13(1):75–81.

Deng, Z., Wang, G., Jin, W., Tang, N., Ren, H., and Chen, X. (2023c). Characteristics and quantification of fine particle loss in internally unstable sandy gravels induced by seepage flow. *Engineering Geology*, 321:107150.

Department of Jobs, P. a. R. (2024). What is soil? - Agriculture. https://agriculture.vic.gov.au/farm-management/soil/what-is-soil.

Di Felice, R. (1994). The voidage function for fluid-particle interaction systems. *International Journal of Multiphase Flow*, 20(1):153–159.

Divya Jyothi, B. and Ramya Krishna, V. (2021). Optimal arrangement of geogrids in road embankment using different fill materials. *Materials Today: Proceedings*, 46:8507–8512.

El Mountassir, G., Sánchez, M., and Romero, E. (2014). An experimental study on the compaction and collapsible behaviour of a flood defence embankment fill. *Engineering Geology*, 179:132–145.

El Shamy, U., Zeghal, M., Dobry, R., Thevanayagam, S., Elgamal, A., Abdoun, T., Medina, C., Bethapudi, R., and Bennett, V. (2010). Micromechanical aspects of liquefaction-induced lateral spreading. *International Journal of Geomechanics*, 10(5):190–201.

Fall, A., Weber, B., Pakpour, M., Lenoir, N., Shahidzadeh, N., Fiscina, J., Wagner, C., and Bonn, D. (2014). Sliding friction on wet and dry sand. *Physical Review Letters*, 112(17):175502.

Fang, Y., Zhuo, B., Zhang, R., Wang, Y., Dou, L., and Yao, Y. (2024). Soil conditioning of clay based on interface adhesion mechanism: Microscopic simulation and laboratory experiment. *Underground Space*, 18:239–255.

Fell, R., Wan, C. F., Cyganiewicz, J., and Foster, M. (2003). Time for Development of Internal Erosion and Piping in Embankment Dams. *Journal of Geotechnical and Geoenvironmental Engineering*, 129(4):307–314.

Feng, R., Fourtakas, G., Rogers, B. D., and Lombardi, D. (2024). Modelling internal erosion using 2D smoothed particle hydrodynamics (SPH). *Journal of Hydrology*, 639:131558.

Fleshman, M. S. and Rice, J. D. (2014). Laboratory modeling of the mechanisms of piping erosion initiation. *Journal of Geotechnical and Geoenvironmental Engineering*, 140(6):04014017.

Fraser, H. J. (1935). Experimental Study of the Porosity and Permeability of Clastic Sediments. *The Journal of Geology*, 43(8, Part 1):910–1010.

Frishfelds, V., Hellström, J. G. I., Lundström, T. S., and Mattsson, H. (2011). Fluid Flow Induced Internal Erosion within Porous Media: Modelling of the No Erosion Filter Test Experiment. *Transport in Porous Media*, 89(3):441–457.

GB50487-2008 (2008). Code for engineering geological investigation of water resources and hydropower.

Gilboy, G. (1933). Soil Mechanics Research. *Transactions of the American Society of Civil Engineers*, 98(2):218–239.

Gong, J., Liu, J., and Cui, L. (2019). Shear behaviors of granular mixtures of gravel-shaped coarse and spherical fine particles investigated via discrete element method. *Powder Technology*, 353:178–194.

Gong, J., Pang, X., Tang, Y., Yang, Z., Jiang, J., and Ou, X. (2024). Effects of angularity and content of coarse particles on the mechanical behaviour of granular mixtures: A DEM study. *Granular Matter*, 26(1):17.

Gu, D. M., Huang, D., Liu, H. L., Zhang, W. G., and Gao, X. C. (2019). A DEM-based approach for modeling the evolution process of seepage-induced erosion in clayey sand. *Acta Geotechnica*, 14:1629–1641.

Guo, Y., Wang, C., Lu, M., and Yu, X. B. (2023). Numerical investigations on evolution mechanism of contact erosion in layered soils considering particle-scale parameters. *Transportation Geotechnics*, 41:101023.

Hanley, K. J., Huang, X., and O'Sullivan, C. (2018). Energy dissipation in soil samples during drained triaxial shearing. *Géotechnique*, 68(5):421–433.

Harshani, H., Galindo-Torres, S., Scheuermann, A., and Muhlhaus, H. (2015). Micro-mechanical analysis on the onset of erosion in granular materials. *Philosophical Magazine*, 95(28-30):3146–3166.

Hendrickson, BH. (1934). The choking of pore-space in the soil and its relation to runoff and erosion. *Eos, Transactions American Geophysical Union*, 15(2):500–505.

Hicher, P.-Y., Marot, D., and Sibille, L. (2018). Advances in multi-physics and multi-scale couplings in geo-environmental mechanics. In Nicot, F. and Millet, O., editors, *Advances in Multi-Physics and Multi-Scale Couplings in Geo-Environmental Mechanics*, pages 291–334. Elsevier.

Hu, Z., Li, J. Z., Zhang, Y. D., Yang, Z. X., and Liu, J. K. (2023). A CFD–DEM study on the suffusion and shear behaviors of gap-graded soils under stress anisotropy. *Acta Geotechnica*, 18(6):3091–3110.

Hu, Z., Zhang, Y., and Yang, Z. (2019). Suffusion-induced deformation and microstructural change of granular soils: A coupled CFD–DEM study. *Acta Geotechnica*, 14(3):795–814.

Hu, Z., Zhang, Y., and Yang, Z. (2020). Suffusion-Induced Evolution of Mechanical and Microstructural Properties of Gap-Graded Soils Using CFD-DEM. *Journal of Geotechnical and Geoenvironmental Engineering*, 146(5):04020024.

Ibrahim, A. and Meguid, M. (2023). The Applicability of the Two-Fluid Model to Simulate Soil Internal Fluidization Due to Pipe Leakage. In Walbridge, S., Nik-Bakht, M., Ng, K. T. W., Shome, M., Alam, M. S., el Damatty, A., and Lovegrove, G., editors, *Proceedings of the Canadian Society of Civil Engineering Annual Conference 2021*, pages 421–431, Singapore. Springer Nature.

Indraratna, B. and Radampola, S. (2002). Analysis of Critical Hydraulic Gradient for Particle Movement in Filtration. *Journal of Geotechnical and Geoenvironmental Engineering*, 128(4):347–350.

Irons, T., Quinn, M., Li, Y., and McKenna, J. (2014). A numerical assessment of the use of surface nuclear magnetic resonance to monitor internal erosion and piping in earthen embankments. *Near Surface Geophysics*, 12:325–334.

Istomina, VS. (1957). Filtration stability of soils. *Gostroizdat, Moscow, Leningrad*, 15.

Jiang, X., Cui, P., and Ge, Y. (2015). Effects of fines on the strength characteristics of mixtures. *Engineering Geology*, 198:78–86.

Kawano, K., Shire, T., and O'Sullivan, C. (2018). Coupled particle-fluid simulations of the initiation of suffusion. *Soils and Foundations*, 58(4):972–985.

Kay, BD. and Angers, DA. (2001). 7 Soil Structure. *Soil physics companion*, page 249.

Kenney, TC. and Lau, D. (1985). Internal stability of granular filters. *Canadian geotechnical journal*, 22(2):215–225.

Kezdi, A. (1969). Increase of protective capacity of flood control dikes. *Department of Geotechnics, Technical University of Budapest, Report*, (1).

Kézdi, A. (2016). *Stabilized Earth Roads*. Elsevier.

Knappen, T. T. and Philippe, R. R. (1936). Practical Soil Mechanics at Muskingum—IV.

Knight, C. (2018). *Fluid Flow and Drag in Polydisperse Granular Materials Subject to Laminar Seepage Flow*. PhD thesis, Imperial College London.

Kozeny, J. (1927). Ueber kapillare leitung des wassers im boden. *Sitzungsberichte der Akademie der Wissenschaften in Wien*, 136:271.

Li, D., Zhao, Y., Liu, N., and Gao, X. (2023a). An Assessment Model for the Erosion Occurrence of Gap-Graded Sand-Gravel Soils under Variable Seepage Direction. *Water*, 15(8):1487.

Li, G.-y., Zhan, L.-t., Hu, Z., and Chen, Y.-m. (2021). Effects of particle gradation and geometry on the pore characteristics and water retention curves of granular soils: A combined DEM and PNM investigation. *Granular Matter*, 23(1):9.

Li, M.-W., Hu, S.-L., and Tong, C.-X. (2023b). Numerical Simulation of Mechanical Properties of Soil Considering the Effect of Internal Erosion. *Mathematics*, 11(13):2959.

Li, S., Russell, A. R., and Muir Wood, D. (2024). Internal erosion of a gap-graded soil and influences on the critical state. *Acta Geotechnica*, 19(8):5363–5381.

Li, S. and Smith, A. (2023). Acoustic emission and energy dissipation in soils during triaxial shearing. *Computers and Geotechnics*, 162:105639.

Li, S. and Smith, A. (2025). Pipeline–Soil Interaction Behavior: Acoustic Emission and Energy Dissipation. *Journal of Geotechnical and Geoenvironmental Engineering*, 151(2):04024157.

Li, W. C., Deng, G., Liang, X. Q., Sun, X. X., Wang, S. W., and Lee, M. L. (2020). Effects of stress state and fine fraction on stress transmission in internally unstable granular mixtures investigated via discrete element method. *Powder Technology*, 367:659–670.

Lian, X., Savari, C., Li, K., and Barigou, M. (2023). Coupled smoothed particle hydrodynamics and discrete element method for simulating coarse food particles in a non-Newtonian conveying fluid. *Physics of Fluids*, 35(4):043325.

Liang, L., Tian, D.-L., and Li, Z.-C. (2024). Internal erosion process and its influence factors in widely graded loose soils due to rainfall infiltration. *Frontiers in Earth Science*, 12.

Liang, Y., Yeh, T.-C. J., Chen, Q., Xu, W., Dang, X., and Hao, Y. (2019a). Particle erosion in suffusion under isotropic and anisotropic stress states. *Soils and Foundations*, 59(5):1371–1384.

Liang, Y., Yeh, T.-C. J., Ma, C., Zhang, Q., Yang, D., and Hao, Y. (2020). Experimental investigation of internal erosion behaviours in inclined seepage flow. *HYDROLOGICAL PROCESSES*, 34(26):5315–5326.

Liang, Y., Yeh, T.-C. J., Wang, J., Liu, M., Zha, Y., and Hao, Y. (2019b). Onset of suffusion in upward seepage under isotropic and anisotropic stress conditions. *European Journal of Environmental and Civil Engineering*, 23(12):1520–1534.

Liang, Y., Zeng, C., Wang, J.-J., Liu, M.-W., Jim Yeh, T.-C., and Zha, Y.-Y. (2017). Constant Gradient Erosion Apparatus for Appraisal of Piping Behavior in Upward Seepage Flow. *Geotechnical Testing Journal*, 40(4):630–642.

Liu, C. (2021a). The basic structure of MatDEM. In Liu, C., editor, *Matrix Discrete Element Analysis of Geological and Geotechnical Engineering*, pages 27–55. Springer, Singapore.

Liu, C. (2021b). *Matrix Discrete Element Analysis of Geological and Geotechnical Engineering*. Springer Singapore, Singapore.

Liu, F., Singh, J., Chen, C., Li, Y., and Wang, G. (2024a). Hydrological and Mechanical Behavior of Granular Materials Subjected to Internal Erosion: A Review. *KSCE Journal of Civil Engineering*, page 100047.

Liu, J., Chen, W., Liu, T., Yu, J., Dong, J., and Nie, W. (2018). Effects of Initial Porosity and Water Pressure on Seepage-Erosion Properties of Water Inrush in Completely Weathered Granite. *Geofluids*, 2018:1–11.

Liu, L., Chen, R., Li, Z., Zhou, C., and Li, X. (2024b). A new method for preventing sidewall preferential flow in the internal erosion simulation using un-resolved CFD–DEM. *Acta Geophysica*, 72(5):3595–3607.

Liu, L., Chen, R., Zhou, C., Li, X., and Bate, B. (2023a). Microscopic mechanism of the combined effects of confining pressure and fines content on suffusion in gap-graded underfilled soils. *Journal of Hydrology*, 626(B):130370.

Liu, Y., Wang, L., Hong, Y., Zhao, J., and Yin, Z.-Y. (2020). A coupled CFD-DEM investigation of suffusion of gap graded soil: Coupling effect of confining pressure and fines

content. *International Journal for Numerical and Analytical Methods in Geomechanics*, 44(18):2473–2500.

Liu, Y., Wang, L., Yin, Z.-Y., and Hong, Y. (2023b). A coupled CFD-DEM investigation into suffusion of gap-graded soil considering anisotropic stress conditions and flow directions. *Acta Geotechnica*, 18(6):3111–3132.

Liu, Y., Yin, Z.-Y., Wang, L., and Hong, Y. (2021). A coupled CFD–DEM investigation of internal erosion considering suspension flow. *Canadian Geotechnical Journal*, 58(9):1411–1425.

Liu, Y.-J., Yin, Z.-Y., Huang, S., Lai, Z., and Zhou, C. (2024c). Resolved CFD-DEM Modeling of Suffusion in Gap-Graded Shaped Granular Soils. *Journal of Geotechnical and Geoenvironmental Engineering*, 150(4):04024008.

Luo, Y., Luo, B., and Xiao, M. (2020). Effect of deviator stress on the initiation of suffusion. *Acta Geotechnica*, 15(6):1607–1617.

Luo, Y. L. and Kong, X. F. (2016). Effect of the load history of hydraulic gradient on suffusion. In *Hydraulic Engineering IV*, pages 11–16. CRC Press.

Luo, Y.-l., Wu, Q., Zhan, M.-l., Sheng, J.-c., and Wang, Y. (2013). Hydro-mechanical coupling experiments on suffusion in sandy gravel foundations containing a partially penetrating cut-off wall. *Natural Hazards*, 67(2):659–674.

Ma, G., Bui, H. H., Lian, Y., Tran, K. M., and Nguyen, G. D. (2022). A five-phase approach, SPH framework and applications for predictions of seepage-induced internal erosion and failure in unsaturated/saturated porous media. *Computer Methods in Applied Mechanics and Engineering*, 401:115614.

Mao, X., Cai, P., Fu, J., and Dai, Z. (2023). Study on internal erosion and structural evolution mechanism of soil–rock mixture. *Natural Hazards*, 118(2):1739–1764.

Mao, Y., Kong, Y., and Guan, M. (2022). GPU-accelerated SPH modeling of flow-driven sediment erosion with different rheological models and yield criteria. *Powder Technology*, 412:118015.

Maroof, M. A., Mahboubi, A., and Noorzad, A. (2021). Effects of grain morphology on suffusion susceptibility of cohesionless soils. *Granular Matter*, 23(1):8.

Marot, D., Dinh, M. T., Bendahmane, F., and Van, T. L. (2020). Multidirectional Flow Apparatus for Assessing Soil Internal Erosion Susceptibility. *GEOTECHNICAL TESTING JOURNAL*, 43(6):1481–1498.

Marot, D., Rochim, A., Nguyen, H.-H., Bendahmane, F., and Sibille, L. (2016). Assessing the susceptibility of gap-graded soils to internal erosion: Proposition of a new experimental methodology. *Natural Hazards*, 83(1):365–388.

Minh, N. H., Cheng, Y. P., and Thornton, C. (2014). Strong force networks in granular mixtures. *Granular Matter*, 16(1):69–78.

Morimoto, T., O'Sullivan, C., and Taborda, D. M. G. (2024). Applying Network Modeling to Determine Seepage-Induced Forces on Soil Particles. *Journal of Geotechnical and Geoenvironmental Engineering*, 150(5):04024029.

Mu, L., Zhang, P., Shi, Z., and Huang, M. (2023). Coupled CFD–DEM Investigation of Erosion Accompanied by Clogging Mechanism under Different Hydraulic Gradients. *Computers and Geotechnics*, 153:105058.

Muhammad, N. (2021). Finite volume method for simulation of flowing fluid via OpenFOAM. *The European Physical Journal Plus*, 136(10):1–22.

Nguyen, C. D., Benahmed, N., Andò, E., Sibille, L., and Philippe, P. (2019). Experimental investigation of microstructural changes in soils eroded by suffusion using X-ray tomography. *Acta Geotechnica*, 14(3):749–765.

Nguyen, T. T. and Indraratna, B. (2020). A Coupled CFD–DEM Approach to Examine the Hydraulic Critical State of Soil under Increasing Hydraulic Gradient. *International Journal of Geomechanics*, 20(9):04020138.

Oueidat, M., Benamar, A., and Bennabi, A. (2021). Effect of Fine Particles and Soil Heterogeneity on the Initiation of Suffusion. *Geotechnical and Geological Engineering*, 39(3):2359–2371.

Ouyang, M. and Takahashi, A. (2016). Influence of initial fines content on fabric of soils subjected to internal erosion. *Canadian Geotechnical Journal*, 53(2):299–313.

Pachideh, V. and Mir Mohammad Hosseini, S. M. (2019). A New Physical Model for Studying Flow Direction and Other Influencing Parameters on the Internal Erosion of Soils. *Geotechnical Testing Journal*, 42(6):1431–1456.

Panchuk, K. (2019). 8.4 Weathering and Erosion Produce Sediments. *Physical Geology, First University of Saskatchewan Edition*.

Persson, P.-O. and Strang, G. (2004). A simple mesh generator in MATLAB. *SIAM review*, 46(2):329–345.

Prasomsri, J., Shire, T., and Takahashi, A. (2021). Effect of fines content on onset of internal instability and suffusion of sand mixtures. *Géotechnique Letters*, 11(3):209–214.

Prasomsri, J. and Takahashi, A. (2020). The role of fines on internal instability and its impact on undrained mechanical response of gap-graded soils. *Soils and Foundations*, 60(6):1468–1488.

Qian, J.-G., Zhou, C., Yin, Z.-Y., and Li, W.-Y. (2021). Investigating the effect of particle angularity on suffusion of gap-graded soil using coupled CFD-DEM. *Computers and Geotechnics*, 139:104383.

Radjai, F., Roux, S., and Moreau, J. J. (1999). Contact forces in a granular packing. *Chaos: An Interdisciplinary Journal of Nonlinear Science*, 9(3):544–550.

Rahman, F. U. (2018). Different Types of Soil – Sand, Silt, Clay and Loam. https://theconstructor.org/practical-guide/material-testing/soil/soil-types-sand-silt-clay-loam/25208/.

Rao, D. and Bai, B. (2020). Study of the Factors Influencing Diffusive Tortuosity Based on Pore-Scale SPH Simulation of Granular Soil. *Transport in Porous Media*, 132(2):333–353.

Ren, J., Yao, Y.-j., Dong, H., and Jing, Y. (2024). Calculation model of depth under quantification of surface morphology of dry shrinkage cracks in red clay. *IOP Conference Series: Earth and Environmental Science*, 1334(1):012023.

Richards, K. S. and Reddy, K. R. (2007). Critical appraisal of piping phenomena in earth dams. *Bulletin of Engineering Geology and the Environment*, 66(4):381–402.

Rochim, A., Marot, D., Sibille, L., and Thao Le, V. (2017). Effects of Hydraulic Loading History on Suffusion Susceptibility of Cohesionless Soils. *Journal of Geotechnical and Geoenvironmental Engineering*, 143(7):04017025.

Scheuermann, A., Harshani, H. M. D., and Galindo-Torres, S. A. (2019). Micro-scale Flow Conditions Leading to the Onset of Erosion. In Bonelli, S., Jommi, C., and Sterpi, D., editors, *Internal Erosion in Earthdams, Dikes and Levees*, pages 180–188, Cham. Springer International Publishing.

Sharp, M., Wallis, M., Deniaud, F., Hersch-Burdick, R., Tourment, R., Matheu, E., Seda-Sanabria, Y., Wersching, S., Veylon, G., Durand, E., Smith, P., Forbis, J., Spliethoff, C., van Hemert, H., Igigabel, M., Pohl, R., Royet, P., Sharp, M., Simm, J., Tourment, R., and Wallis, M. (2013). *The International Levee Handbook*. CIRIA.

Shire, T., O'Sullivan, C., and Hanley, K. J. (2016). The influence of fines content and size-ratio on the micro-scale properties of dense bimodal materials. *Granular Matter*, 18(3):52.

Sibille, L., Marot, D., Poullain, P., and Lominé, F. (2016). Phenomenological interpretation of internal erosion in granular soils from a discrete fluid-solid numerical model.

Stearns, F. P., Hasen, A., North, E. P., Ehle, B., Paschke, T., Burr, W. H., Menocal, A. G., Pharr, H. N., Duryea, E., Sundstrom, C. A., Wegmann, E., Forchheimer, P., Campbell, J. L., and Ford, J. T. (1902). Discussion on The Bohio Dam. *Transactions of the American Society of Civil Engineers*, 48(2):259–308.

Su, Z., Wang, S., Li, D., Sheng, J., and Wu, W. (2024). SPH–DEM modeling overtopping failure of earthfill dams. *Acta Geotechnica*, 19(2):953–970.

Sufian, A., Knight, C., O'Sullivan, C., van Wachem, B., and Dini, D. (2019a). Ability of a pore network model to predict fluid flow and drag in saturated granular materials. *Computers and Geotechnics*, 110:344–366.

Sufian, A., Knight, C., O'Sullivan, C., van Wachem, B., and Dini, D. (2019b). EWG-28 Application of Pore Network Models to Investigate Internal Erosion in Gap-Graded Soils. In *Book of Abstracts*, page 92.

Sullivan, RR. and Hertel, KL. (1942). The permeability method for determining specific surface of fibers and powders. *Advances in colloid science*, 1:37–80.

Taha, H., Nguyen, N.-S., Marot, D., Hijazi, A., and Abou-Saleh, K. (2019). Micro-scale investigation of the role of finer grains in the behavior of bidisperse granular materials. *Granular Matter*, 21(2):28.

Terzaghi, K. (1939). 45TH JAMES FORREST LECTURE, 1939. SOIL MECHANICS - A NEW CHAPTER IN ENGINEERING SCIENCE. *Journal of the Institution of Civil Engineers*, 12(7):106–142.

Thornton, C. and Antony, SJ. (1998). Quasi–static deformation of particulate media. *Philosophical Transactions of the Royal Society of London. Series A: Mathematical, Physical and Engineering Sciences*, 356(1747):2763–2782.

Tian, D., Xie, Q., Fu, X., and Zhang, J. (2020). Experimental study on the effect of fine contents on internal erosion in natural soil deposits. *Bulletin of Engineering Geology and the Environment*, 79(8):4135–4150.

Tran, D.-K., Prime, N., Froiio, F., Callari, C., and Vincens, E. (2017). Discrete modelling of front propagation in backward piping erosion. *EPJ Web of Conferences*, 140:09036.

Wan, C. F. and Fell, R. (2008). Assessing the potential of internal instability and suffusion in embankment dams and their foundations. *Journal of geotechnical and geoenvironmental engineering*, 134(3):401–407.

Wang, Tang, Y., Huang, B., Hu, T., and Ling, D. (2021). Review on numerical simulation of the internal soil erosion mechanisms using the discrete element method. *Water*, 13(2):169.

Wang, M., Feng, Y., and Wang, C. (2016). Coupled bonded particle and lattice Boltzmann method for modelling fluid–solid interaction. *International Journal for Numerical and Analytical Methods in Geomechanics*, 40(10):1383–1401.

Wang, M., Feng, Y. T., Pande, G. N., Chan, A. H. C., and Zuo, W. X. (2017). Numerical modelling of fluid-induced soil erosion in granular filters using a coupled bonded particle lattice Boltzmann method. *Computers and Geotechnics*, 82:134–143.

Wang, P. and Arson, C. (2018). Energy distribution during the quasi-static confined comminution of granular materials. *Acta Geotechnica*, 13(5):1075–1083.

Wang, P., Ge, Y., Wang, T., Liu, Q.-w., and Song, S.-x. (2023a). CFD-DEM modelling of suffusion in multi-layer soils with different fines contents and impermeable zones. *Journal of Zhejiang University-SCIENCE A*, 24(1):6–19.

Wang, T., Wang, P., Yin, Z.-y., and Zhang, F. (2022a). DEM-DFM modeling of suffusion in calcareous sands considering the effect of double-porosity. *Computers and Geotechnics*, 151:104965.

Wang, T., Zhang, F., and Zheng, W. (2023b). Suffusion of gap-graded soil with realistically shaped coarse grains: A DEM–DFM numerical study. *International Journal of Geomechanics*, 23(1):04022247.

Wang, X., Huang, B., Tang, Y., Hu, T., and Ling, D. (2022b). Microscopic mechanism and analytical modeling of seepage-induced erosion in bimodal soils. *Computers and Geotechnics*, 141:104527.

Wang, Y., Chai, J., Xu, Z., Qin, Y., and Wang, X. (2020). Numerical Simulation of the Fluid–Solid Coupling Mechanism of Internal Erosion in Granular Soil. *Water*, 12(1):137.

Wu, B., Yan, Q., Wang, L., Chen, Q., Wang, T., and Zhang, F. (2020). DEM simulation of internal erosion around a submerged defective pipe. *IOP Conference Series: Earth and Environmental Science*, 570(2):022050.

Wu, Y., Hou, Q., Qi, Z., and Yu, A. (2021). Particle–pore scale modelling of particle–fluid flows. *Chemical Engineering Science*, 235:116500.

Xia, W., Liu, C., Liu, H., Zhao, T., and Zhu, Y. (2024). Modeling of particle migration in piping based on an improved discrete element method. *Rock Mechanics Bulletin*, 4(1):100151.

Xiao, Q. and Wang, J.-P. (2020). CFD–DEM simulations of seepage-induced erosion. *Water*, 12(3):678.

Xie, Q., Liu, J., Han, B., Li, H., Li, Y., and Li, X. (2018). Critical hydraulic gradient of internal erosion at the soil–structure interface. *Processes*, 6(7):92.

Xing, B., Fan, W., Lyu, Y., Sun, H., and Che, J. (2021). Influence of particle mineralogy and size on the morphological characteristics of mineral fillers. *Journal of Materials Research and Technology*, 15:3995–4009.

Xiong, H., Wu, H., Bao, X., and Fei, J. (2021a). Investigating effect of particle shape on suffusion by CFD-DEM modeling. *Construction and Building Materials*, 289:123043.

Xiong, H., Yin, Z.-Y., Zhao, J., and Yang, Y. (2021b). Investigating the effect of flow direction on suffusion and its impacts on gap-graded granular soils. *Acta Geotechnica*, 16(2):399–419.

Xiong, H., Zhang, Z., Bao, X., Wu, H., Yin, Z.-y., and Chen, X. (2024). Micro-mechanical analysis of particle shape effect on suffusion of gap-graded soils. *Computers and Geotechnics*, 165:105925.

Xiong, H., Zhang, Z., Sun, X., Yin, Z.-y., and Chen, X. (2022). Clogging effect of fines in seepage erosion by using CFD–DEM. *Computers and Geotechnics*, 152:105013.

Xiong, H., Zhang, Z., Yang, J., Yin, Z.-y., and Chen, X. (2023). Role of inherent anisotropy in infiltration mechanism of suffusion with irregular granular skeletons. *Computers and Geotechnics*, 162:105692.

Xu, ZD., Zhang, L. M., Kamali Zarch, M., and Wang, HJ. (2022). Experimental study of internal erosion in granular soil subject to cyclic hydraulic gradient reversal. *Journal of Geotechnical and Geoenvironmental Engineering*, 148(5):04022014.

Yang, J. and Luo, X. D. (2015). Exploring the relationship between critical state and particle shape for granular materials. *Journal of the Mechanics and Physics of Solids*, 84:196–213.

Yang, J., Yin, Z.-Y., Laouafa, F., and Hicher, P.-Y. (2019a). Analysis of suffusion in cohesionless soils with randomly distributed porosity and fines content. *Computers and Geotechnics*, 111:157–171.

Yang, J., Yin, Z.-Y., Laouafa, F., and Hicher, P.-Y. (2019b). Internal erosion in dike-on-foundation modeled by a coupled hydromechanical approach. *International Journal for Numerical and Analytical Methods in Geomechanics*, 43(3):663–683.

Yang, K.-H. and Wang, J.-Y. (2017). Experiment and statistical assessment on piping failures in soils with different gradations. *MARINE GEORESOURCES & GEOTECHNOLOGY*, 35(4):512–527.

Yin, Y., Cui, Y., Tang, Y., Liu, D., Lei, M., and Chan, D. (2021). Solid–fluid sequentially coupled simulation of internal erosion of soils due to seepage. *Granular Matter*, 23(2):20.

Yin, Z.-Y., Yang, J., Laouafa, F., and Hicher, P.-Y. (2023). A framework for coupled hydro-mechanical continuous modelling of gap-graded granular soils subjected to suffusion. *European Journal of Environmental and Civil Engineering*, 27(8):2678–2699.

Zhang, F., Wang, T., Liu, F., Peng, M., Furtney, J., and Zhang, L. (2020). Modeling of fluid-particle interaction by coupling the discrete element method with a dynamic fluid mesh: Implications to suffusion in gap-graded soils. *Computers and Geotechnics*, 124:103617.

Zhang, L., Deng, G., Chen, R., and Luo, Z. (2023a). Confining stress effects on global and local responses of internal erosion in gap-graded cohesionless soils. *Bulletin of Engineering Geology and the Environment*, 82(8):326.

Zhang, L., Wu, F., Zhang, H., Zhang, L., and Zhang, J. (2019). Influences of internal erosion on infiltration and slope stability. *Bulletin of Engineering Geology and the Environment*, 78(3):1815–1827.

Zhang, Y., Li, J., Xu, Y., Zhu, H., and Liu, Z. (2023b). Numerical simulation of dike failure using a GPU-based coupled DEM–SPH model. *Computers & Fluids*, 267:106090.

Zhao, Y., Hu, Z., Zheng, Y., and Wu, Q. (2024). Influences of particle size ratio and fines content on the suffusion characteristics of gap-graded soils. *GRANULAR MATTER*, 26(2):52.

Zhao, Y., Wu, Q., Hu, Z., Jia, Y., and Zheng, Y. (2025). Macro- and micro-scopic suffusion behavior of gap-graded soils under cyclic hydraulic gradient reversal. *Computers and Geotechnics*, 178:106950.

Zheng, G., Tong, J., Zhang, T., and Ng, C. W. W. (2022). Progression of backward erosion piping with sudden and gradual hydraulic loads. *Acta Geotechnica*, 17(5):2029–2035.

Zhou, C. and Ooi, J. Y. (2009). Numerical investigation of progressive development of granular pile with spherical and non-spherical particles. *Mechanics of Materials*, 41(6):707–714.

Zhou, C., Qian, J.-G., and Yin, Z.-Y. (2022). Microscopic investigation of the influence of complex stress states on internal erosion and its impacts on critical hydraulic gradients. *International Journal for Numerical and Analytical Methods in Geomechanics*, 46(18):3377–3401.

Zhou, C., Qian, J.-G., Yin, Z.-Y., Liu, Y.-J., and Du, Z.-B. (2023a). Effect of particle shape and bedding angle on suffusion in gap-graded granular soils by coupled CFD-DEM method. *International Journal for Numerical and Analytical Methods in Geomechanics*, 47(8):1373–1398.

Zhou, C., Qian, J.-G., Yin, Z.-Y., and Xiong, H. (2023b). Suffusion in gap-graded granular soils subjected to strain-controlled cyclic loading with coupled CFD-DEM method. *Transportation Geotechnics*, 42:101098.

Zhou, W., Ma, Q., Ma, G., Cao, X., and Cheng, Y. (2020a). Microscopic investigation of internal erosion in binary mixtures via the coupled LBM-DEM method. *Powder Technology*, 376:31–41.

Zhou, Y., Chen, L., Gong, Y., and Wang, S. (2021). Pore-Scale Simulations of Particles Migration and Deposition in Porous Media Using LBM-DEM Coupling Method. *Processes*, 9(3):465.

Zhou, Y. C., Wright, B. D., Yang, R. Y., Xu, B. H., and Yu, A. B. (1999). Rolling friction in the dynamic simulation of sandpile formation. *Physica A: Statistical Mechanics and its Applications*, 269(2):536–553.

Zhou, Z., Li, Z., Ranjith, P. G., Wen, Z., Shi, S., and Wei, C. (2020b). Numerical simulation of the influence of seepage direction on suffusion in granular soils. *Arabian Journal of Geosciences*, 13(14):669.

Zhou, Z. Y., Kuang, S. B., Chu, K. W., and Yu, A. B. (2010). Discrete particle simulation of particle–fluid flow: Model formulations and their applicability. *Journal of Fluid Mechanics*, 661:482–510.

Zhou, Z. Y., Yu, A. B., and Choi, S. K. (2011). Numerical simulation of the liquid-induced erosion in a weakly bonded sand assembly. *Powder Technology*, 211(2-3):237–249.

Zhu, Y., Liu, C., Liu, H., Kou, Y.-d., and Shi, B. (2023). A multi-field and fluid–solid coupling method for porous media based on DEM-PNM. *Computers and Geotechnics*, 154:105118.

Zhu, Y., Nie, Z., Gong, J., Zou, J., Zhao, L., and Li, L. (2020). An analysis of the effects of the size ratio and fines content on the shear behaviors of binary mixtures using DEM. *Computers and Geotechnics*, 118:103353.

Zou, Y., Chen, C., and Zhang, L. (2020). Simulating Progression of Internal Erosion in Gap-Graded Sandy Gravels Using Coupled CFD-DEM. *International Journal of Geomechanics*, 20(1):04019135.

Zou, Y., Ma, G., Zhao, S., Chen, S., and Zhou, W. (2023). Particle shape transforms the driving of shear stress in granular materials. *Powder Technology*, 416:118235.